ISSN 2954-436X

Geofísica Internacional

Revista Trimestral Publicada por el Instituto de Geofísica de la Universidad Nacional Autónoma de México

México
Volume 62 Number 1
January - March

— Geofísica Internacional —

GEOFÍSICA INTERNACIONAL, Año 62, Vol. 62, Núm. 1, enero - marzo de 2023 es una publicación trimestral, editada por la Universidad Nacional Autónoma de México, Ciudad Universitaria, Alcaldía Coyoacán, C.P. 04150, Ciudad de México, a través del Instituto de Geofísica, Circuito de la Investigación Científica s/n, Ciudad Universitaria, Alcaldía Coyoacán, C.P. 04150, Ciudad de México, Tel. (55)56 22 41 15. URL: http://revistagi.geofisica.unam.mx, correo electrónico: revistagi@igeofisica.unam.mx. Editora responsable: Andrea Rostan Robledo. Certificado de Reserva de Derechos al uso Exclusivo del Título: 04-2022-081610251200-102, ISSN: 2954-436X, otorgados por el Instituto Nacional del Derecho de Autor (INDAUTOR). Responsable de la última actualización Saúl Armendáriz Sánchez, Editor Técnico. Fecha de la última modificación: 31 de diciembre 2022, Circuito de la Investigación Científica s/n, Ciudad Universitaria, Alcaldía Coyoacán, C.P. 04150, Ciudad de México.

https://www.doi.org/10.22201/igeof.2954436xe.2023.62.1

Geofísica Internacional

Vol. 62, Núm. 1, enero - marzo de 2023

Contents

Geofísica Internacional (2023) **62-1**: 377 - 385

Ground Penetrating Radar (GPR) Investigation of Queen Sheba (Bilikisu Sungbo) Possible Burial Site in Oke-Eri, Ijebu-Ode, Southwestern Nigeria

Olawale Olakunle Osinowo[1], Quam Ademola Elebute[2]

Abstract

The near subsurface imaging strength of Ground Penetrating Radar (GPR) which can delineate regions of contrasting dielectric properties has been explored in this study to identify the contentious burial tomb of the biblical Queen Sheba (Bilikisu Sungbo) located in the Oke-eri area of Ijebu province in southwestern, Nigeria. The site is highly revered as sacred by Christians, Muslims and Traditional worshippers and claimed by the Ijebus as heroin who came back from King Solomon's voyage to build a fortified city. The filtered and processed GPR data acquired using a 400 MHz antenna GSSI SIR-3000 for GPR system via twenty-three (23) established profiles, surveyed at 2 m inter-profile separation, presented varying amplitude GPR reflection which characterize the entire study area at different depths as observed from the various iso-depth slices extracted from the combined GPR radargrams. Unique and consistent high amplitude GPR reflection patterns and classic hyperbolic diffraction curves dominate part of the burial site cordoned off and claimed by the local as the grave of the queen. The reflection pattern beneath the grave is observed to be consistent in amplitude, size, shape and exist right from 0.91 m to 1.83 m depth beneath the surface. The unique reflection signatures beneath the burial site suggest occurrence of materials which differ considerably in dielectric properties from that of the surrounding geologic rocks which could be tomb walls, void or simply non-geologic / anthropogenic materials consistent with burial activities.

Keywords: Dielectric properties, Anthropogenic activities, GPR reflection pattern, Queen Sheba, King Solomon.

Resumen

En este estudio se exploró la intensidad de las imágenes cercanas al subsuelo con el radar de penetración terrestre (GPR, por sus siglas en inglés), el cual puede delinear regiones de propiedades dieléctricas contrastantes con el propósito de identificar la polémica tumba funeraria de la bíblica reina Sheba (Bilikisu Sungbo), la cual se encuentra ubicada en el área de Oke-eri de Ijebu, provincia en el suroeste de Nigeria. El sitio es muy venerado por cristianos, musulmanes y adoradores tradicionales, y los Ijebus lo reclaman como una heroína que regresó del viaje del rey Salomón para construir una ciudad fortificada. Los datos GPR filtrados se procesaron adquiridos utilizando una antena GSSI SIR-3000 de 400 MHz a través de 23 perfiles establecidos, medidos con una separación entre unos de 2 m. Los resultados nos muestran una reflexión GPR de amplitud variable, la cual caracteriza toda el área de estudio en diferentes profundidades. Éstas, se observan a partir de los diversos cortes de isoprofundidad extraídos de los radargramas GPR combinados. Dominan parte del sitio de entierro patrones de reflexión GPR únicos y consistentes de alta amplitud y curvas de difracción hiperbólica clásicas. Se observa que el patrón de reflexión debajo de la tumba es consistente en amplitud, tamaño, forma y existe desde 0,91 a 1,83 m de profundidad. Las firmas de reflexión únicas debajo del sitio del entierro sugieren la presencia de materiales que difieren considerablemente en propiedades dieléctricas de las rocas geológicas circundantes que podrían ser paredes de tumbas, vacíos o simplemente materiales no geológicos / antropogénicos consistentes con las actividades del entierro.

Palabras clave: Propiedades dieléctricas, Actividades antropogénicas, Patrón de reflexión GPR, Reina Saba, Rey Salomón.

Received: October 15, 2021; October 25, 2022; published on-line: January 1, 2023.

Editorial responsibility: Dulce María Vargas Bracamontes

* Corresponding author: Olawale O. Osinowo
[1] Department of Geology, University of Ibadan, Ibadan, Nigeria, 200284. E-mail: olawale.osinowo13@alumni.imperial.ac.uk
[2] Department of Geology, University of Ibadan, Ibadan, Nigeria, 200284. E-mail: wale.osinowo@ui.edu.ng

https://doi.org/10.22201/igeof.2954436xe.2023.62.1.1446

Introduction

Several versions of the historical background and the place of birth of the biblical Queen Sheba documented in the Old Testament (1King 10: 1 - 13) as a black queen of the south with great wealth and influence who journeyed from the uttermost part of the earth to hear about the wisdom of King Solomon exist and are well documented. Some records account that she was originally from today's known country of Yemen (Seligsoha *et al.*, 1906) while the Ethiopians held Makeda (Queen of Sheba) in high esteem as the mother of Melenik 1, a son she had with King Solomon, the progenitor of the Emperor Haile Selassie dynasty that ruled Ethopia until 1974 (Belcher, 2010). The Ijebus, a stock of the Yoruba ethnic tribe in southwestern part of Nigeria has also laid claim that a powerful Yoruba queen (Bilikisu Sungbo, (Bilqis) the Islamic version), reported to have great power and wealth, is the biblical Queen Sheba (Darling, 1997, 1999, 2001). Tradition claims that she returned from her voyage to visit King Solomon and settled in the Yoruba kingdom afterwards building a great fortified city with a trench (up to 20 m deep in some places), constructed by her servants in a mysterious way, along the perimeter of the Ijebu Kingdom (Darling, 1997). The trench popularly known as 'Eredo' (ditch in Ijebu dialect) and currently on Nigeria's tentative list of potential UNESCO World heritage sites, has been compared to other UNESCO Heritage Sites such as The Pyramid of Giza and The Great Wall of China (Darling, 1997, 2001). The trenches, which were usually mounted by guards at certain points, to protect against invasion, surround the kingdom and extend over 160 km in length. Remains of the trench still exist today (Figure 1). The burial site of this controversial woman of great influence has been greatly revered by some Christian, Islamic and Traditional religion worshipers, some for tourism, while others pay visit to draw some sort of spiritual powers including answers to prayers. Several myths surround the burial site, many of which have been documented by other researchers (e.g. Aremu, 2002; Ogundele and Babalola, 2007; Aremu *et al.*, 2013).

Several archaeological and anthropological studies have been carried to establish or refute some of the mythical claims (Ogundele and Babalola, 2007; Aremu *et al.*, 2013). However, geophysical investigation techniques though limited in confirming if the so much revered Bilikisu Sungbo is indeed the biblical Queen Sheba's tomb, but it is apt, through its subsurface imaging ability, to establish the occurrence of a tomb. Ground penetrating radar is a non-invasive geophysical technique that employs reflections of electromagnetic energy generated by a transmitter, to image the subsurface on the account of variation in subsurface dielectric properties. The technique has recently gained relevance in archaeological investigation, particularly to locate buried archaeological features, artifacts, and important cultural strata (Perez-Gracia *et al.*, 2009; Masini *et al.*, 2010; Conyers, 2006; Conyers, 2012). This study therefore employs the subsurface imaging ability of ground penetrating radar geophysical techniques to evaluate the burial site and thus establish if a grave exists within the assumed region where the burial site of this woman is situated.

Geology of the study area

The study area lies within the transition zone between the crystalline basement rocks and sedimentary rocks situated

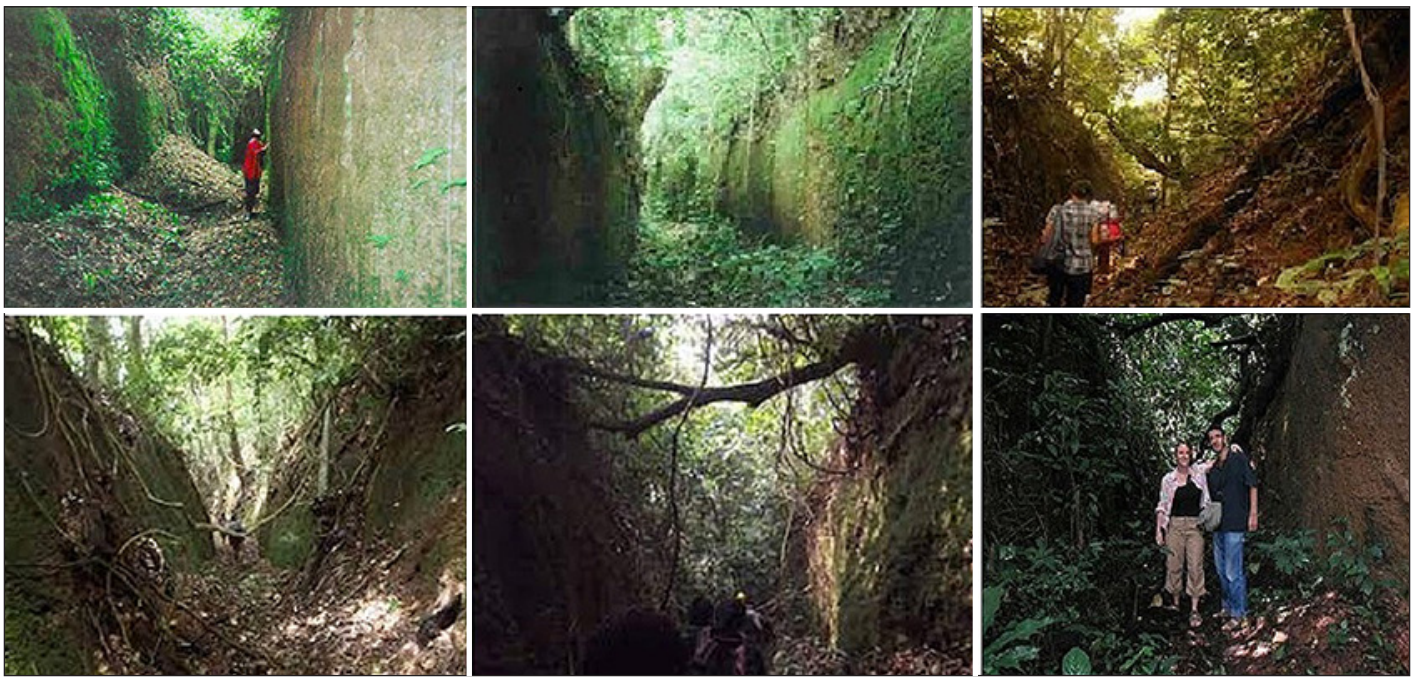

Figure 1. Pictures of the Bilikisu Sungbo trench excavated at different parts of Ijebu land (Darling, 1997, 2001; Wikipedia, 2021).

between latitude 7ºN and 10ºN and longitudes 3ºE and 6ºE outskirt of Ijebu-Ode town. The geology of Ijebu-Ode and environs has been described by Osinowo and Olayinka (2012, 2013) to belong to the transition geological environment between the Precambrian Basement Complex rocks of southwestern Nigeria and the Cretaceous sedimentary units of the Abeokuta Formation in the eastern part of the Dahomey Basin (Figure 2). The northern (northeast, northwest and north central) is underlain by basement rocks of Migmatite Gneiss Complex which comprises of biotite granite gneiss, biotite-hornblende gneiss that intrude schistose host rocks such as biotite schist, quartzite schist, talc-tremolite schist, and Muscovite schists (Oyawoye 1972; Rahaman 1988; Osinowo and Olayinka, 2012, 2013). The southern portion is overlain by Ise Member of the Abeokuta Group that unconformably overlies the basement rocks. The sedimentary unit comprise mainly of grits, arkosic sandstones, siltstones and clay with occasional conglomerate of predominantly arenaceous materials (Omatsola and Adegoke, 1981).

Local Geology

The studied burial site is situated in Oke-eri, a village settlement located in the northern part of Ijebu-Ode. It is underlain by Migmatite Gneiss Complex rocks with faults which generally trend NW-SE (Osinowo *et al.*, 2011). Prominent rocks include migmatite gneiss, biotite granite gneiss and quartz schist. The gneiss which is the oldest rock is intruded by other rock types. It is fine to medium grained, weakly foliated and variably migmatized. It strikes generally NW-SE with measured dip values that range from 37 – 49ºW. Outcrops observed around Oke-eri displayed medium to high degree of migmatization with quartz-feldspartic pegmatite veins having sodic feldspars and quartz as the prominent leucocratic mineral intrusions. The soil profile around Oke-eri, presented in the form of a geological section (Figure 3) generated from interpreted Vertical Electrical Sounding (VES) data (Obtained by Osinowo and Olayinka (2012), indicate a well-developed soil profile. The lateritic top soil unit which is about 1.6 m thick comprise of lateritic sands or sandy unit which may be capped with clayey top. This unit directly overlie the weathered/partially weathered basement rock unit (about 6.7 m) and itself underly by fresh basement rock unit of southwestern Nigeria around the study area. Osinowo and Olayinka (2012) reported the capping lateritic unit to be indurated and often inhibit adequate groundwater recharge around Ijebu-Ode, and has been identified to be responsible for poorly developed groundwater system around Ijebu-Ode and environs.

Materials and Methods

Data acquisition for imaging the upper subsurface around the Queen Sheba's (Bilikisu Sungbo) burial site was carried out using GSSI (SIR-3000) GPR equipment. The equipment which consists of a transmitter and a receiver unit was used

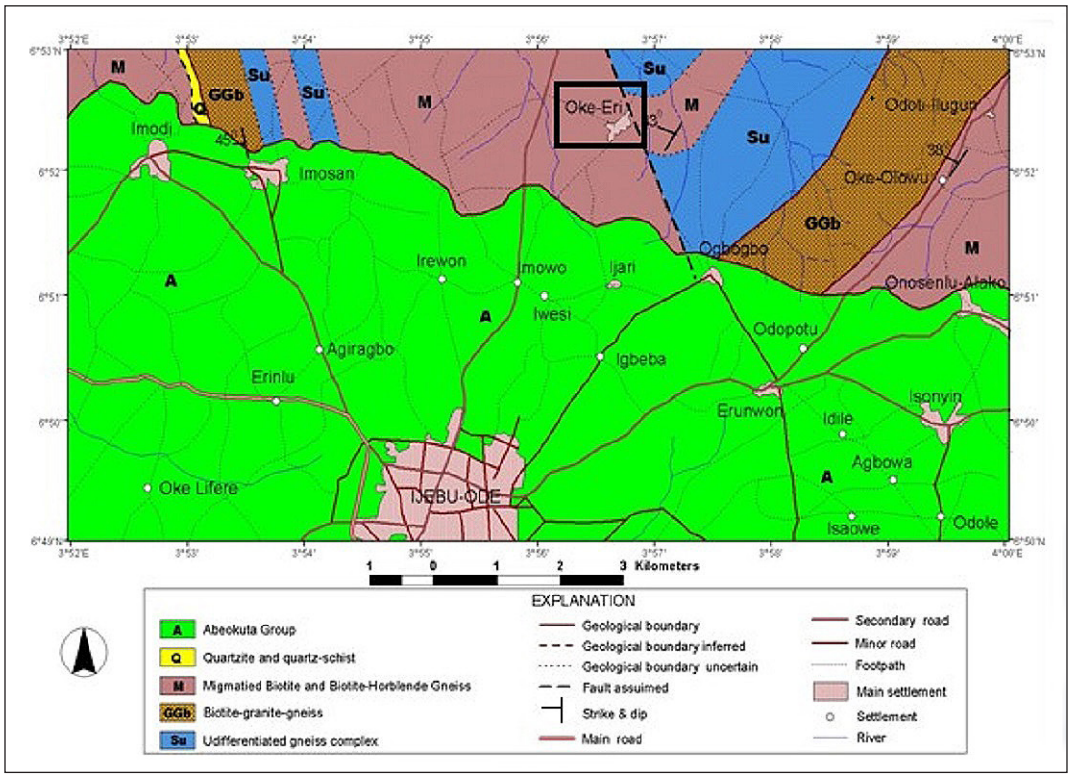

Figure 2. Geological map of Ijebu-Ode and its environs (Modified from Osinowo and Olayinka, 2012).

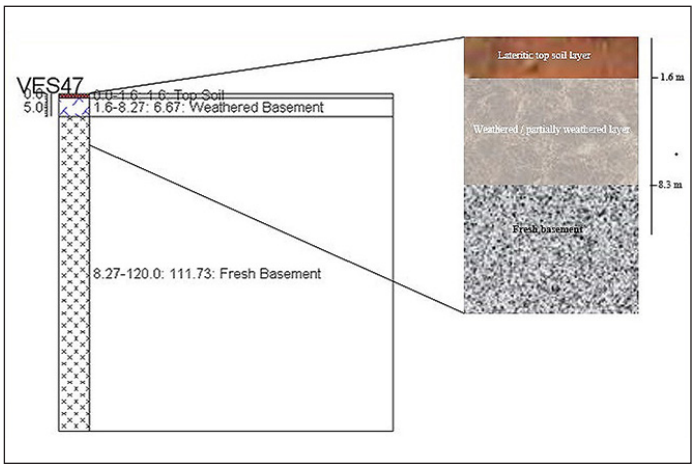

Figure 3. Geological section generated from outcrop assisted interpreted Vertical Electrical Sounding (VES) investigation carried out around the study area (Osinowo and Olayinka, 2012).

Figure 4. Photographs of the (a) GSSI (SIR-3000) GPR equipment with a 400 MHz antenna, (b) the entire burial site and the (c) Tomb area cordoned by the fence.

to measure the two-way reflection time of electromagnetic pulses reflected at interfaces of differing dielectric properties and recorded as radagrams (Leckebusch, 2003; Conyers, 2004, 2009; Annan, 2003). A 400 MHz antenna capable of probing up to 4 m was used in this study (Figure 4a). Relatively deep profiling was achieved with 400 MHz antenna by using longer range (100 ns) for the energy to penetrate deeper, with dielectric value of 9, for slightly damp sand / dry silt. The sample rate per scan of 1024, pulse rate of 2.5 ns, bits per sample of 16 and 64 scan per second were specified to achieve a relatively deeper measurement of the target subsurface depth (GSSI, 2011; 2017). Ground measurements were taken using both the geology-can and structure-scan modes for the GPR system. These measurement modes can image the geological and structural subsurface features on the account of variation in dielectric properties of the scanned geological and structural features. Twenty-three profiles

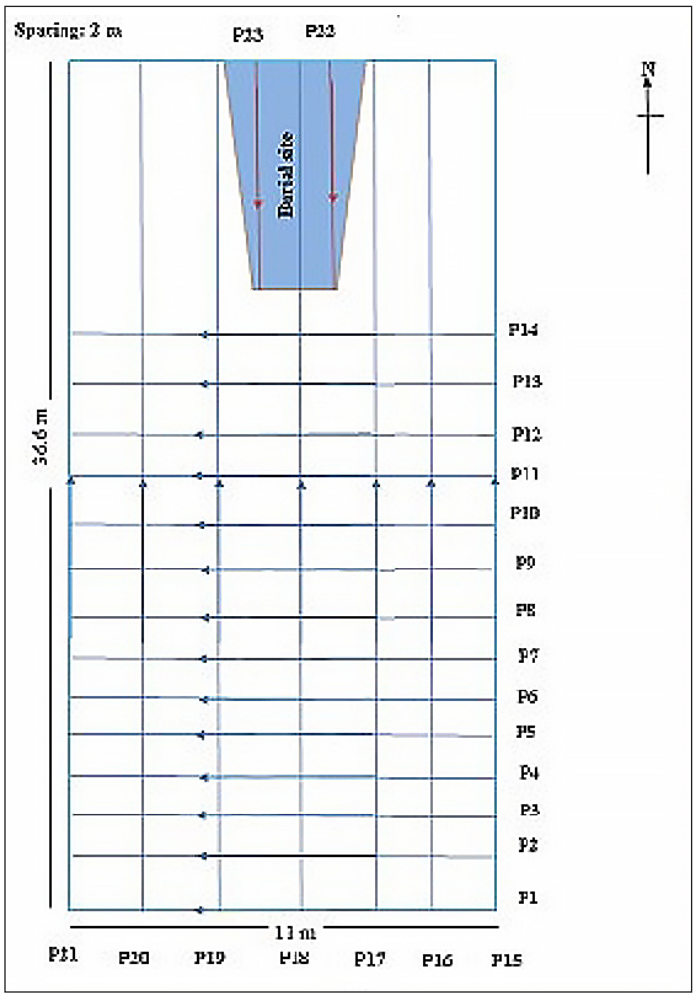

Figure 5. Schematic diagram showing the transect lines on the surveyed site.

were established at 2 m separation along E - W and S –N directions, across the entire burial site (Figure 4b). 14 profiles (P1 – P14) were set along east – west direction, seven (7) profiles (P15 – P21) were oriented to the South - North direction while two (2) short survey profiles (P22 – P23) were executed along North – South direction. The last two profiles were established within a rectangular frame constructed to restrict people's access (Figure 4a) to a region believed to directly overly the grave (Figure 5). The E – W trending profiles are approximately 11 m in length while the N - S profiles are 36.6 m long, except for profile 18 which is about 33.5 m long. The profile (P18) is shorter than the other S – N profiles because it is limited by the fence constructed to cordon off the burial site. Profiles 22 and 23 which were occupied within the cordoned off section are the shortest in length (8.5 m long). Two-way travel time of individual reflections generated at different dielectric interfaces were automatically digitized into traces by the equipment to generate radargrams, which represent the total waveform of a series of reflections obtained along the profiles (Conyers, 2004, 2009).

Data Processing

Static correction to compensate for the time delay of the first arrival was the first processing operation applied to the raw GPR data after the initial quality checking (QC) and preprocessing operations such as data editing and reorganization, file merging, adding header and background information as well as correct positioning (Annan, 2003). The static correction adjusts individual traces for the lag between the time when the transmitter was switched on, at time zero (to) and the first break (tfb) when the first wave was recorded (Davis and Annan, 1989). This operation accounts for the air space between the transmitter/receiver units and the ground surface and thus converts t_{fb} to t_o using the relation below.

$$t_0 = t_{fb-} \, d \Big/ v_a \tag{1}$$

Where d is the distance between the transmitter and the receiver, and V_a is the velocity of GPR signal in air, which is the media below the transmitter/receiver units and the ground surface.

The resultant data were filtered to remove non-linear/low frequency GPR signal components (cultural noise) which results due to proximity of the transmitter and the receiver to near surface/buried electrical and other cultural/house-hold utilities (Moorman, 1990). The low frequency noise which does not propagate but diffuses into the ground and induces slowly decaying wow (wave) on the high frequency components of the trace, were filtered out to increase signal to noise ratio (S/N). Thus, improving the quality of the data by the application of low cut or high pass Gaussian filter in a process commonly referred to as Dewowing (Fisher *et al.*, 1996; Cassidy, 2009). Amplitude gain was further applied to the GPR data to compensate for the signal attenuation that affected the transmitted signal as it travels to the reflector and back to the receiver. Gains were applied to boost signal strength, which generally decreases with depth, and thereby increasing the visibility of the late arrivals that are often presented as weak signals. Spatial filters were also applied to remove high frequency random noise types, such as ringing (horizontal noise, which may be associated with electromagnetic interference, system noise and surface reflections) in the data set. Background average subtraction filter that runs the average background subtraction to the data, filters out unwanted signals by subtracting the mean/average trace of the entire GPR line from every trace in the line (Benedetto *et al.*, 2017). The filter known to enhance dipping events and mute horizontal events is also effective for removing direct air waves and ground waves at the top of the GPR profiles. Conversion of the 2-way travel time to depth was also carried out using a simple mathematical relation expressed in equation 2. The expression relates the depth of investigation (d) with the 2-way travel-time (t) of the GPR reflection pulses, the dielectric permittivity of subsurface materials (ε) and the speed of light in a vacuum (c = is 3×10^8 m/s). The approach generates an initial velocity relation using initial dielectric (assumed) value of 9, which though an approximation has been reported to be reliable, especially where the electrical conductivity is low and the magnetic permeability is 1.

$$d \frac{1}{2} \frac{ct}{\sqrt{\varepsilon}} \tag{2}$$

The initial velocity relation is usually optimized using velocity information obtained from detailed propagation velocity analysis such as could be derived from velocity migration, Common Mid Point (CMP), hyperbolic velocity analysis. For this study a semblance of the CMP velocity analysis technique was employed to generate a quick velocity estimate used to improve the velocity information for time – depth conversion. The technique simply sorts out data acquired at common-source and multi-receiver data and further rearranges them into centimeter to extract velocity information. Finally, the resultant processed, filtered and gain recovered GPR data (2D radargram) were sorted based on the order of acquisition in the field and combined using Ekko Project software algorithm developed by Sensors and Software Inc. Canada, to generate 2D sections and time slices at different imaged depths.

Results and Discussions

A combination of the geophysical concepts of GPR techniques, observed cultural features during measurement as well as the knowledge of the terrain geology guided the interpretation of the various anomalies observed from the filtered and enhanced GPR data and they are presented as 2D radargrams and 2D sections / time slice maps. The radargram sections generated from the GPR survey present the subsurface image on the account of GPR reflection up to 4.88 m. The section can be roughly divided into two parts based on the reflection signals. The upper near surface (0 – 0.76 m) part of the section with characteristic poor reflection images which imaged the soil horizons and the averagely well imaged deeper (0.91 – 4.88 m) horizon (Figure 5a). The upper part of the sections presents poorly resolved low amplitude GPR reflections which can be attributed to relatively high humidity of the soils (damp) and the possible occurrence of lateritic capping unit which has ability to attenuate reflection energies (Leucci, 2008). The surveyed area is situated under a shed constructed with planks and iron roofing sheets with the topmost soil comprising of relatively dry loose sands. However, beneath the few inches of dry loose sands is possible occurrence of lateritic unit (Figure 3). The deeper part on

the other hand presents relatively high amplitude reflections which reflect the actual subsurface signals. The relatively high resolution at depth, as evident by distinct reflection signatures which remain visible with depth, suggest that the deeper unit is resistive and by extension relatively high electrical permittivity. The low conductivity of the deeper units may be associated with less clayey materials and low in water saturation as reported by Osinowo and Olayinka (2012). The deeper reflections have relatively high amplitude, they are continuous and appeared truncated at points of variation in dielectric properties of the subsurface. This can be related to the changes in earth materials beneath the imaged section or occurrence of materials which differ significantly in the dielectric properties, especially when compared to that of the surrounding earth material. The variation in the reflection characteristics or continuation has been a very reliable means of mapping occurrence of subsurface voids or cavities which have different reflection patterns from that of the surrounding rocks (Reppert *et al.*, 2000). Changes in reflection impedance as a result of variation in dielectric properties encountered between the surrounding earth materials and the walls of the burial tomb is known to generate classic hyperbolic diffraction curves/reflection events (Davis and Annan, 1989), such as the prominent classic hyperbolic

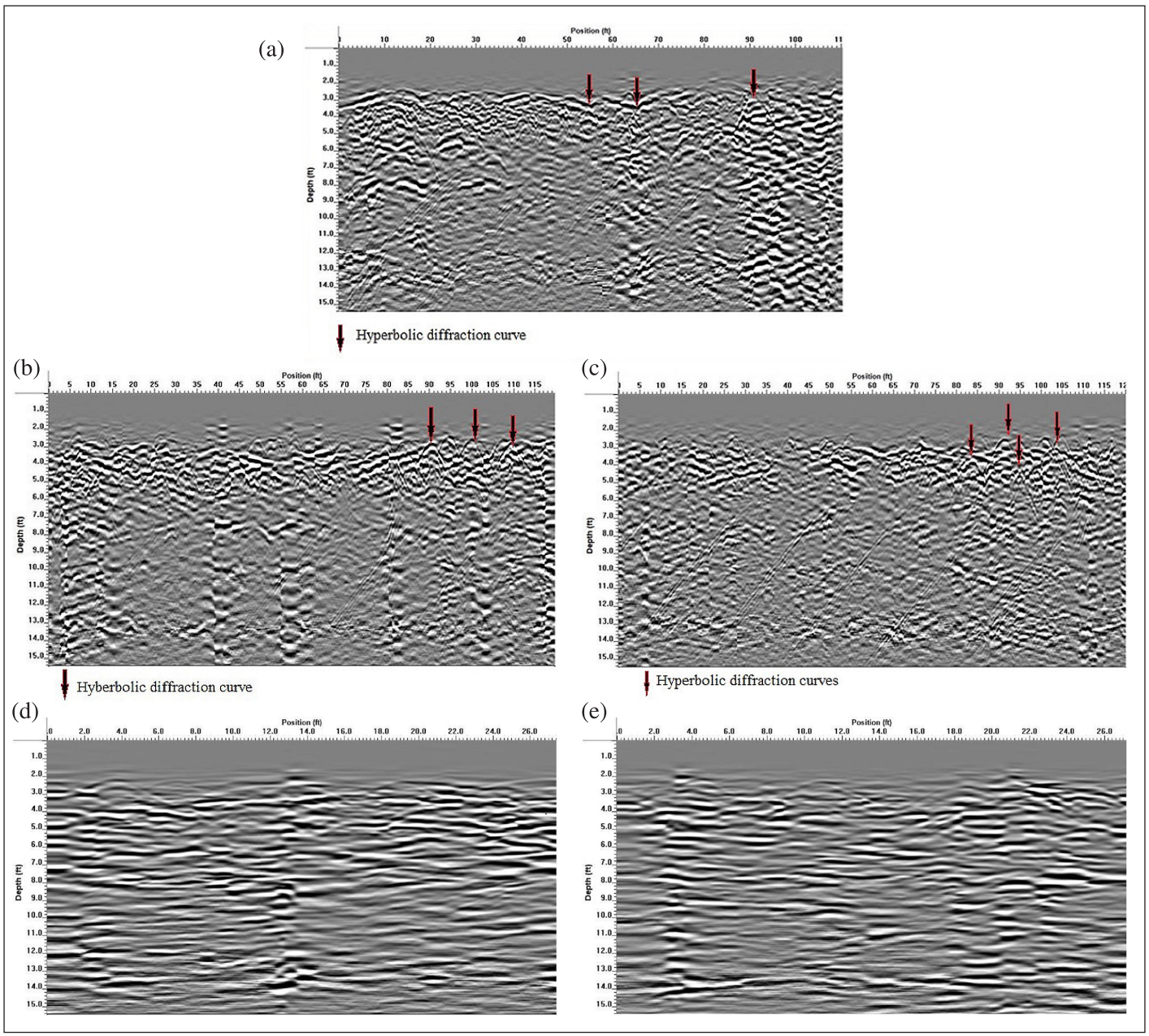

Figure 6. GPR Reflection Profiles (a) ran over the grave area (P18) (b) right of the reference profile (P17) (c) left of the reference profile (P19), (d) Profile 22 and Profile 23 established directly on the possible burial site with reflection signatures showing variation in dielectric properties relative to the host geologic materials.

diffraction curves observed around 0.91 to 1.22 m (marked with red arrows) (Figure 6). The generated diffractions and other associated perturbation beneath the hyperbolic curves appeared continuous with depth, from around 1.22 m, thus suggesting occurrence of prominent material of differing reflection amplitude, such as could be attributed to grave/tomb walls, voids or occurrence of burial materials existing between the walls of the grave. The occurrence of classic hyperbolic diffraction curves in profiles established around the cordoned off burial place, specifically to the right (Figure 6b) and the left (Figure 6c) of the reference profile (Figure 6a) further established the possible existence of materials which differ in dielectric properties from the host geologic materials, especially such variation which may be consistent with burial activities. Visible high amplitude and extensive reflection anomalies also characterize the different depth sections and different parts of profiles 22 and 23 that were established directly over the cordoned off, possible burial site (Figures 6e & 6d). The anomalies possibly indicate occurrence of subsurface voids created by excavation which may be poorly filled with foreign or disturbed earth materials. Other noticeable reflection events generally observed on the GPR profiles may be attributed to airwave events commonly associated with reflection energies that travel through the air and returned to the receiver by overhead metallic roofing sheets that covered the burial site (Sun and Young, 1995).

The desired target in this study is a burial tomb which is better evaluated in 2D dimensional form. The combination of all the individual radargram sections generated a 3D image from which time slices of different depths were extracted for the purpose evaluating the GPR reflections patterns at various depths. Eighteen GPR time slices generated at 0.061 m interval from 0.73 m to 1.83 m and stacked at six (6) traces each, are presented in figures 7 (a – c). Figure 7a presents the first stack traces with the shallowest trace extracted at 0.73 m. This is because shallower than 0.73 m the GPR reflections were attenuated and poorly resolved. The first stacked traces (Figure 7a) show characteristic low amplitude reflections which dominates the entire slice except for isolated relatively high reflection amplitude in extreme north of the surveyed area. The stacked traces indicate gradual increase in reflection amplitude with depth that suggests increase in resolution with depth which may result from reduction in clay content and probably decrease in water saturation, since the lateritic unit is known to inhibit adequate groundwater recharge after rainfall (Osinowo and Olayinka, 2012). The relatively high reflection amplitude observed within the depth range (upper 1.04 m) in the presented GPR time slices in the first stack (Figure 7a), probably relates to near surface bioactivities such as burrow of animals or occurrence of artifacts. The second stack (Figure 7b) shows traces extracted from 1.04 m to 1.4 m. It shows progressive deeper part of the subsurface beneath

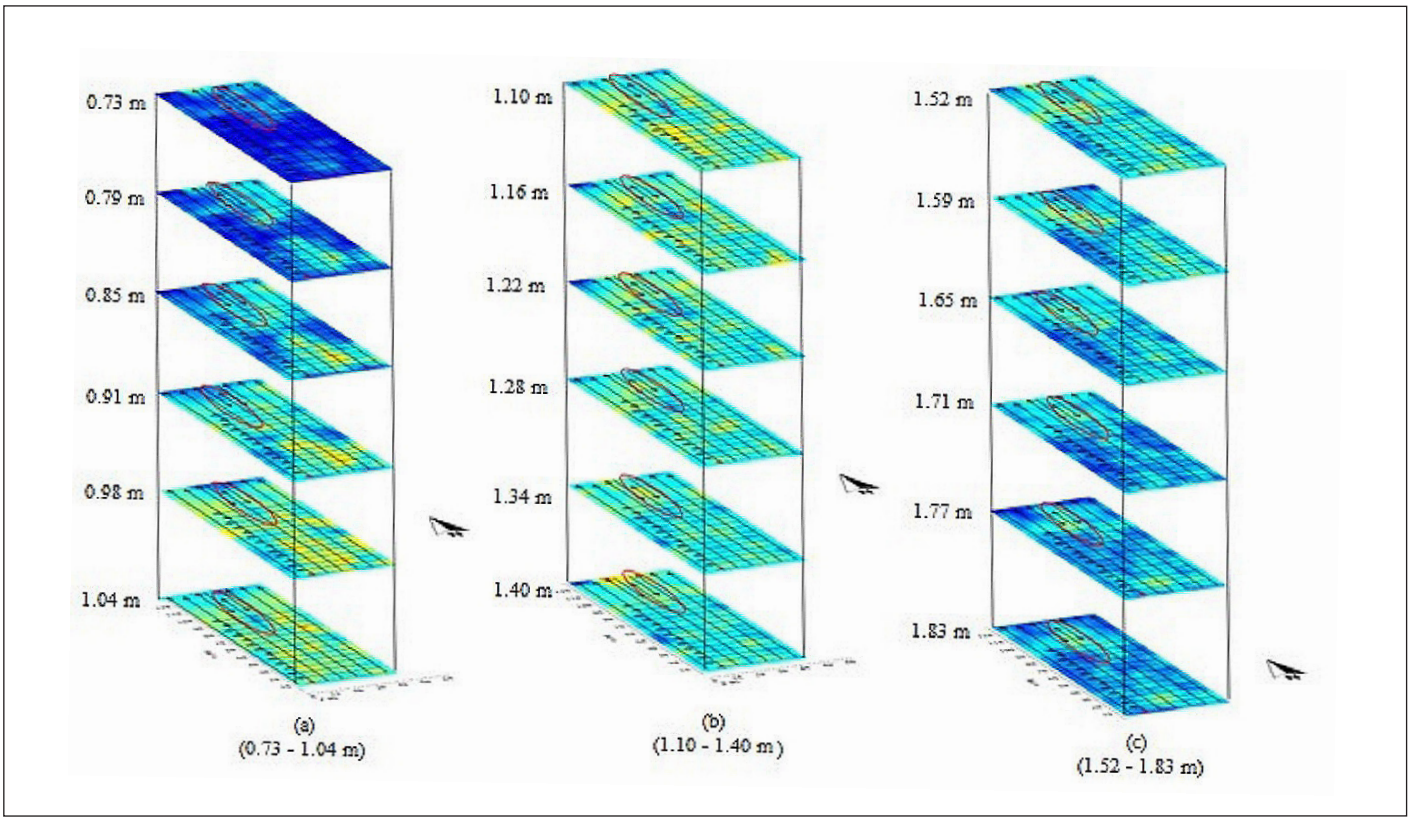

Figure 7. (a-c) Iso depth GPR reflection time slices (a) 0.73 – 0.91 m, (b) 1.10 – 1.40 m, (c) 1.52 -1.83 m with the circle defining the possible location of the tomb.

the surveyed area. The slices present relatively higher GPR reflection amplitude which suggests less attenuation of the GPR reflection energy, especially when compared with degree of attenuation in the upper very near surface (<0.73 m). Variation in the reflection amplitude generally characterizes the iso-depth reflection slices extracted from this depth interval. This variation can be attributed to the varying dielectric properties of the subsurface materials at these intervals. This variation may relate directly or indirectly with break in distribution of geologic material at the intervals. Occurrence of voids or foreign material of contrasting dielectric properties will properly present contrasting GPR reflection amplitude (Moran *et al.*, 1993; Novo *et al.*, 2011). The cordoned off part of the surveyed area, believed by locals to be the ground directly above the Queen Sheba's tomb (Figure 3a), presents unique GPR reflection amplitude. The region marked with circle presents gradual increase in reflection pattern with depth (Figures 7b) and it is found to continue with depth and consistent in pattern up to 1.83 m (Figure 7c). The relatively high amplitude reflection pattern observed around the location of the burial tomb, demarcated with circle indicates variation in dielectric properties, especially when compared with the surrounding host/subsurface geology. This could be attributed to the alteration in the original geology through digging of the grave and introduction of foreign materials, such as tomb walls. Prominent and consistent high GPR reflection amplitude around the cordoned part of the burial site is apparent on the GPR time slices extracted at 1.24 m, 1.30 m, 1.36 m and 1.43 m as shown in figure 8. The anomaly in GPR reflections could be attributed to the occurrence of tomb walls as well as occurrence of void around the walls of the grave (Bladon *et al.*, 2011).

Conclusion

Variation in subsurface dielectric properties, determined from ground penetrating radar reflection measurements across a burial site claimed by the Christian, Muslim and Traditional believers as the burial place of the biblical Queen Sheba (Bilikisu Sungbo) in Oke-eri in Ijebu-Ode, southwestern Nigeria, has proved very effective in establishing the occurrence of a grave beneath the cordoned part of this heritage site. The hyperbolic diffraction curves as well as the consistent and relatively high amplitude GPR reflection pattern, though not able to establish who was buried in the tomb, suggest the occurrence of tomb walls, and possible anthropogenic foreign material that is consistent with occurrence of a burial place beneath the cordoned off part of the site.

Acknowledgements

The authors gratefully acknowledge the anonymous reviewers for insightful suggestions that helped improved the quality of the paper. The editorial team is thankfully appreciated.

References

Annan, A.P. (2003). Ground penetrating radar: Principles, procedures, & applications, Sensors & Software Inc. Technical Paper.

Aremu, D.A. (2002). Saving Sungbo Eredo: A Challenge to Nigerian Archaeologists. *West African Journal of Archaeology 32*(2): 63-73.

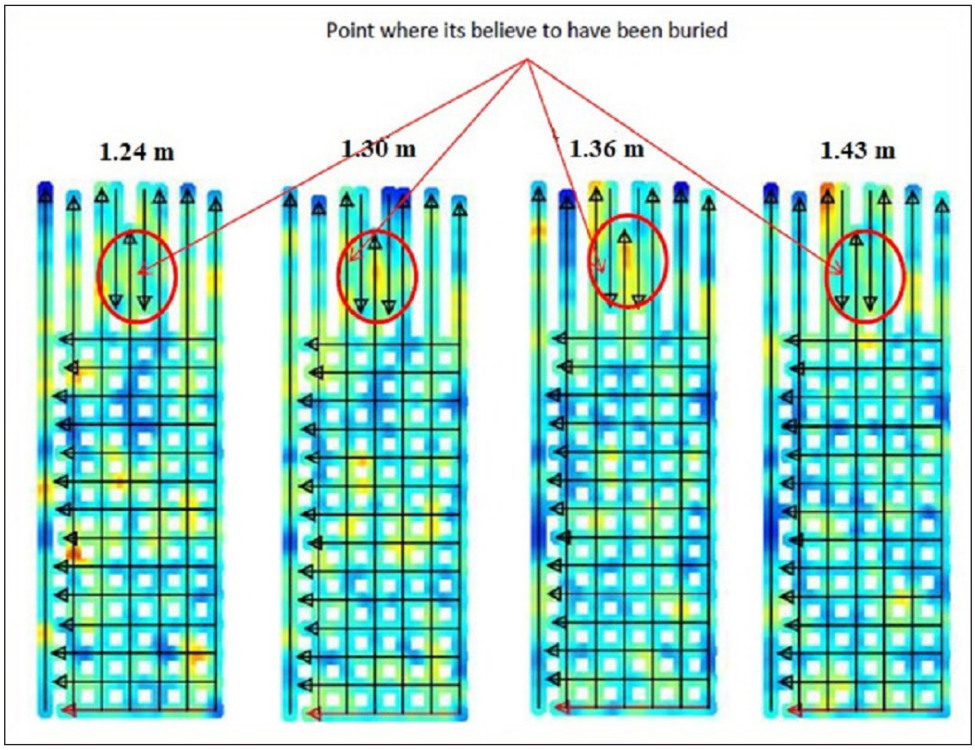

Figure 8. GPR reflection amplitude distribution of time – slice at depths 1.24 m, 1.30 m, 1.36 m and 1.43 m.

Aremu, D.A., J. Ogiogwa, J.O. Aleru, B.J. Tubosun, A. Ogunfolakan, and P.A. Oyelaran, (2013). Sungbo Eredo, Materiality, Ecology and Society in Prehistoric South Western Nigeria. *West African Journal of Archaeology 43*: 1-21.

Belcher, W. L. (2010). "From Sheba They Come: Medieval Ethiopian Myth, US Newspapers, and a Modern American Narrative". *Callaloo*. 33 (1): 239–257. doi:10.1353/cal.0.0607. JSTOR 40732813. S2CID 161432588.

Benedetto, A.; Tosti, F.; Bianchini Ciampoli, L.; D'Amico, F. (2017). An overview of ground-penetrating radar signal processing techniques for road inspections. Signal Process. 2017, 132, 201–209.

Bladon, P., Moffat, I., Guilfoyle, D., Beale, A. and Milani, J. (2011). Mapping anthropogenic fill

with GPR for unmarkedgrave detection: A case study from a possible location ofMokare's grave, Albany, Western Australia. *ExplorationGeophysics 42*: 249–257.

Conyers, L. B. (2004). *Ground-Penetrating Radar for Archaeology*. AltaMira Press, Lanham.

Conyers, L. B. (2006). Ground-Penetrating Radar Techniques to Discover and Map Historic Graves. *Historical Archaeology 40*(3):64-73.

Conyers L.B. (2012). *Interpreting Ground-penetrating Radar for Archaeology*. Left Coast Press, Walnut Creek, California.

Davis, J. L., and Annan, A.P. (1989). Ground-penetrating radar for high-resolution mapping of soil and rock stratigraphy: *Geophysical Prospecting, 37*, 531 - 551.

Darling P.J. (1997).Sungbo's Eredo: Africa's Largest Monument. *The Nigerian Field 62*, 113-129.

Darling, P. J. (1999). Archaelogists find clues to Queen of Sheba in Nigeria, Find May Rival Egypt's Pyramids'' www.hartford-hwp.com.

Darling, P.J. (2001).Sungbo's Eredo: Evidence of Past Dune Formation near the Coast? In Darling (ed.) *Past Shifts of Desert and Forest Across Nigeria* 112-120. School of Conservation Science, Bournemouth University.

Fisher, S. C., Stewart, R. R., and Jol, H. M., (1996). Ground penetrating radar data enhancement using seismic techniques. *Journal of environmental and engineering geophysics*, p. 89 – 96.

GSSI (2011). Geophysical Survey Systems, Inc., SIR System-3000 Manual. 97pp.

GSSI (2017). Geophysical Survey Systems Antennas Manual. MN30-903 Rev G. 99pp.

Leckebusch, J. (2003). Ground-penetrating radar: A modern three-dimensional prospection method. Archaeol. Prospect. 10, 213–240.

Leucci G., (2008). Ground penetrating radar: the electromagnetic signal attenuation and maximum penetration depth Scholarly Research Exchange: Volume 2008 • Article ID 926091 • doi:10.3814/2008/926091.

Masini N, Persico R, Rizzo E. (2010). Some examples of GPR prospecting for monitoring of the monumental heritage, *J. Geophys. Eng., vol. 7* (pg. 190-199)10.1088/1742-2132/7/2/S05.

Moran, M.L., and Greenfield, R.J. (1993). *Radar signature of a 2.5-D tunnel: Geophysics*, v. 58, no. 11., p. 1573-1587.

Moorman, B. J. (1990). Assessing the ability of ground penetrating radar to delineate subsurface fluvial lithofacies.

Novo A, Lorenzo H, Rial FI, Solla M. (2011). 3D GPR in forensics: Finding a clandestine grave in a mountainous environment. *Forensic Science International 204*:134-138.

Ogundele, S.O. andBabalola, B. A. (2007). Sociology and Archaeology of Defensive Ditches and Embankments in Orile-Keesi, Abeokuta, Nigeria. *Nyame Akuma* 67: 60- 69.

Omatsola, M. E and Adegoke, O. S. (1981). Tectonic and Cretaceous stratigraphy of Dahomey basin *J. Min. Geol. 54* 65–87.

Osinowo, O. O,, Akanji, A. O. and Akinmosin, A. (2011). Integrated geophysical and Geotechnical investigation of the failed portion of a road in basement complex terrain,southwestern Nigeria, *RMZ-Mater. Geoenvironment 58* 143–62.

Osinowo, O. O. and Olayinka, A. I. (2012). Very low frequency electromagnetic (VLF-EM) and electrical resistivity (ER) investigation for groundwater potential evaluation in a complex geological terrain around the Ijebu-Ode transition zone, southwestern Nigeria. *Journal of geophysics and engineering*, pp. 374–396.

Osinowo, O. O. and Olayinka, A. I. (2013). Aeromagnetic Mapping of Basement Topography around the Ijebu-Ode Geological Transition Zone, Southwestern Nigeria. *Acta Geodaetica et Geophysica* Vol. 48, No. 3: 451-470.

Oyawoye, M.O. (1972).The basement complex of Nigeria. In: Dessauvagie TFJ, Whiteman AJ eds) African geology. Ibadan UniversityPress, pp. 66–102.

Pérez-Gracia V, Caselles O, Clapés J, Osorio R, Canas J A, Pujades L G. (2009). Radar exploration applied to historical buildings: A case study of the Marques de Lió palace, in Barcelona (Spain), Eng. Fail. Anal., vol. 16 (pg. 1039-050)10.1016/j.engfailanal.2008.05.007.

Rahaman M.A. (1988).*Recent advances in the study of the basement complex of Nigeria*. In: Geological Survey of Nigeria (ed) Precambrian Geol Nigeria, pp. 11–43.

Reppert, P. M., Morgan, F. D. and Toksoz, M. N. (2000). Dielectric constant determination using ground-penetrating radar reflection coefficients, *Journal of Applied Geophysics*, vol. 43, no. 2–4, pp. 189–197.

Seligsohn, M. and Montgomery, M. W. (1906). ''SOLOMON'', in Isidore Singer: *et al.* (eds.), Jewish Encyclopedia, 11, p.4361 – 448a. Wikipedia, (2021): www.wikipedia/en.

Sun, J., and Young, R. A. (1995). Recognizing surface scattering in ground-penetrating radar data. *Geophysics*, Vol 60; 1378-1385.

Editörler: Biddle, K.T., ChrisiteBlick, N.). Society of Economic Paleontologists and Mineralogists, Special Publication, 227- 264.

Şentürk K. and Karaköse C., 1987, Çanakkale Boğazı ve dolayının jeolojisi, MTA Genel Müdürlüğü, Jeoloji Etüdleri Dairesi Arşivi, yayınlanmamış teknik rapor, 371, 207 s.

Thabet M., 2019, Site-Specific Relationships between Bedrock Depth and HVSR Fundamental Resonance Frequency Using KiK-NET Data from Japan. Pure Appl Geophys. **https://doi.org/10.1007/s00024-019-02256-7**

Tunusluoğlu M. C. and Karaca Ö., 2018, Liquefaction severity mapping based on SPT data: a case study in Canakkale city (NW Turkey), Environmental Earth Sciences, 77(12). **https://doi.org/10.1007/s12665-018-7597-x**

Ullah I., 2017, Near-surface characterization from the H/V spectral curves along with the joint inversion of the ellipticity and dispersion curves. Doktora Tezi, São Paulo Üniversitesi, Brezilya.

Wathelet M., Chatelain, J. L., Cornou, C., Di Giulio, G., Guillier, B., Ohrnberger, M., Savvaidis, A., 2020, Geopsy: A User-Friendly open-source tool set for ambient vibration processing, Seismological Research Letters, 91(3), 1878-1889.

Yiğitbaş E., 2016, Jeolojik – Antropojenik Sebep – Sonuç İlişkileri Açısından Çanakkale

Geofísica Internacional (2023) **62-1**: 387 - 401

Bedrock Depth Calculation of Çanakkale (Turkey) Basin Using Rayleigh Ellipticity and Microgravity Survey

Aydın Büyüksaraç[1], Onur Eyisüren[2], Özcan Bektaş*[3] and Öznur Karaca[4]

Abstract

It is a well-known fact that the local ground effect plays an important role in the damage to structures during earthquakes. In order to define the soil-structure interaction correctly, the geometry of the tight and loose soil layers in the soil should be well known. In addition, the impedance contrast due to local ground effects can be deeper than the first 30 m, which is accepted as the engineering depth, and in this case, the Vs,30 parameter is disabled. For this reason, the location of engineering bedrock and seismic bedrock gains importance. The variation of shear wave velocity with depth is a key parameter for seismic field effect estimation. In addition, the separation of low-density layers close to the surface and higher-density bedrock can be easily done by the gravity method. Bedrock/seismic foundation levels were determined by using these two methods together for Çanakkale soils, which are known to have thick alluvial thickness and liquefaction problems. Microgravity measurements were made at 100 points and the anomalies obtained were modelled in three dimensions. In light of the data obtained from this study, it has been determined that the thickness of the loose basin unit in the study area is in the range of about 50-300 m. Ambient vibration was recorded with the help of a velocity seismometer at 146 points, and S velocity (Vs) profiles were obtained by using the inversion of the observed ellipticity curve. In addition, the velocity-depth change rate structure of the basin is defined depending on the Vs velocities on the 2D gravity model made along the two profiles that cut the basin in N-S and E-W directions. Along these profiles, the frequency range has been determined as 0.8-1.3 Hz in the deep parts of the Basin and 1.5-11.0 Hz in the shallow parts.

Key words: Bedrock, Microgravity, Rayleigh Ellipticity, S-Velocity, Seismic Foundation

Resumen

Es bien conocida la importancia de los efectos locales del suelo en el daño a estructuras por sismos. Para definir correctamente la interacción suelo-estructura, es necesario establecer la geometría de las capas compactas y sueltas del suelo. Además, el contraste de impedancias debido a efectos locales del suelo puede exceder los 30 m de profundidad, que es la profundidad aceptada en ingeniería, y por ello, en este caso, se deshabilita el parámetro Vs,30. De allí la importancia de ubicar el lecho rocoso de ingeniería y el lecho rocoso sísmico. La variación de la velocidad de la onda de corte con la profundidad es un parámetro clave para la estimación del efecto de campo sísmico. Además, la separación de capas de baja densidad cercanas a la superficie del lecho rocoso de mayor densidad se puede realizar rápidamente mediante el método de gravedad. Para los suelos de Çanakkale, que tienen problemas de licuefacción y espesor aluvial grueso, los niveles de lecho rocoso/cimentación sísmica se determinaron usando ambos métodos. Las mediciones de microgravedad se realizaron en 100 puntos y se modelaron las anomalías obtenidas en tres dimensiones. A la luz de los datos obtenidos de este estudio, se determinó que el espesor de la unidad de material suelto en la cuenca del área de estudio está en el rango de aproximadamente 50-300 m. La vibración ambiental se registró con un sismómetro (sensor de velocidad) en 146 puntos, y los perfiles de velocidad S (Vs) se obtuvieron de la inversión de la curva de elipticidad observada. Además, la estructura de tasa de cambio de la velocidad con la profundidad en la cuenca se definió en función de las velocidades Vs en el modelo de gravedad 2D a lo largo de dos perfiles que cortan la cuenca en las direcciones N-S y E-W. A lo largo de esos perfiles, el rango de frecuencias se ha determinado de 0.8 a 1.3 Hz en las partes profundas de la Cuenca y de 1.5 a 11.0 Hz en las partes someras.

Palabras clave: Lecho rocoso, Microgravedad, Elipticidad de Rayleigh, Velocidad-S, Lecho rocoso sísmico

Received: January 30, 2022; September 6, 2022; published on-line: January 1, 2023.

Editorial responsibility: Anonymous

* Corresponding author: Özcan Bektaş obektas@cumhuriyet.edu.tr
[1] Çan Vocational School, Çanakkale Onsekiz Mart University, TR-17400 Çan/Çanakkale, Turkey. e-mail:absarac@comu.edu.tr
[2] School of Graduate Studies, Çanakkale Onsekiz Mart University, TR-17020 Çanakkale, Turkey. e-mail: onureyisuren@gmail.com
[3] Department of Geophysical Engineering, Sivas Cumhuriyet University, TR-58140 Sivas, Turkey. e-mail:obektas@cumhuriyet.edu.tr
[4] Department of Geological Engineering, Çanakkale Onsekiz Mart University, TR-17020 Çanakkale, Turkey. e-mail:oznurkaraca@comu.edu.tr

https://doi.org/10.22201/igeof.2954436xe.2023.62.1.1447

Introduction

While determining the behaviour of a site during the earthquake occurrence, it is generally acted according to the ground information near the surface. However, shallow and deep ground structures of that area must be well known to fully define the ground behaviour of a site. In particular, the distance of the near-surface soils to the bedrock is one of the most important factors that determine the ground behaviour during an earthquake occurrence. The depth of the bedrock and the presence of soft-medium solid clay deposits or liquefiable soils with low shear wave velocity on them and the inclusion of basin effects increase the PGV values and extend the period of the acceleration spectra.

Urban settlements generally develop towards looser, unstable, in other words, lowland regime areas in Turkey. For this reason, the foundation designs of buildings in urban settlements are made in areas with soil structure. This situation brings engineering problems that need to be solved at the design stage. In particular, the soil thickness under the buildings is very important information and factor in terms of defining the response of the site in terms of construction. For this reason, it is also important to determine the depth where the soil completely passes into the rock ambient (bedrock) or S-wave velocity reaches 600-760 ms^{-1}. The damage caused by the earthquakes that took place in Turkey in the last 25 years has revealed how important it is to know the underground model and the basin effect, too. On the other hand, it is imperative to generate the bedrock depth information to obtain a complete ground structure model in basin-type structures and to model information such as possible soil amplification and acceleration distribution. For this purpose, many studies have been carried out to obtain bedrock depth with experimental relations from inversion based on ambient vibration measurements (Delgado *et al.*, 2000a; Hinzen *et al.*, 2004; García-Jerez *et al.*, 2006; D'Amico *et al.*, 2008; Birgören *et al.*, 2009; Özalaybey *et al.*, 2011; Harutoonian *et al.*, 2013; Fairchild *et al.*, 2013; Del Monaco *et al.*, 2013; Mendecki *et al.*, 2014; Kuo *et al.*, 2016; Sant *et al.*, 2017; Molnar *et al.*, 2018; Liang *et al.*, 2018; Moon *et al.*, 2019; Thabet, 2019; Anbazhagan *et al.*, 2019; Rupar and Gosar, 2020; Büyüksaraç *et al.*, 2021; Maghami *et al.*, 2021).

Seismic microzonation or multi-parameter microzonation studies based on the inversion of surface waves have been carried out for many residential areas in Turkey. In these studies, ground motion parameters, site conditions, and their effects were evaluated using different soil classifications, and especially the surface and near-surface changes of soils were zoned (Över *et al.*, 2011; Büyüksaraç *et al.*, 2013; Akkaya and Özvan, 2019; Bekler *et al.*, 2019). In multi-parameter microzonation studies, a kind of risk ranking was carried out by evaluating multiple data within the framework of selected criteria (Kolat *et al.*, 2006). Later, when it was understood that this layer was especially effective on the bedrock or seismic bedrock, where the effect of amplifying the earthquake ground motion of the unstable ground sections was important, studies were developed to obtain V_s velocity measurements for the foundation limitation. The variation of regional S-wave velocity with depth and the bedrock, and depth distribution play an important role in the estimation of seismic hazard and earthquake ground motion characteristics in terms of understanding the seismic wave amplification potential of geological formations (Birgören *et al.*, 2009). Kamalian *et al.* (2008) mentioned the seismic bedrock in their study for the city of Qom, Iran, defined the levels that reached 760 m/s, and examined the behavior of the earthquake ground motion above this level. Similarly, Nakamura (2000) defined the S-velocity value of 600 m/s as the seismic basis. Especially in the upper part of this level, it was emphasized in most studies that the damage rate increased in the ground parts close to the surface.

Çanakkale is an area with a very high earthquake risk due to the earthquake sources around it (Figure 1). The ground structure of Çanakkale, which is quite loose and unstable, shows ground characteristics under the influence of shallow groundwater, and most importantly, it is known that there is not enough information about the depth of the bedrock. Site surveys within the boundaries of Çanakkale central zoning were completed within the scope of some projects in 2014. In this context, shallow soil structure and behavior were determined by single station microtremor and seismic MASW method. On the other hand, many researchers have conducted studies to determine the earthquake behavior, soil classification, and problems of shallow soil structure in the study area (Tunusluoğlu and Karaca, 2018; Bekler *et al.*, 2019; Büyüksaraç *et al.*, 2021).

Geophysical studies covering two different methods were carried out to eliminate this deficiency and to calculate the bedrock or seismic bedrock depth in the section between Karacaören and Kepez Plains, where Çanakkale central settlement is located within the scope of this study. First, microgravity measurements were made to determine the density contrast between loose and hard units. Considering that the volcanic units in the east of the Çanakkale Basin may be the basement rock, three-dimensional modeling has been made. Then, the V_s velocity structure was obtained from the measurements based on the ambient vibrations in the environment. Compatibility analysis was made by comparing the results obtained with both methods and the ground structure was defined on the two-dimensional models.

Seismicity and Seismotectonic of Çanakkale Basin

The Biga Peninsula, where the Çanakkale Basin is located, is one of the most active parts of the North-West Anatolian seismotectonic regime dominated by a strike-slip structure

bounded by normal or oblique faults (McKenzie, 1978; Şengör *et al.*, 1985; Barka *et al.*, 1997; Kürçer *et al.*, 2008; Ateş *et al.*, 2009; Le Pichon and Kreemer, 2010; Fairchild *et al.*, 2013). Çanakkale city, which is our study area, is located in Northwest Anatolia, in other words, in the northern Aegean Region. The Biga Peninsula, to which Çanakkale belongs geographically, is in the southern part of the North Anatolian Fault Zone (*NAFZ*), the most important fault zone in Turkey. When the distribution of earthquakes in and around Çanakkale is examined, four sub-seismic zones can be mentioned. These are *NAFZ* in the north, the Yenice-Gönen Fault Zone (*YGFZ*) in the east, and the Ganos Fault (*GF*), which is the continuation of the *NAFZ* in the north, in the northwest, respectively. The most important active fault that may affect the study area is the Ganos Fault along the Gaziköy-Gölcük-Kavakköy line, two of the most active fault systems in Southern Marmara, and the SW-NE trending Yenice-Gönen Fault Zone. These faults are approximately 50 km away from the study area. (Figure 1). On the other hand, Çanakkale is affected by all earthquakes in the Aegean Sea. As can be seen from the map given in Figure 1, Çanakkale is under the influence of seismogenic zones that produce devastating earthquakes. When the historical records are examined, it is understood that the ancient settlement, especially known as the ancient city of Troy, was destroyed and rebuilt 9 times. Therefore, information such as soil thickness and soil behaviour become much more important for such areas.

Geology Of Çanakkale And Its Surroundings

The main geological elements of the Biga Peninsula are Metamorphic rocks, Ophiolites, Neogene basin sediments, and Magmatic rocks that started from the Oligo-Miocene and continued their development at intervals until the Quaternary (Siyako *et al.*, 1989). Paleozoic or possibly older metamorphic rocks form the basement of the Biga Peninsula (Kazdağ Group). Over the metamorphic rocks, there is the Triassic aged Karakaya Complex, which consists of different tectonostratigraphic units represented by active continental margin deposits with a tectonic contact (Figure 2). In the Upper Cretaceous, the Çetmi ophiolitic mélange was emplaced in the region with a complex and irregular internal structure mainly composed of spilite, greywacke, pelagic shale, serpentinite and radiolarites. The products of the acidic magmatism active in various stages in the Biga Peninsula are mostly granite, granodiorite and diorite compositions. Researchers studying in the region in the previous years (Birkle and Satır, 1995; Genç and Yılmaz, 1994) discovered the Kestanbol, Evciler, Karaköy and Eti plutons, the product of Tertiary magmatism and the Biga defined as shallow intrusions formed due to Lower Miocene volcanism in the peninsula. Plutons are NE-SW long axis elliptical igneous masses and they are surrounded by fine-grained volcanic rocks of similar composition (Karacık and Yılmaz, 1998). Çanakkale Group is located on older polygenic basement rocks with angular unconformity.

The formations in the Çanakkale Group are located on both sides of the Dardanelles Strait and from bottom to top consist of four litho-stratigraphic units including "Gazhanedere fm., Kirazlı fm., Çamrakdere fm. and Alcitepe fm.". From a stratigraphical point of view, the lowest levels of the Çanakkale Group are composed of the Gazhanedere formation, which was deposited in a terrestrial environment and represented by conglomerate, sandstone and mudstone, aged between the Middle Miocene and the beginning of the Late Miocene. The mudstone-supported conglomerate is loosely cemented and locally mud conglomerate. The Gazhanedere formation typically reflects the alluvial fan in terms of facies features and deposition geometry. The transition of the unit into fine-grained lithologies towards the coarse-grained basin at the basin margins indicates the alluvial fan environment (Atabey *et al.*, 2004). The longitudinal and/or transverse bar deposits found in it indicate that this spectrum developed in a braided river environment, and many depositional structures such as the indeterminate thick layer, the presence of cross layers, and the presence of wedged layers in places indicate that this environment is irregular and high-energy. The presence of red mudstones in it indicates both terrestrial formation and flood plain.

The Kirazlı formation is mostly composed of fine-coarse grained sandstone and lesser amounts of fine conglomerate, siltstone and mudstone. It was deposited in coastal and near-shore (coast, beach, tidal delta) environments. It is widely observed in the study area. The Kirazlı formation is a loosely anchored unit dominated by sandstones deposited in near-coastal environments. Among the sandstones, siltstone, claystone intercalations and conglomerates in the form of channel fillings are rarely observed. The thickness of the formation varies from region to region. It is approximately 220 m in type section near Kirazlı Village. Şentürk and Karaköse (1987) measured 132 m around Intepe, 157 m in Bayrak Tepe and 204 m in Çamrakdere. They stated that the thickness of the Gallipoli Peninsula could reach up to 500 m. The Kirazlı formation is transitional with the Gazhanedere formation at the bottom and the Çamrakdere and Alçıtepe formations at the top (Siyako, 2006).

Çamrakdere formation is transitional with Kirazlı formation at the bottom and Alçıtepe formation at the top (Siyako, 2006). The dominant lithology in the unit is mudstone-claystone and consists of siltstone, sandstone, conglomerate with pebbles and calcarenite. The claystone-mudstone layers of the unit play a primary role in the development of the landslides

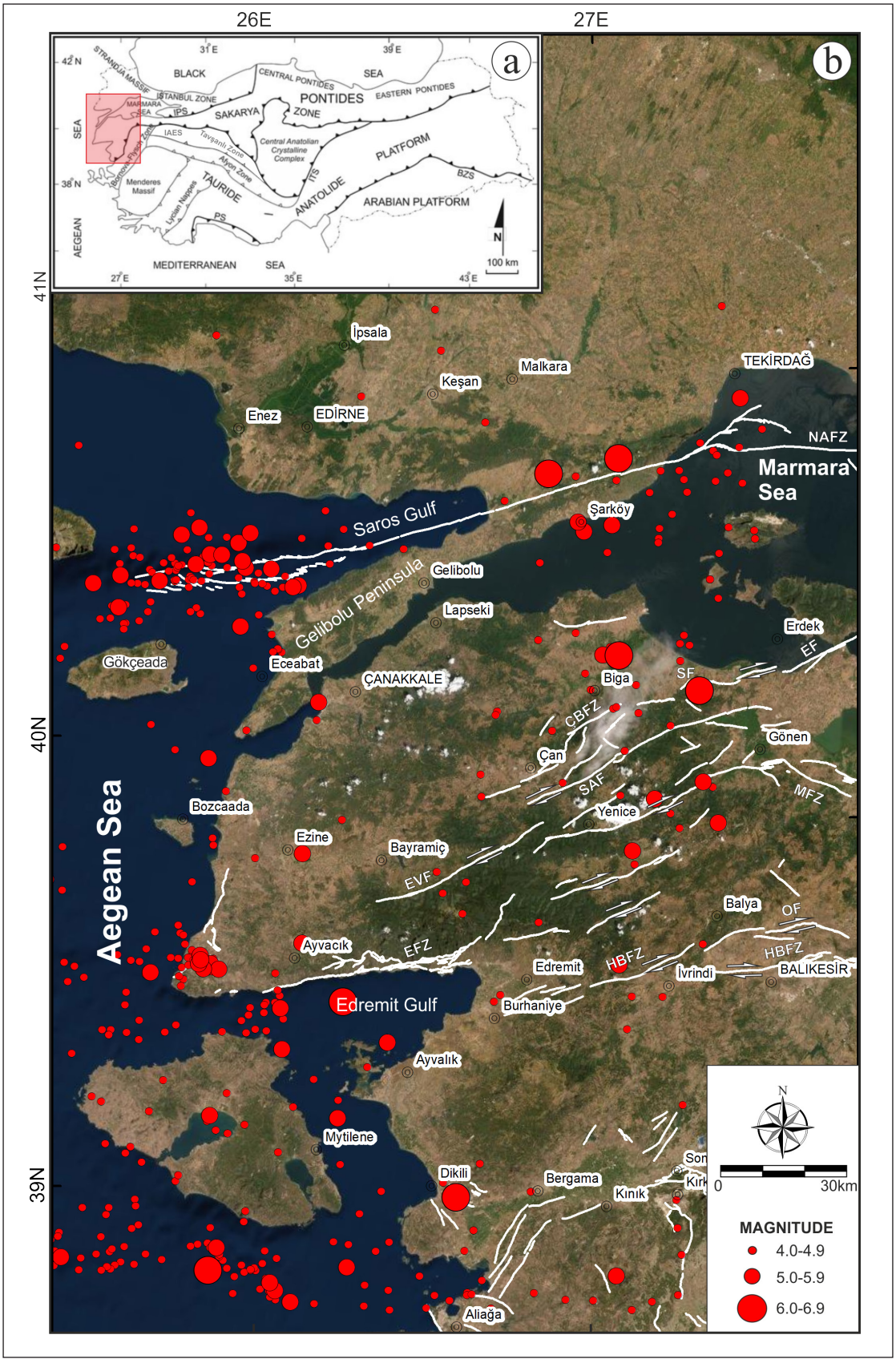

Figure 1 (a). Tectonic Units of Turkey. Red rectangular box shows the study area, (b) Epicentral distribution (between 1900 and 2021 years for M ≥ 4.0) and faults of Biga Peninsula and its environment. *NAFZ*: North Anatolian Fault Zone, *GF*: Ganos Fault, *CBFZ*: Çan-Biga Fault Zone, *SAF*: Sarıköy Fault, *YGFZ*: Yenice-Gönen Fault Zone, *SF*: Sinekçi Fault, *EF*: Edincik Fault, *EVF*: Evciler Fault, *MFZ*: Manyas Fault Zone, *EFZ*: Edremit Fault Zone, *HBFZ*: Havran-Balya Fault Zone, *OF*: Ortaca Fault

observed in the region. The formation was measured as 55 m at Bayrak Tepe near Çanakkale and 222 m at Çamrakdere in Lapseki district (Siyako, 2006).

The Alçıtepe Formation starts with beige-gray coloured, medium bedded, pebbly and sandy carbonates at the base, transitioning with the clastics of the Çamrakdere Formation. The units that make up the formation are mudstone, marl, siltstone, sandstone, calcite and fine conglomerate. These lithologies are laterally and vertically transitive with each other. It can be seen in the military area around Narababa Hill, in the area where Esenler District is located and around the Barbaros Martyrdom.

The Alçıtepe formation consists of alternations of sandy limestone, sandstone, claystone, marl and limestone with abundant macrofossils and oolitic limestones (Siyako, 2006). The Alçıtepe formation was deposited in a mixed, clastic-carbonate shoreline environment consisting of coastal and offshore clastics and carbonates (Şentürk and Karaköse, 1987). The fact that it contains lagoonal sediments fed by rivers at the bottom and oolitic limestones consisting of turbulent shoreline and offshore sediments at the top indicates that the unit was deposited not only beyond the coast, but also in an area along the clastic coastline. The repetition of clastic sediments and carbonate sediments at some levels indicates that the coastline is volatile (moving) (Şentürk and Karaköse, 1987).

Alluviums consisting of unconsolidated sediments are very common in the study area. Both the distribution and formation of these alluviums took place under the influence of Sarıçay. Sarıçay collects the sediments it carries from high elevations, both along its old bed and along its new bed, primarily at low-lying plains. These deposits are grouped into three separate units according to their formation forms and the locations of the lithology types that compose them (Figure 3). 1st group, sand, clayey sand, partially gravel channelled sand unit, 2nd group, sand, silty sand unit, and 3rd group, block, gravel and sand (existing riverbed and floodplain sediments) unit (Büyüksaraç *et al.*, 2022). As you

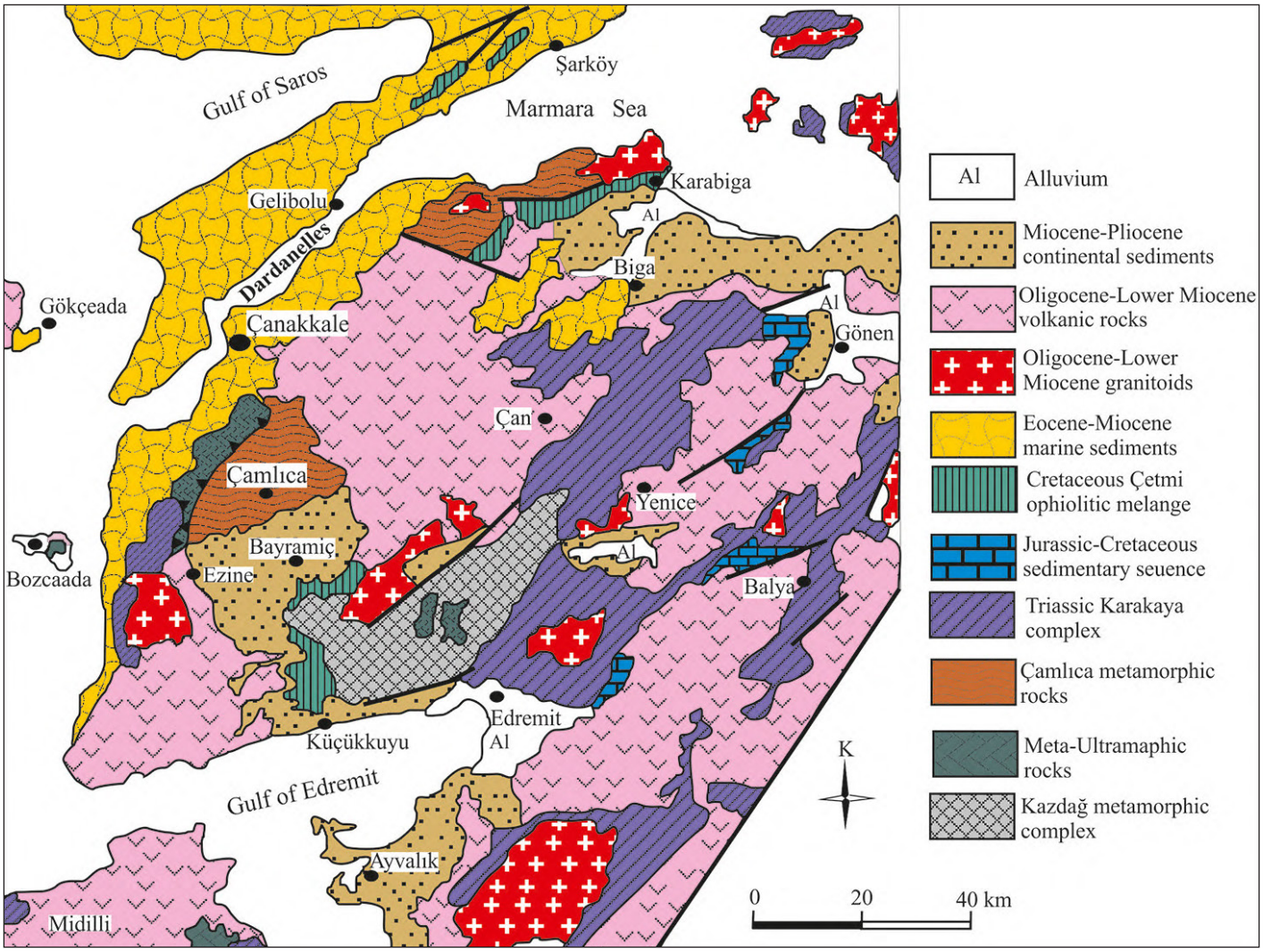

Figure 2. Geological map of Çanakkale and its surroundings, including the Biga and Gallipoli peninsulas (Atabey *et al.*, 2004; Duru *et al.*, 2012; Ilgar *et al.*, 2008; 2012; Yiğitbaş, 2016).

move away from the main bed of Sarıçay, the grain size in the sediments decreases, and block gravel, sand, silt and clay elements show lateral and vertical transitions with each other.

3D Bedrock Depth Map of Çanakkale Basin Based on Gravity Data

Gravity data were collected with the grid network created in an area of approximately 10×10 km, that aims to reach the borders of the Çanakkale basin, which includes the study area and its surroundings (Figure 4). The distance between profiles and measurement points was equal and taken as 1 km. Field data collection protocols were carried out by making 60-second, 5-repetitive measurements at 100 stations using the Scintrex CG-5 gravimeter.

In addition, a base measurement was made averagely every 2 hours to control the instrumental drift at 4 temporary base stations. After the raw data set is obtained, free air, latitude, Bouguer and terrain corrections are required for correction of data in gravity measurements. However, this correction was not made because the topographic change was insignificant in the study area. Other corrections were made, and the Bouguer gravity anomaly map of the study area was prepared. Station locations were determined using high precision d-GPS.

Gravity data are reduced to complement the Bouguer anomalies using a reduction density of 2.58 g.cm^{-3}. Figure 5a shows the Bouguer gravity map of the study area obtained by gridding the reduced data. In the Bouguer gravity map, there are high gravity values in the low middle part of the area in the north and south of the area. The height measurements made during the survey were also used for the necessary information to make the altitude correction to the microgravity measurements. The elevation information obtained was mapped and the elevation change in the area

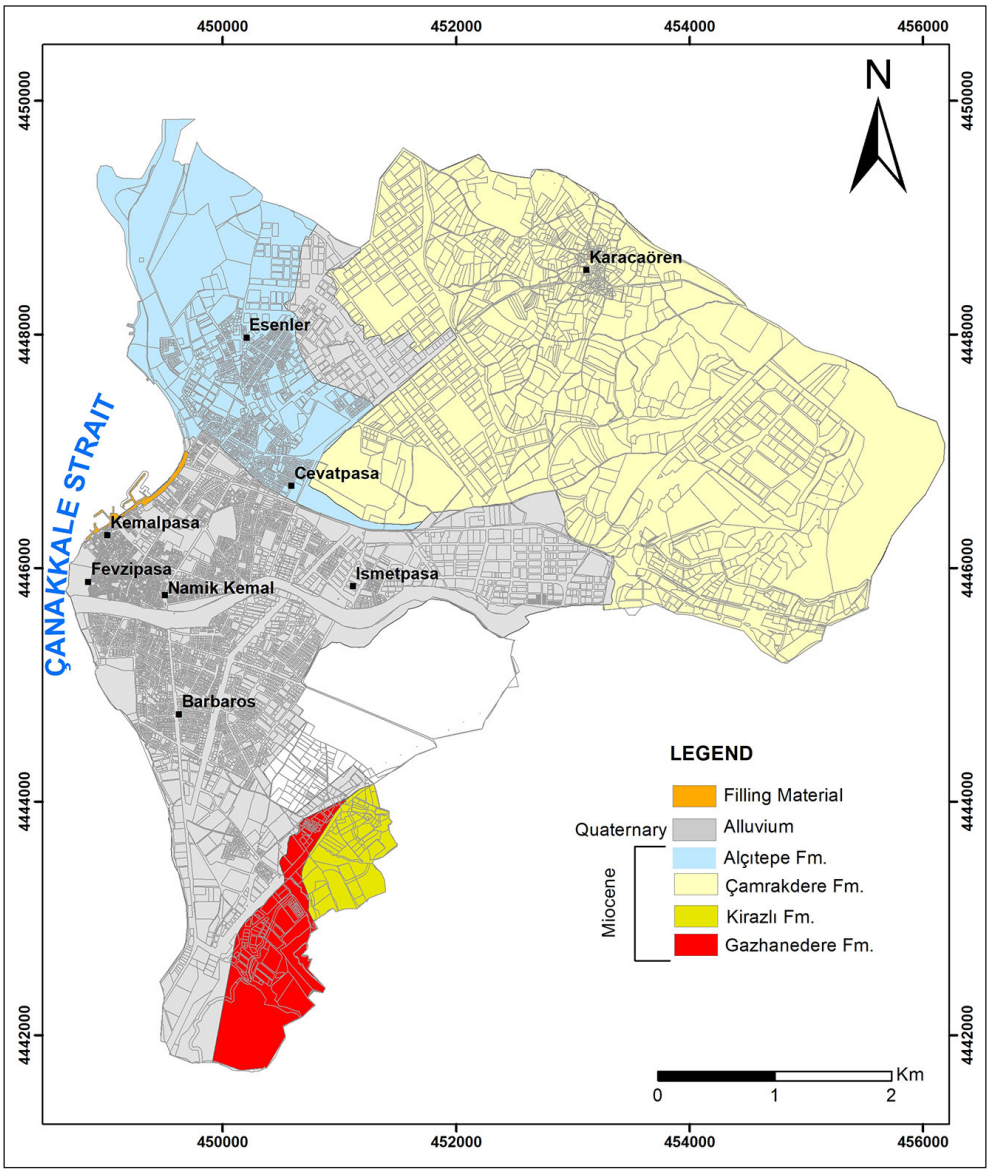

Figure 3. Geological map of the study area (Büyüksaraç *et al.*, 2022).

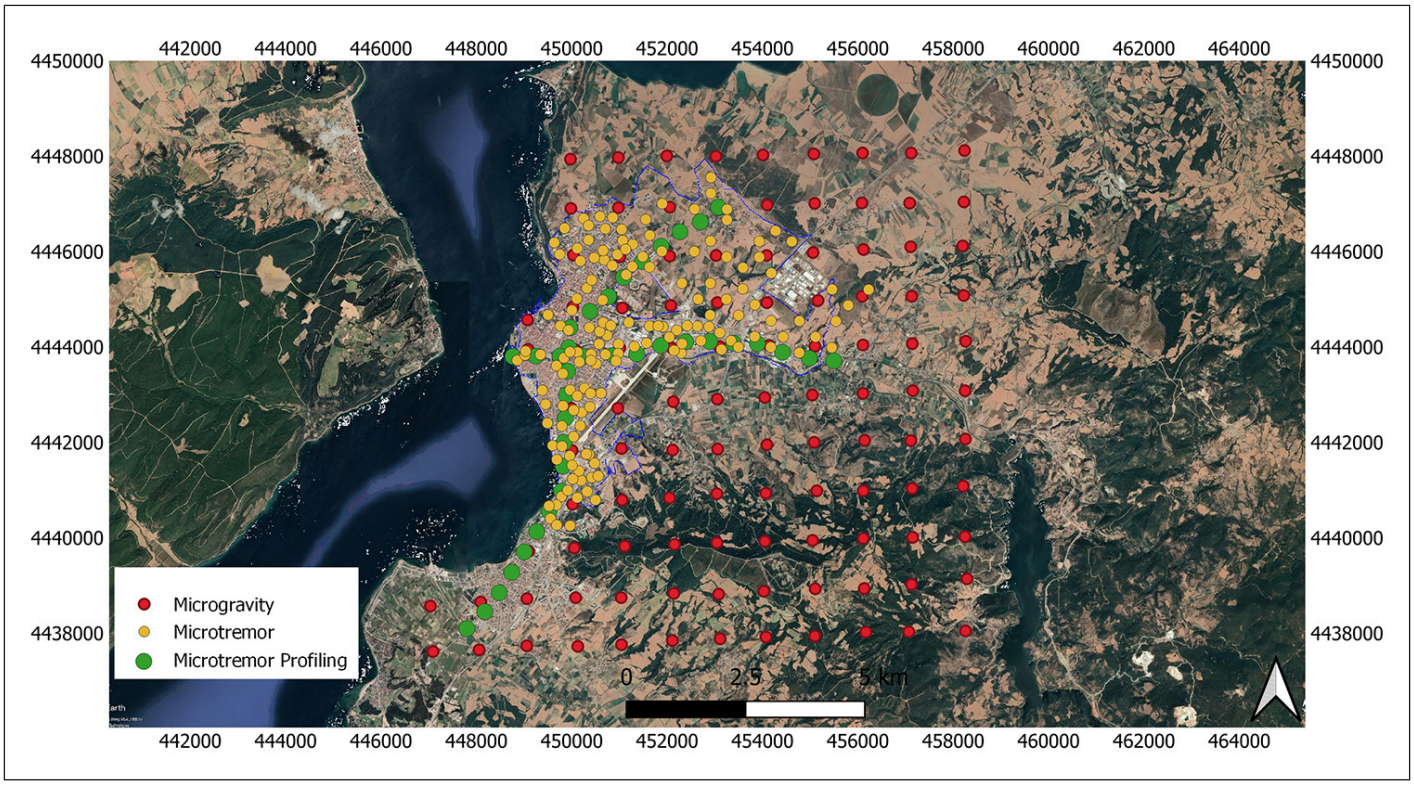

Figure 4. Locations of all geophysical measurement points. *Red circles* show gravity measurement points, *yellow circles* show microtremor points and *green circles* show microtremor profiling taken in the study area.

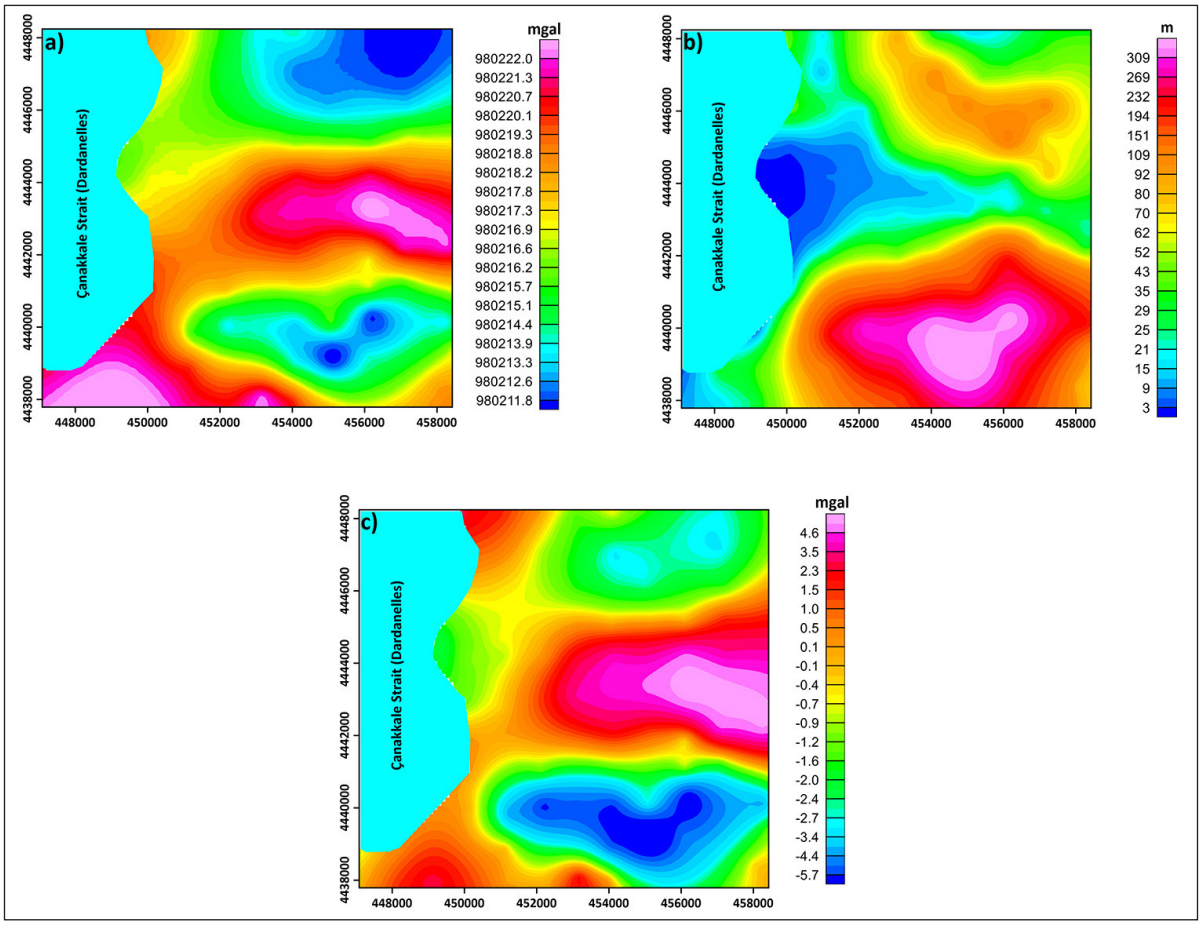

Figure 5 (a). Bouguer gravity anomaly map, (b) Elevation map of the study area, (c) Gravity anomaly map with first order de-trend.

was obtained (Figure 5b). The Ulupınar hill, which has the lowest gravity value (-10 to -13 mGal) in the southeast of the area, stands out most clearly on the map. The height of this place reaches around 430 m. Gravity measurement values include regional values. The regional effect complicates the processing of gravity data by potential field data evaluation methods. Therefore, it is necessary to obtain residual anomaly data by eliminating the regional effect in the data. One of the techniques used in the differentiation of regional-residual anomalies is trend analysis. This analysis can be linear, orthogonal etc. done with polynomials. In this study, residual anomalies were obtained by removing the first-degree trend to the Bouguer Gravity Anomaly. The first-order de-trended gravity anomalies are shown in Figure 5c.

The 3D modelling was applied to the Bouguer anomalies obtained from the microgravity measurements made in the study area. In this method, the gravity anomaly is gridded as a rectangle. Each grid point is the centre of the vertical prismatic structure, and the cross-sectional dimensions of the prisms are equal to the grid intervals. In this way, the data is divided into prisms of equal density as the grid point. The method developed by Cordell and Henderson (1968) was applied to the gravity data shown in Figure 5c to determine the change in young alluvium thickness in the study area. The density difference value was taken as (-0.58 gr.cm-³) (bedrock density= 2.8 gr.cm^{-3} and alluvial density=2.22 gr.cm^{-3}) while making three-dimensional modelling. The thickness of the young alluvial unit in the study area was determined to be approximately 300 m at most as can be seen from the 3D depth model. Prismatic representation of the three-dimensional model is given in Figure 6. In this map, it can be said that the basin depth of the study area is in the range of 160-200 m in the city centre of Çanakkale, the bedrock almost outcrops in the east of Sarıçay and the deepest is observed around 40 m in this part.

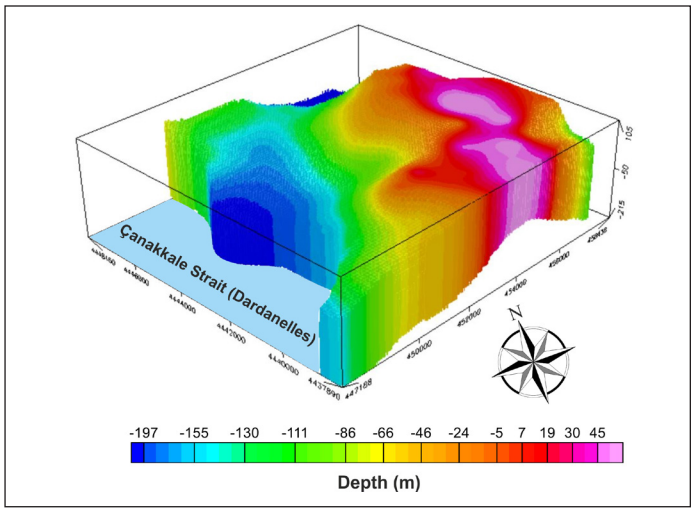

Figure 6. 3D prismatic gravity depth map (After Büyüksaraç *et al.*, 2022)

On the other hand, in the Karacaören Basin in the north of the area, it was observed to be in the range of 200-240 m, with the deepest reaching 240 m.

Inversion of Rayleigh Wave Ellipticity Curve

The local ground response describes the effects on ground motion of shallow sediments, often tens or even hundreds of meters deep, with the slowest seismic velocity. Since soft sediments are limited in size, the affected frequencies are generally higher than 1 Hz. The main factors contributing to the local ground response include impedance effect, non-linear ground content, and potentially resonance effects. Basin effects are related to the deep structure of sediments existing in many areas. Basins generally contain soft sediments near the surface that gradually transition to harder sediments with depth. Topographic effects are related to irregularities in ground surface morphology that can produce local amplification. The frequencies affected by topographic effects depend on the scale of the topographic features.

For example, a local steep hill will affect higher frequencies than large mountains (Stewart *et al.*, 2017).

Shear wave velocity profile and bedrock depth are key parameters for seismic field response estimation. It can be easily determined using geophysical surface wave methods. The surface wave distribution changes along the propagation path depending on the nature of the place where these waves pass. Therefore, surface wave distribution analysis is a good tool to study the most important features of ground structure.

The main advantage of surface wave methods is the ability to characterize the shear wave velocity of the soil on a larger scale. However, in general, the depth of exploration is less than 20 m. A deeper V_s profile is obtained by using the Rayleigh ellipticity curve from active and/or passive measurements. For example, in the Iberian Peninsula, various slip rate models of the crust and upper mantle have been described by Corchete *et al.* (1993, 1995) from the analysis of the Rayleigh wave distribution. This analysis consists of filtering and inversion of the Rayleigh wave distribution to obtain the variation in shear wave velocity versus depth. Sexton *et al.* (1977) showed that the Rayleigh wave ellipticity mainly depends on the local shell structure and does not exhibit azimuth dependence in the range of 10 - 50 seconds.

Therefore, the observed ellipticity for this period range is primarily controlled by the local crustal geology below the seismic station and is not dependent on the propagation path of Rayleigh waves. This essential feature of ellipticity means that ellipticity analysis is a very useful tool for obtaining local crustal models that can be used to identify site and/or local effects in seismic risk and/or seismic design studies (Lee *et al.*, 2003; Rastogi *et al.*, 2011). The ellipticity curve depends on the soil structure and corresponds to the ratio between the

horizontal and vertical components of the ellipse, defined by the particle motion of Rayleigh waves as a function of frequency. The Rayleigh ellipticity curve can be obtained from three-component ambient vibration recordings made at a single station (Gouveia *et al.*, 2016). It is known that the observed ellipticity of a Rayleigh wave can be calculated using the Equation (4) (Aki and Richards, 1980).

$$\varepsilon(T) = A_L(T)/A_Z(T) \quad (4)$$

Here $A_L(T)$ and $A_Z(T)$ are the instrument corrected spectral amplitudes of the longitudinal (also called radial) and vertical seismograms for the period T (Sexton *et al.*, 1977). Rayleigh waves, whose particle motion is in the form of an ellipse and whose motion is opposite to the direction of propagation, propagate in an elastic medium that is semi-infinitely homogeneous. Rayleigh waves are formed by linear interference of P (primary waves) and SV (vertical component of S-wave) waves. In addition, for dispersion to occur in Rayleigh waves, it must propagate in a stratified medium. The phase shift in interference of vertical and horizontal components is $\pm\pi/2$. Depending on whether the phase shift is positive or negative, the particle motion proceeds in the opposite or forward direction. In a homogeneous semi-infinite medium, the particle motion goes backwards at all frequencies and the ellipticity is constant. However, in the case of a stratified environment, the ellipticity is not constant and the particle motion changes from reverse elliptical motion to forward elliptical motion depending on the contrast between bedrock and ground (Konno and Ohmachi, 1998; Ullah, 2017). The ellipticity can be determined by the H/V spectral ratio between the peak at the fundamental dominant frequency and the first minimum at the high frequency (Fäh *et al.*, 2001). Therefore, using the shape of the H/V spectral ratio, the 1-Dimensional S-wave velocity structure of the earth can be revealed. Accurate results have been obtained in areas where the bedrock is both shallow and deep using this method (Fäh *et al.*, 2001; Parolai *et al.*, 2005). The 1-Dimensional seismic velocity structure of the soil affects the propagation of Rayleigh waves and the shape of the H/V spectral ratios obtained with the help of microtremor measurements in the ground (Picotti *et al.*, 2017). Thus, the 1-Dimensional velocity structure of the soil can be obtained by inverting the ellipticity of Rayleigh waves in the fundamental mode (Fäh *et al.*, 2001; Picotti *et al.*, 2017).

The inversion of the ellipticity curves of Rayleigh waves (Figure 7a) is done using Dinver software from the Geopsy package (www.geopsy.org, Wathelet *et al.*, 2020) based on the neighbourhood algorithm (Figure 7b). The parameters that need to be set before inversion are:

- The number of loose layers on the bedrock
- The variation range of their thickness (hmin, hmax)
- Density (min, max)
- Body wave velocity ranges (V_p and V_s)
- Poisson's ratio

The ellipticity curves of Rayleigh waves alone are not sufficient to correlate the depth and velocity values during inversion. Therefore, such an inversion only works in com-

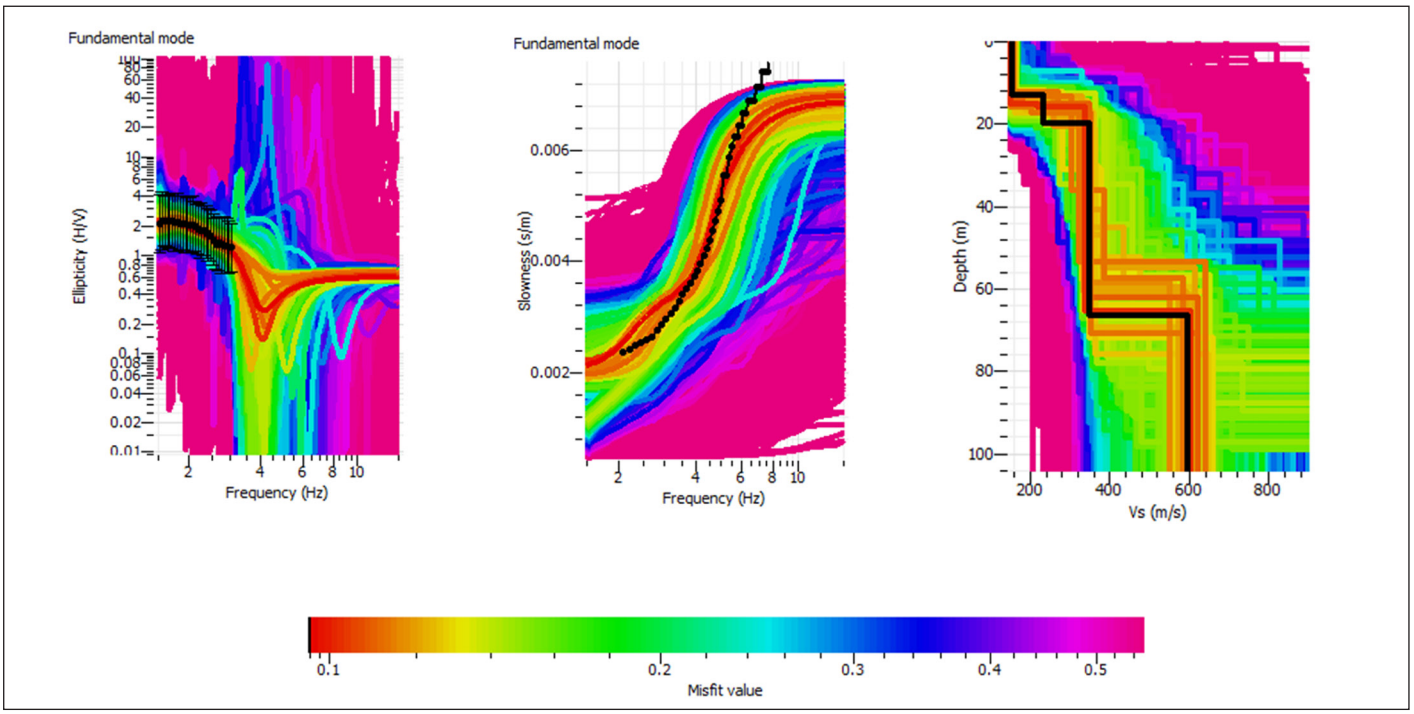

Figure 7 (a). Rayleigh ellipticity graph, (b) Obtaining V_s velocity values, (c) Depth-velocity structure example graph

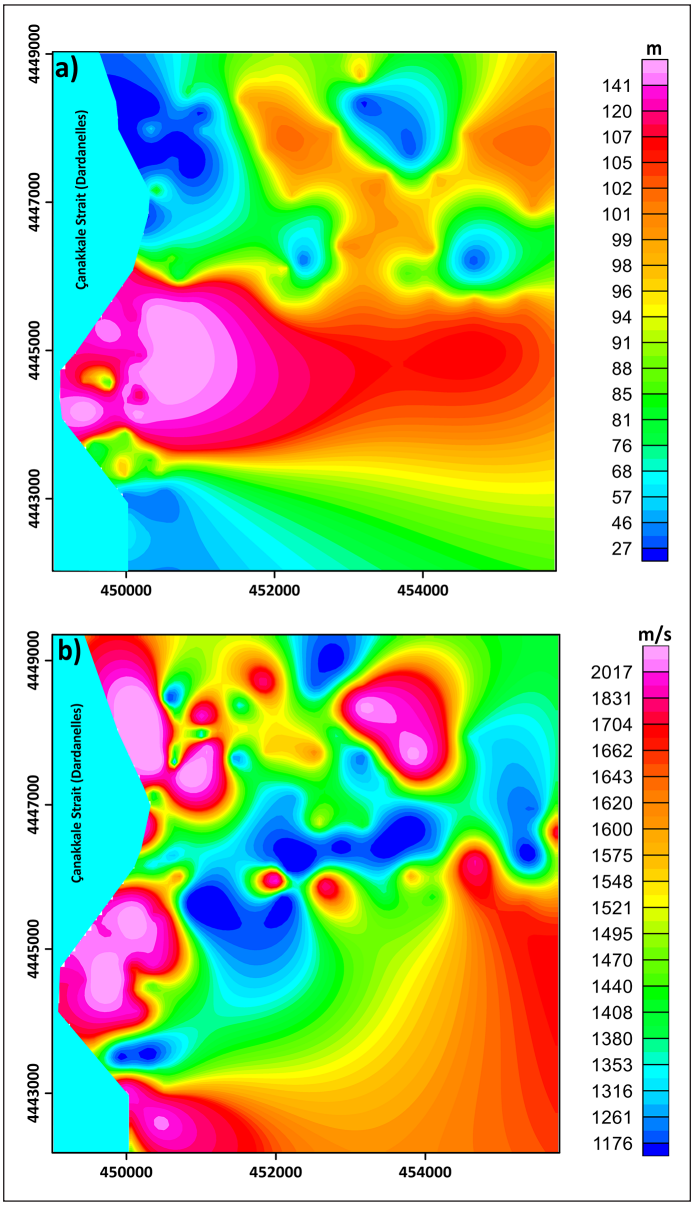

Figure 8 (a). V_s velocity base depth map (includes depth values exceeding 700 m/s velocity value), (b) V_s velocity distribution map under bedrock depth

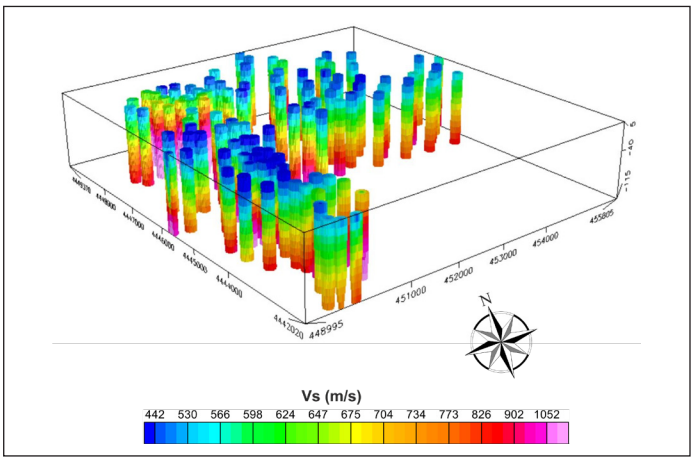

Figure 9. 3D vertical V_s sounding velocity variation map

bination with values obtained from analysis of superficial V_s values such as MASW. Similarly, it is recommended to limit the initial soil model by using previous information (wave velocity, densities, layer thicknesses, etc.) from other geotechnical and geophysical techniques (drilling, seismic fracturing, etc.). The inversion process generates a large number of possible V_s values. For each soil model created, its theoretical curve is calculated and then compared to the experimental one with a false parameter indicating how close the calculated curves are to the experimental ones (Figure 7c).

Rayleigh Ellipticity Calculation and Obtaining S-Wave Velocity

A data set was created by combining microtremor measurements made at 109 points with dispersion curves from which dispersion curves can be obtained, and microtremor measurements made at 37 points within the scope of this project, from the microtremor data collected within the scope of the soil research projects that were made in the study area (Figure 4). Thus, an inverse solution was applied to the generated data via Geopsy software. 1-dimensional V_s velocity and depth values were calculated for the stratified ground structure.

First, a depth map of the study area was created by using V_s values (Figure 8a). This map has been designed as a seismic base map, considering 700 m/s and higher values. The ground structure representing the bedrock or accepted as the seismic basis gives different seismic velocity change values in some parts of the study area. There are very high-speed values as well as limit values. The deepest (below seismic bedrock) V_s seismic velocity distribution map was also created in order to make this distinction (Figure 8b). In addition, a 3-dimensional velocity change map, which can also be defined as V_s sounding, was created by using V_s depth values (Figure 9).

Results and Discussions

Within the scope of this study, which covers the Çanakkale Strait, one of the rare geographies in the world and Turkey's two strait passages, the centre of the city of Çanakkale, which is located on the edge of Çanakkale Strait (Dardanelles), and the nearby towns, a basin depth study based on gravity and microtremor measurements was carried out. Gravity measurements covered a very wide area and depth information about a large part of the Çanakkale Basin could be reached. The entire Bouguer gravity map exhibits anomalies suitable for the geological situation. The region with the lowest negative gravity anomalies (~ -6.0 mGal) is the highest peak in the study area and marine material tempered limestones are dominant. Negative gravity values (~ -2.0 mGal) are also observed in the north-eastern plain uplift. Positive gravity

anomalies were observed on the central quaternary sediments of the study area, as they mostly show marine continental features. The trend removal process was applied to the Bouguer gravity anomalies, and the field was modelled as 3D based on the trend removed gravity anomalies. During the modelling of the gravity anomalies, the density difference between the shallow alluvial units and the volcanic base was considered. Accordingly, modelling was done according to the density difference of -0.58 g/cm^3. It was observed that the alluvial thickness of the area increased especially around Sarıçay, which almost divides the city into two, while the alluvial thickness decreased considerably from Sarıçay to the east. The average thickness of alluvium in the north of the basin is around 20-30 m. Karacaören Plain, located in the northeast of the basin, generally presents a thick alluvial structure and shallows are formed in places. In the central settlement of Çanakkale, the current sediment thickness goes deeper than 100 meters. In the southern parts, the alluvium becomes shallow again. Findings confirming the results obtained from the three-dimensional gravity model were obtained in the 2-dimensional sections created based on the microtremor measurements made in the direction of two separate profiles taken from the south to the north and from the west to the east of the study area. Combined depth sections from both gravity and V_s velocity variations are given in Figures 10a and 10b. Dominant frequency values in these sections were also used as a controller and its compatibility with the behaviour of the basin was observed. In these sections, thicknesses of up to 200 meters can be seen in the parts of Sarıçay close to the Dardanelles. The part of Sarıçay, which is seen as the alluvial fan on the side of the Dardanelles, is the region where alluvium is thickest. On the other hand, the V_s velocity is low due to the shallow groundwater effect in the middle of the basin.

Conclusions

Çanakkale Basin is a Quaternary sedimentary basin dominated by terrestrial and marine alluvial materials. The presence of very loose alluvial materials and shallow groundwater also create important ground problems throughout the basin. The

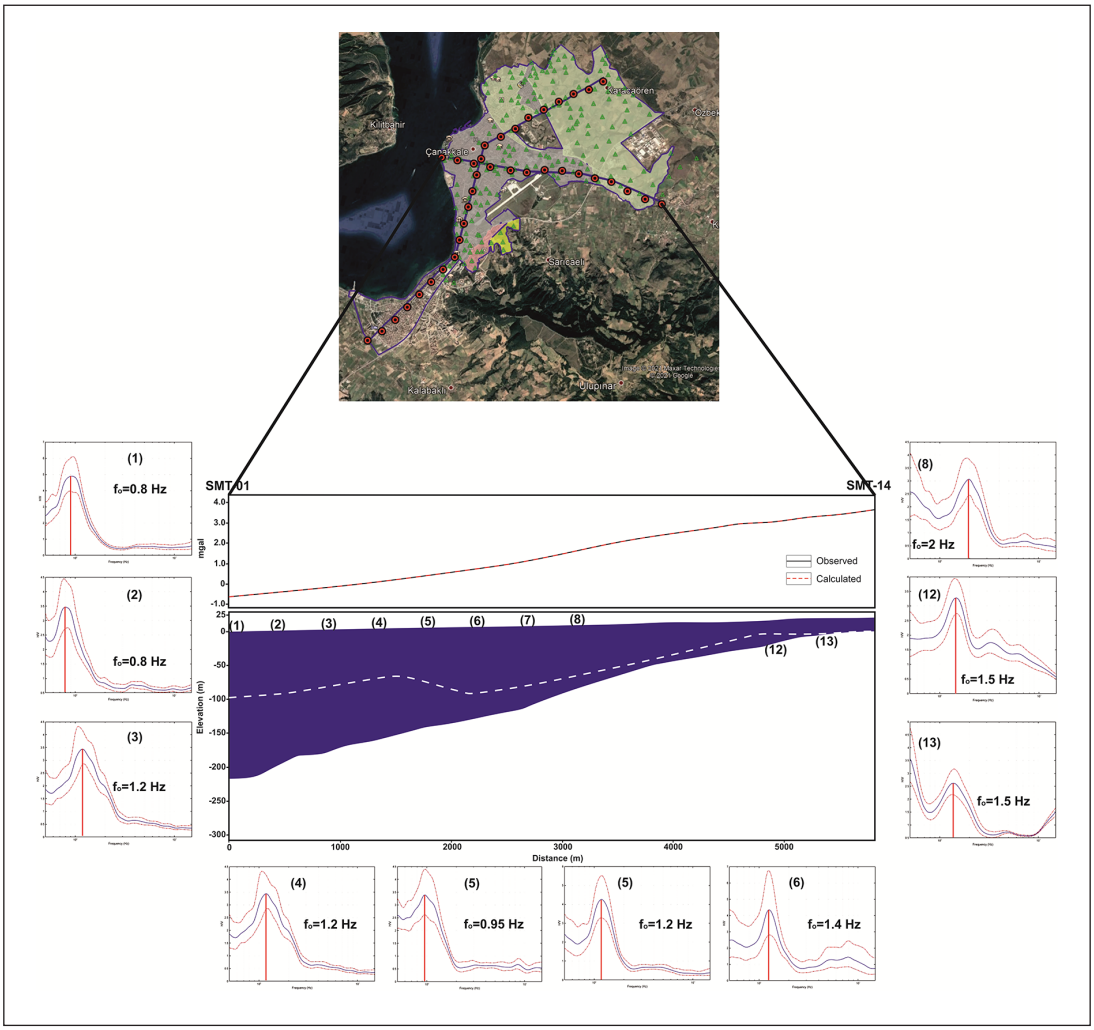

Figure 10 (a). Combined depth section obtained from gravity and V_s-velocity changes along points SMT-01-SMT-14 (White dashed line bedrock boundary obtained from Rayleigh ellipticity measurements ($V_s > 700$ m/s))

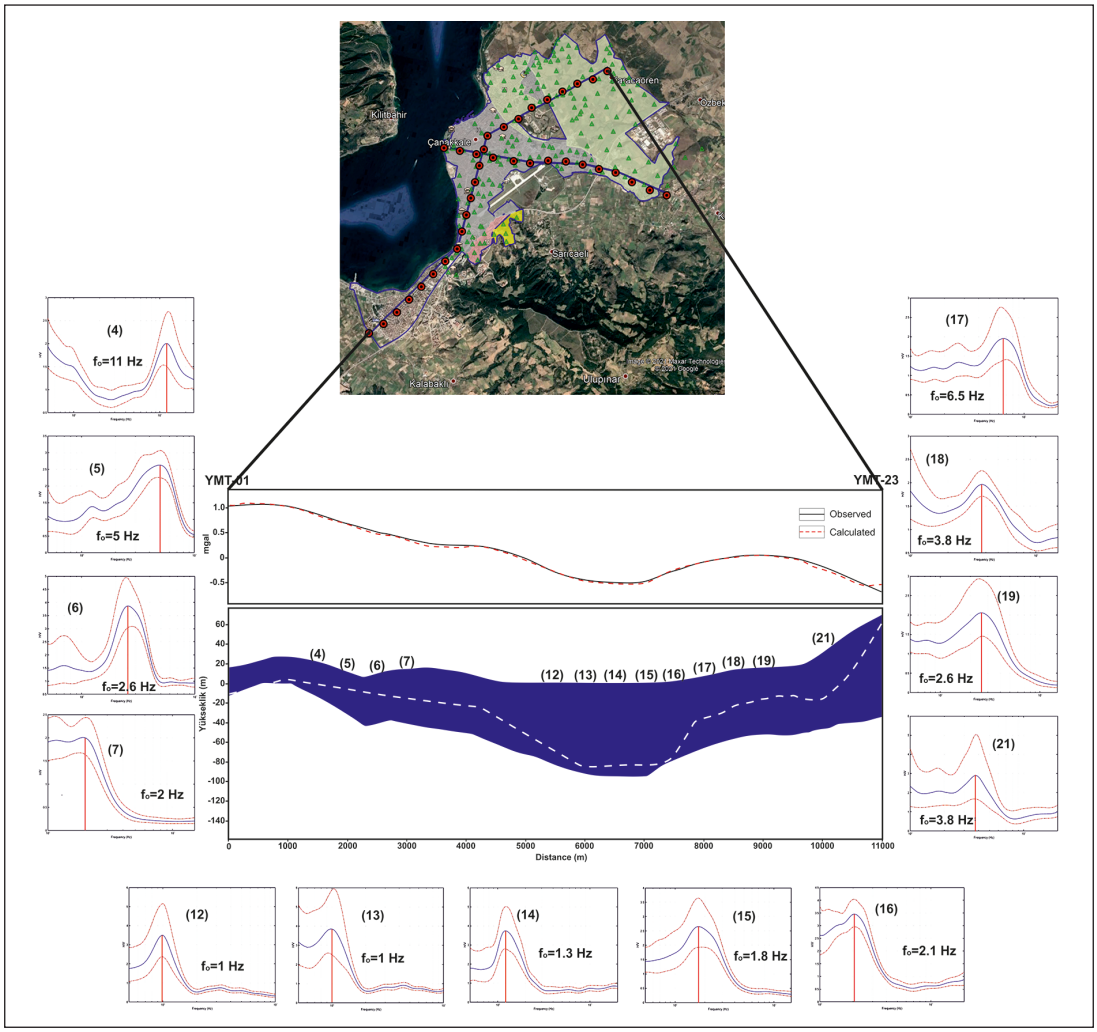

Figure 10 (b). Combined depth section obtained from gravity and velocity variations along points YMT-01-YMT-23 (White dashed line bedrock boundary obtained from Rayleigh ellipticity measurements ($V_s > 700$ m/s))

fact that there is a dense building settlement on the alluvium requires a holistic planning for the Basin. Important findings have been reached with this study. The basement rock depth of the basin was obtained according to the gravity data, and the engineering foundation depth information was created with microtremor measurements. It has been observed that in areas where the local ground response, V_s velocity decreases and frequencies are relatively low (0.8-1.3 Hz), there are areas with loose, soft sediments. Towards the basin edges, in the sections where the bedrock depth decreases, the V_s velocity increases, and the ground frequency values increase considerably (1.5-11.0 Hz). The thickest part of the basin is Ulupınar hill, which is about 300 m deep and is outside the settlement area. The thickness of the basin reaches approximately 200 meters in the alluvial fan, where the settlement is dense, on the edge of the Çanakkale Strait (Dardanelles) and where the Sarıçay River empties into the sea. The southern and eastern parts of the basin are shallow, while the northern and western parts are deeper. V_s velocity values are quite low in the first 10 meters and increase after 10 meters. In the study, the definition of V_s sounding was also made throughout the Basin. With this study, loose basin material thickness and local ground response information, which are the basic information of seismic safe settlement in a basin, were revealed as a whole. Based on this information, the expected acceleration values in the basin, repetitive reflection effects near the basin edge and possible soil amplification effects can be calculated.

Acknowledgements

We are grateful to Editor-in-Chief, Dr. Servando De la Cruz-Reyna and anonymous reviewers for their constructive comments and suggestions. Thanks are due to Scientific Research Projects Coordination Unit of Çanakkale Onsekiz Mart University (Turkey) for supporting this study (Project No: FBA-2020-3307).

References

Akkaya İ., Özvan A., 2019, Site characterization in the Van settlement (Eastern Turkey) using surface waves and HVSR microtremor methods.

Journal of Applied Geophysics.160, 157-170. https://doi.org/10.1016/j.jappgeo.2018.11.009

Aki K. and Richards P. G., 1980, Quantitative seismology: Theory and methods, v.l: W.H. Freeman and Co.

Anbazhagan P., Janarthana Boobalan A., Shaivan H.S., 2019, Establishing empirical correlation between sediment thickness and resonant frequency using HVSR for the Indo-Gangetic Plain. Current Science. 117(9), 1482-1491. https://doi.org/10.18520/cs/v117/i9/1482-1491

Atabey E., Ilgar A. ve Sakıtaş A., 2004, Çanakkale Havzasının Orta – Üst Miosen Stratigrafisi, Çanakkale, KB Türkiye. MTA Dergisi,128: 79-97.

Ateş A., Büyüksaraç A., Bilim F., Bektaş Ö., Şendur Ç., Komanovalı G., 2009, Spatial correlation of the aeromagnetic anomalies and seismogenic faults in the Marmara region, NW Turkey, Tectonophysics, 478 (1-2), 135-142. https://doi.org/10.1016/j.tecto.2008.09.025

Barka A.A., 1997, Neotectonics of the Marmara region in active tectonics of Northwest Anatolia. C. Schindler, M. Pfister (Eds.), The Marmara Poly-project, Hochschulverlag AG an der ETH, Zurich, pp. 55-87.

Bekler T., Demirci A., Ekinci Y.L., Büyüksaraç A., 2019, Analysis of local site conditions through geophysical parameters at a city under earthquake threat: Çanakkale, NW Turkey. J Appl Geophys, 63, 31-39. https://doi.org/10.1016/j.jappgeo.2019.02.009

Birgören G., Özel O., Siyahi B., 2009, Bedrock depth mapping of the coast south of Istanbul: Comparison of analytical and experimental analyses. Turkish J Earth Sci, 18, 315–329. https://doi.org/10.3906/yer-0712-3

Birkle P. ve Satır M., 1995, Dating, Geochemistry and geodynamic significance of the Tertiary magmatism of the Biga Peninsula, NW-Turkey. Geology of the Black Sea Region, Min. Res. Expl. Inst. of Turkey, Ankara, pp. 171-180.

Büyüksaraç A., Bektaş O., Yılmaz H., Arısoy M.O., 2013, Preliminary seismic microzonation of Sivas city Turkey using microtremor and refraction microtremor (ReMi) measurements. J. Seismol. 17, 425–435. https://doi.org/10.1007/s10950-012-9328-1

Büyüksaraç A., Bekler T., Demirci A., Eyisüren O., 2021, New insights into the dynamic characteristics of alluvial media under the earthquake prone area: a case study for the Çanakkale city settlement (NW of Turkey) Arabian Journal of Geosciences, 14:2086 https://doi.org/10.1007/s12517-021-08430-3

Büyüksaraç, A., Karaca, Ö., Eyisüren, O., Bektaş, Ö., Işık, E., 2022, Importance of Bedrock Depth Knowledge in Basins: Çanakkale (Dardanalles) Case History. In: Glavaš, H., Hadzima-Nyarko, M., Karakašić, M., Ademović, N., Avdaković, S. (eds) 30th International Conference on Organization and Technology of Maintenance (OTO 2021). OTO 2021. Lecture Notes in Networks and Systems, vol 369. Springer, Cham. https://doi.org/10.1007/978-3-030-92851-3_25

Corchete V., Badal J., Pujades L. and Canas J. A., 1993, Shear velocity structure beneath the Iberian Massif from broadband Rayleigh wave data. Phys. Earth Planet. Inter., 79, 349-365. https://doi.org/10.1007/s00531-010-0581-7

Corchete V., Badal J., Serón F. J. and Soria A., 1995, Tomographic images of the Iberian subcrustal lithosphere and asthenosphere. Journal of Geophysical Research, 100, 24133-24146. https://doi.org/10.1029/95JB00979

D'Amico V., Picozzi M., Baliva F., Albarello D., 2008, Ambient Noise Measurements for Preliminary Site-Effects Characterization in the Urban Area of Florence, Italy. Bulletin of Seismological Society America, 98 (3), 1373–1388. https://doi.org/10.1785/0120070231

Delgado J., Casado C. L., Estevez A., Giner J., Cuenca A., Molina S., 2000a, Mapping soft soils in the Segura River valley (SE Spain): A case study of microtremors as an exploration tool. Journal of Applied Geophysics, 45, 19–32. https://doi.org/10.1016/S0926-9851(00)00016-1

Del Monaco F., Tallini M., De Rose C., Durante F., 2013, HVNSR survey in historical downtown L'Aquila (central Italy): Site resonance properties vs. subsoil model. Engineering Geology, 158, 34–47. https://doi.org/10.1016/j.enggeo.2013.03.008

Duru M. Pehlivan Ş. Aral İ. O. Şentürk Y. Yavaş F. Kar H., 2012, Biga Yarımadasının Tersiyer Öncesi Jeolojisi, Maden Tetkik ve Arama Genel Müdürlüğü Yayınları, Özel Yayınlar Serisi, No 28: 7-74.

Fah D., Kind F., Giardini D., 2001, A theoretical investigation of average H/V ratios. Geophys J Int, 145, 535–549. https://doi.org/10.1046/j.0956-540x.2001.01406.x

Fairchild G.M., Lane J.W., Voytek E.B., LeBlanc D.R., 2013, Bedrock topography of western Cape Cod, Massachusetts, based on bedrock altitudes from geologic borings and analysis of ambient seismic noise by the horizontal-to-vertical spectral-ratio method, U.S. Geological Survey Scientific Investigations Map 3233, 1 sheet, maps variously scaled, p 17. Pamphlet, on one CD–ROM. http://pubs.usgs.gov/sim/3233. Accessed 20 Feb 2017.

García-Jerez A., Luzón F., Navarro M., Pérez-Ruiz A., 2006, Characterization of the Sedimentary Cover of the Zafarraya Basin, Southern Spain, by Means of Ambient Noise. Bulletine of Seismological Society America, 96(3), 957–967. https://doi.org/10.1785/0120050061

Genç Ş.C. ve Yılmaz Y., 1994, Post Collisional Magmatism in Armutlu Peninsula, NW Anatolia: IAVCEI International Volcanology Congress, Abstracts, Ankara.

Gouveia F., Lopes I., Gomes R.C., 2016, Deeper VS profile from joint analysis of Rayleigh wave data. Engineering Geology, 202, 85–98. https://doi.org/10.1016/j.enggeo.2016.01.006

Harutoonian P., Leo C.J., Tokeshi K., Doanh T., Castellaro S., Zou J.J., 2013, Investigation of dynamically compacted ground by HVSR-based approach. Soil Dynamics and Earthquake Engineering, 46, 20–29. https://doi.org/10.1016/j.soildyn.2012.12.004

Hinzen K.G., Weber B., Scherbaum F., 2004, On the resolution of H/V measurements to determine sediment thickness, a case study across a normal fault in the Lower Rhine Embayment, Germany. Journal of Earthquake Engineering, 8(6), 909-926. https://doi.org/10.1142/S136324690400178X

Ilgar A., Demirci E.S., Duru M., Pehlivan Ş., Dönmez M., Akçay A. E., 2008, 1/100.000 ölçekli Türkiye Jeoloji Haritaları Çanakkale H15 ve H16 Paftaları. No: 100. Maden Tetkik ve Arama Genel Müdürlüğü, Ankara.

Ilgar A., Demirci E.S., Demirci Ö., 2012, Biga Yarımadası Tersiyer istifinin stratigrafisi ve sedimantolojisi. Biga Yarımadası'nın Genel ve Ekonomik Jeolojisi, Editörler: Erdoğan Yüzer, Gürkan Tunay, Maden Tetkik ve Arama Genel Müdürlüğü Özel Yayın Serisi

Kamalian M., Jafari M.K., Ghayamghamian M.R., Shafiee A., Hamzehloo H., Haghshenas E., Sohrabi-bidar A., 2008, Site effect microzonation of Qom, Iran, Engineering Geology, 97 (1–2), 63-79. **https://doi.org/10.1016/j.enggeo.2007.12.006**

Karacık Z., Yılmaz Y., 1998, Geology of the Ignimbrites and the Associated Volcano-plutonic Complex of the Ezine Area, northwestern Anatolia, Journal of Volcanology and Geothermal Research, 85, 251-264. **https://doi.org/10.1016/S0377-0273(98)00058-4**

Kolat Ç., Doyuran V., Ayday C., Süzen M. L., 2006, Preparation of a geotechnical microzonation model using Geographical Information Systems based on Multicriteria Decision Analysis, Engineering Geology, 87(3–4), 241-255. **https://doi.org/10.1016/j.enggeo.2006.07.005**

Konno K., Ohmachi T., 1998, Ground-Motion Characteristics Estimated from Spectral Ratio between Horizontal and Vertical Components of Microtremor. Bull. Seism. Soc. Am., 88, 228-241. **https://doi.org/10.1785/BSSA0880010228**

Kuo C., Chen C., Lin C., Wen K., Huang J., Chang S.J., 2016, S-wave velocity structure and site effect parameters derived from microtremor arrays in the Western Plain of Taiwan. J Asian Earth Sci, 128(1): 27-41. **https://doi.org/10.1016/j.jseaes.2016.07.012**

Kürçer A., Chatzipetros A., Tutkun S.Z., Pavlides S., Ateş Ö., Valkaniotis S., 2008, The Yenice–Gönen active fault (NW Turkey): Active tectonics and palaeoseismology. Tectonophysics, 453(1–4): 263–275. **https://doi.org/10.1016/j.tecto.2007.07.010**

Lee W., Kanamori H., Jennings P. and Kisslinger C., 2003, International Handbook of Earthquake and Engineering Seismology. Elsevier, New York.

Le Pichon X. and Kreemer C., 2010, The Miocene-to-Present Kinematic Evolution of the Eastern Mediterranean and Middle East and Its Implications for Dynamics, Annual Review of Earth and Planetary Sciences 38:1, 323-351. **https://doi.org/10.1146/annurev-earth-040809-152419**

Liang D., Gan F., Zhang W., Jia L., 2018, The application of HVSR method in detecting sediment thickness in karst collapse area of Pearl River Delta, China. Environmental Earth Sciences, 77, 259. **https://doi.org/10.1007/s12665-018-7439-x**

Maghami S., Sohrabi-Bidar A., Bignardi S., Zarean A., Kamalian M., 2021, Extracting the shear wave velocity structure of deep alluviums of "Qom" Basin (Iran) employing HVSR inversion of microtremor recordings. Journal of Applied Geophysics, 104246. **https://doi.org/10.1016/j.jappgeo.2020.104246**

McKenzie D., 1978, Active tectonics of the Alpine-Himalayan Belt: the Aegean Sea and surrounding regions (Tectonics of Aegean Region). Geophysical Journal 55, 217-254. **https://doi.org/10.1111/j.1365-246X.1978.tb04759.x**

Molnar S., Cassidy J.F., Castellaro S., Cornou C., Crow H., Hunter J.A., Matsushima S., Sánchez-Sesma F.J., Yong A., 2018, Application of Microtremor Horizontal-to-Vertical Spectral Ratio (MHVSR) Analysis for Site Characterization: State of the Art. Surveys in Geophysics, 39, 613–631. **https://doi.org/10.1007/s10712-018-9464-4**

Moon S.W., Subramaniam P., Zhang Y., Vinoth G., Ku T., 2019, Bedrock depth evaluation using microtremor measurement: empirical guidelines at weathered granite formation in Singapore. J Appl Geoph, 171: 103866. **https://doi.org/10.1016/j.jappgeo.2019.103866**

Mendecki M.J., Bieta B., Mycka M., 2014, Determination of the resonance frequency – thickness relation based on theambient seismic noise records from Upper Silesia Coal Basin. Contemp. Trends. Geosci.,3, 41-51. **https://doi.org/10.2478/ctg-2014-0021**

Nakamura Y., 2000, Clear identification of fundamental idea of Nakamura's technique and its application", in Proceedings of the XII world conference earthquake engineering. Auckland, New Zeeland, 8 pp.

Över S., Büyüksaraç A., Bektaş O. and Filazi A., 2011, Assessment of potential seismic hazard and site effect in Antakya (Hatay Province), SE Turkey. Environ Earth Sci, 62, 313-326. **https://doi.org/10.1007/s12665-010-0525-3**

Özalaybey S., Zor E., Ergintav S., Tapırdamaz M.C., 2011, Investigation of 3-D basin structures in the Izmit Bay area (Turkey) by single-station microtremor and gravimetric methods. Geophysical Journal International, 186, 883–894. **https://doi.org/10.1111/j.1365-246X.2011.05085.x**

Parolai, S., Picozzi, M., Richwalski, S. M. and Milkereit, C., 2005, Joint inversion of phase velocity dispersionand H/V ratio curves from seismic noise recordings using agenetic algorithm, considering higher modes, Geophys. Res. Lett., 3 2,L01303. **https://doi.org/10.1029/2004GL021115**

Picotti S., Francese R., Giorgi M., Pettenati F. and Carcione J. M., 2017, Estimation of glaciers thicknesses and basal properties using the horizontal-to-vertical component spectral ratio (HVSR) technique from passive seismic data. Journal of Glaciology, 63, 229-248. **https://doi.org/10.1017/jog.2016.135**

Rastogi B.K., Singh A. P., B. Sairam, Jain S. K., Kaneko F., Segawa S. and Matsuo J., 2011, The Possibility of Site Effects: The Anjar Case, Following the Past Earthquakes in the Gujarat, India. Seismological Research Letters, 82(1), 692-701; **https://doi.org/10.1785/** gssrl.82.1.692.

Rupar L., Gosar A., 2020, Mapping the Thickness of Quaternary Sediments in the Iška Alluvial Fan (Central Slovenia) Usıng Microtremor Method. Acta Geodynamica et Geomaterialia, 17(2) (198), 177–190. **https://doi.org/10.13168/AGG.2020.0013**

Sant D.A., Parvez I.A., Rangarajan G., Patel S.J., Bhatt M.N., Salam T.A.S., 2017, Subsurface profiling along Banni Plains and bounding faults, Kachchh, Western India using microtremors method. Journal of Asian Earth Sciences, 146, 326–336. **https://doi.org/10.1016/j.jseaes.2017.06.002**

Sexton J. L., Rudman A. J. and Mead J., 1977, Ellipticity of Rayleigh waves recorded in the Midwest. Bull. Seism. Soc. Am., 67, 369-382. **https://doi.org/10.1785/BSSA0670020369**

Siyako M., Bürkan K.A. ve Okay A.I., 1989, Biga ve Gelibolu yarımadalarının Tersiyer jeolojisi ve hidrokarbon olanakları Türkiye Petrol Jeologları Derneği Bülteni, 1, pp. 183-199, Ankara.

Siyako M., 2006, Trakya Bölgesi Litostratigrafi Birimleri, Stratigrafi Komitesi Litostratigrafi Birimleri Serisi-2. 83 s.

Stewart J.P., Afshari K., Goulet C.A., 2017, Non-Ergodic Site Response in Seismic Hazard Analysis. Earthquake Spectra. 33(4):1385-1414. **https://doi.org/10.1193/081716eqs135m**

Şengör A. M. C., Görür N., Şaroğlu F., 1985, Strikeslip faulting and related basin formation in zones of tectonic escape: Turkey as a case study. (Strike-slip Deformation, Basin Formation, and Sedimentation,

Editörler: Biddle, K.T., ChrisiteBlick, N.). Society of Economic Paleontologists and Mineralogists, Special Publication, 227- 264.

Şentürk K. and Karaköse C., 1987, Çanakkale Boğazı ve dolayının jeolojisi, MTA Genel Müdürlüğü, Jeoloji Etüdleri Dairesi Arşivi, yayınlanmamış teknik rapor, 371, 207 s.

Thabet M., 2019, Site-Specific Relationships between Bedrock Depth and HVSR Fundamental Resonance Frequency Using KiK-NET Data from Japan. Pure Appl Geophys. **https://doi.org/10.1007/s00024-019-02256-7**

Tunusluoğlu M. C. and Karaca Ö., 2018, Liquefaction severity mapping based on SPT data: a case study in Canakkale city (NW Turkey), Environmental Earth Sciences, 77(12). **https://doi.org/10.1007/s12665-018-7597-x**

Ullah I., 2017, Near-surface characterization from the H/V spectral curves along with the joint inversion of the ellipticity and dispersion curves. Doktora Tezi, São Paulo Üniversitesi, Brezilya.

Wathelet M., Chatelain, J. L., Cornou, C., Di Giulio, G., Guillier, B., Ohrnberger, M., Savvaidis, A., 2020, Geopsy: A User-Friendly open-source tool set for ambient vibration processing, Seismological Research Letters, 91(3), 1878-1889.

Yiğitbaş E., 2016, Jeolojik – Antropojenik Sebep – Sonuç İlişkileri Açısından Çanakkale

Geofísica Internacional (2023) **62-1**: 403 - 418

Reconstrucción de Imágenes Sísmicas Virtuales con Técnicas de Interferometría en Datos de Sísmica Pasiva

Solano Bahena René*, Aguirre González Jorge[1], Ávila-Carrera Rafael[2] y Granados Chavarría Iván[3]

Resumen

El objetivo de este trabajo es obtener secciones sísmicas para delimitar estructuras geológicas asociadas a yacimientos de hidrocarburos. Utilizamos datos de sísmica pasiva de un arreglo rectangular localizado al noreste de la República Mexicana y el método de Interferometría Sísmica (*IS*), el cual permite extraer la función de Green mediante el uso de correlaciones cruzadas (*CC(t)*) de trazas de ruido sísmico.

Procesamos 6 líneas de 8 km de longitud aproximadamente, con 159 geófonos cada una. Las *CC(t)* obtenidas (también llamadas pseudo-secciones sísmicas de tiros virtuales) fueron procesadas para la extracción de información estructural y de velocidad subsuperficial, con los algoritmos que usualmente son utilizados en la industria de la sismología de exploración. Los resultados los reagrupamos en grupos de offset común (Common Offset Gathers, por sus siglas en ingles *COG*), para generar imágenes del campo de velocidades en el subsuelo en términos de secciones sísmicas de offset cero.

Realizamos un procesamiento que consistió en aplicar el método de la transformada de ondícula, para descomponer y reconstruir las *CC(t)* a partir de la ondícula de Meyer, mejorando la calidad de las *CC(t)*. Posteriormente, generamos nuevas pseudo-secciones sísmicas considerando un offset en común y varias longitudes entre fuente-receptor. En este caso los resultados mejoraron substancialmente, mostrando los reflectores esperados. Observamos que, con un offset mayor, la profundidad de investigación aumentaba, aunque la resolución superficial disminuía. Finalmente, las secciones obtenidas fueron comparadas con una sección sísmica convencional (también llamadas secciones de sísmica "activa") migrada en profundidad.

Palabras clave: Sísmica pasiva, interferometría sísmica, Función de Green, Pseudo-secciones sísmicas de tiros virtuales, Transformada de ondícula.

Abstract

This paper aims to obtain compressional body waves (seismic sections) to delimit geological structures associated with hydrocarbon reservoirs. We used a passive seismic dataset from a rectangular array located at northeast of Mexico. Seismic Interferometry (*IS*) method, which allows extracting the Green's function by using cross-correlations (*CC(t)*) of seismic traces was applied.

We processed six lines of approximately 8 km length, with 159 geophones each. The obtained *CC(t)* (also called virtual shots pseudo-sections) were processed with the algorithms that generally are used in the seismic exploration industry to extract the structural and sub-surface velocity information. We regrouped the results of the pseudo-sections of virtual shots by common offset gathers (*COG*) to generate subsurface images in terms of a zero-offset seismic section.

Although, alternative processing algorithms were performed, which consists in applying the wavelet transform method to decompose and reconstruct the *CC(t)* by means of the Meyer wavelet, improving the quality of the *CC(t)*. Subsequently, new seismic sections were generated considering a common offset. We use offsets of 100, 500, 900, 1300, 1700, and 2100 m among source-receiver virtual arrays. In this case, results were improved substantially, clearly showing the expected reflectors. We observed that the depth of investigation increases for higher offsets, meanwhile the surface resolution decreases. The sections were stacked with the different offsets mentioned above for each line, resulting in a total common offset section. Finally, the obtained sections were compared *versus* a conventional seismic section (also called "active" seismic sections) migrated in depth.

Keywords: Passive seismic, seismic interferometry, Green's function, Pseudo-sections of virtual shots, Wavelet transform.

Received: March 22, 2022; November 9, 2022; published on-line: January 1, 2023.

Editorial responsibility: Oscar Cerapio Valdiviezo Mijangos

* Corresponding author: Solano Bahena René, resolanoba@gmail.com. Instituto Mexicano del Petróleo, Eje Central Lázaro Cárdenas #152, San Bartolo Atepehuacan, Ciudad de México.

[1] Instituto de Ingeniería, UNAM Circuito Escolar s/n. Ciudad Universitaria, Coyoacán, Ciudad de México. joagg@pumas.iingen.unam.mx

[2] Instituto Mexicano del Petróleo, Eje Central Lázaro Cárdenas #152, San Bartolo Atepehuacan, Ciudad de México. rcarrer@imp.mx

[3] Instituto de Geofísica, UNAM, Circuito de la investigación Científica s/n, Ciudad Universitaria, Coyoacán, Ciudad de México. igranadosc@igeofisica.unam.mx

https://doi.org/10.22201/igeof.2954436xe.2023.62.1.1448

Introducción

Los métodos geofísicos, y en particular, la prospección sísmica, son herramientas que ayudan en la exploración y caracterización de yacimientos de hidrocarburos. Sin embargo, en los últimos 15 años se han desarrollado estudios geofísicos utilizando ruido sísmico como una alternativa más económica, rápida y amigable con el ambiente, en comparación con los sendos estudios de sísmica de reflexión.

En el presente artículo se usaron trazas de ruido sísmico, con el fin de obtener imágenes del subsuelo de manera aproximada, rápida, barata y confiable, que permitan identificar y delimitar estructuras geológicas relacionadas con yacimientos de hidrocarburos. Utilizamos el método de Interferometría Sísmica (*IS*), que consiste en la recuperación de la función de Green entre dos receptores mediante las correlaciones cruzadas de trazas de ruido sísmico, que considera a uno de ellos como una fuente virtual. A nivel regional, para distancias entre 100 a 2000 km, aproximadamente, la *IS* se aplica a grabaciones de ruido sísmico en la banda de frecuencia de 0.1-0.4 Hz (*Shapiro y Campillo, 2004; Sabra et al., 2005*).

Claerbout (1968), mostró que la respuesta de reflexión de un medio con capas horizontales puede ser sintetizada a partir de la autocorrelación de su respuesta de transmisión. Esta relación física entre la respuesta de reflexión y la de transmisión se derivó de un teorema de reciprocidad de tipo correlacional (Wapenaar, 2004), es decir una ecuación integral compuesta por funciones de Green tanto causales como anticausales que establece una forma para reconstruir la reflectividad del medio. Por otro lado, *Gouédard et al. (2008)*, describe aplicaciones exitosas de la interferometría en diferentes escalas, desde la extracción de datos de reflexión en mediciones de laboratorio hasta la construcción de ondas superficiales a escala regional.

Algunos autores como *Nakata et al. (2011) y Xu et al. (2012)*, han utilizado la *IS* para la exploración sísmica. *Draganov et al. (2007)*, recuperaron las llegadas de reflexión entre 2 y 10 Hz. *Draganov et al. (2009)*, mostraron resultados preliminares de la recuperación de llegadas de reflexión entre 6 y 24 Hz utilizando ventajosamente patrones de geófonos que suprimieron las ondas superficiales dominantes por encima de los 5 Hz en campo. *Draganov et al. (2013)*, hicieron estudios basándose en las *CC(t)* de ruido sísmico para obtener información estructural del subsuelo.

En la práctica, la recuperación de las ondas de cuerpo resulta más difícil que las ondas superficiales ya que, estas últimas predominan debido básicamente a dos factores: que las fuentes ocurren en superficie y que el decaimiento de la amplitud con la distancia es mayor en las ondas de cuerpo. Aunado a que, en la mayoría de los casos, la aplicación de la *IS* se ve limitada por la falta de receptores en profundidad en la sísmica de exploración.

En esta investigación presentamos una aplicación general de los trabajos de exploración que se realizaron para usar la *IS* considerando escalas sísmicas, con distancias entre receptores de 50 m en dirección *inline* y 200 m en dirección crossline, con una profundidad de propagación de las ondas símicas de 2000 m. Trabajaremos bajo la hipótesis de que el ruido sísmico tendrá llegadas de ondas de cuerpo, necesarias para la recuperación de reflexiones sísmicas. Nos apoyaremos en algunas herramientas como la transformada de ondícula y la metodología que propone *Yilmaz (2001)* para el procesamiento de datos de exploración sísmica.

Método

La función de Green representa el movimiento sísmico producido en una cierta dirección en un sitio x, debido a la aplicación de una fuerza unitaria en otro sito ξ, y contiene información del medio por dónde las ondas sísmicas se propagan. Dicho de otra manera, es la respuesta sísmica en un punto de observación ante una fuerza súbita aplicada en algún sitio del medio elástico.

Claerbout (1968) demostró que la *CC(t)* de trazas de ruido sísmico de un campo de ondas difusas, registradas en dos diferentes receptores que se encuentran en medios tridimensionales y heterogéneos, llevan a la construcción de la función de Green que se observaría si hubiera una fuente impulsiva en uno de los dos receptores, con respecto al otro. En este artículo partiremos del método de Interferometría Sísmica (*IS*) y posteriormente, explicaremos cómo aplicamos los métodos comunes de la sísmica de exploración a los resultados que obtuvimos con la sísmica pasiva.

Interferometría Sísmica

La operación matemática principal utilizada en procesamiento digital para estudiar cuan parecidas son dos señales es la correlación cruzada (*CC(t)*). Por lo tanto, el término de Interferometría Sísmica se refiere al principio de generar nuevas respuestas sísmicas mediante las *CC(t)*, a partir de las observaciones sísmicas en diferentes lugares de los receptores (*Wapenaar y Fokkeman, 2006*).

Como mencionamos, la *IS* es un método que permite extraer o recuperar la función de Green entre dos receptores que grabaron ruido sísmico, considerando a uno de ellos como si fuera una fuente virtual. La *CC(t)* entre pares de trazas sísmicas y la suma o apilamiento de estas, es el procesamiento básico de la Interferometría Sísmica *(Bensen et al., 2007; Gouédard et al., 2008)*. El apilamiento se lleva a cabo para incrementar la relación señal-ruido, lo que resulta conveniente para trazas muy ruidosas.

Sin embargo, aunque las correlaciones de ruido se han utilizado con éxito en estudios tomográficos de sismología *(Shapiro et al., 2005)* y para controlar los cambios de veloci-

dad *(Duputel et al., 2009; Brenguier et al., 2011)*, queda claro que la construcción de la función de Green no es perfecta, incluso cuando se correlacionan varios años de ruido. Según *Sthely et al. (2008)* hay dos razones que explican lo anterior: 1) La distribución de las fuentes de ruido no es homogénea, lo que implica que las correlaciones convergen a una función R, diferente de la función de Green real. 2) Debido a que se usan registros de ruido de longitud finita, la convergencia de las correlaciones hacia la función R no es completa, y las fluctuaciones permanecen en las correlaciones.

Para explicar el método de *IS* consideraremos el caso unidimensional y homogéneo y seguiremos el desarrollo de *Wapenaar et al. (2010),* donde tenemos dos puntos X_A y X_B que representan estaciones sísmicas. Si el medio es afectado por una señal que se comporta de manera impulsiva X_S obtendremos una fuente viajando a lo largo del eje X (Figura 1). La estación A registrará el impulso a un tiempo $t_A = (X_A - X_S)/c$ y la estación B en un tiempo $t_B = (X_B - X_S)/c$ mayor al de la estación A (donde c es la velocidad de propagación).

$$G(X_A, X_S, t)=\delta(t-t_A) \quad (1)$$

$$G(X_B, X_S, t)=\delta(t-t_B) \quad (2)$$

Las ecuaciones 1 y 2, muestran las respuestas de las correlaciones cruzadas entre las señales recibidas en A y B. Observamos que hay una distancia en común de X_S a X_A, donde el tiempo de viaje a lo largo de esa distancia en común se cancela al realizar la $CC(t)$ dejando sólo los tiempos de viaje a lo largo de la distancia entre X_A y X_B. Por lo tanto, percibimos un impulso en X_B como si la fuente estuviera en X_A. La ecuación 3 representa a la Función de Green de las ondas que se propagan entre los puntos X_A a X_B considerando una fuente X_S.

$$G(X_B, X_A, t)=G(X_B, X_S, t)*G(X_A, X_S, t) \quad (3)$$

Datos y equipo utilizado

El campo de velocidades de las trazas de sísmica pasiva utilizadas fueron grabadas con geofónos acelerómetros triaxiales de la marca Sercel DSU3-428XL. La adquisición de los datos fue coordinada por el Instituto Mexicano del Petróleo (IMP). El área de estudio comprende un arreglo que consta de 100 km^2, dividido en 6 bloques rectangulares, que en conjunto completan un tendido total de 27758 receptores (4293×6).

Para este trabajo se procesaron 6 líneas ubicadas dentro del bloque 4, integrado por 4293 receptores ordenados en 27 líneas de 159 geófonos, aproximadamente (Figura 2). Las trazas de ruido sísmico se grabaron a 500 muestras por segundo (m.p.s.) contando con 6.5 h de grabación, aproximadamente. Se utilizó la componente vertical para la realización de las $CC(t)$.

Estimación de las Funciones de Green

Las funciones de Green fueron estimadas mediante las correlaciones cruzadas de pares de receptores. Se aplicó un procesamiento previo con el objetivo de mejorar la relación señal-ruido. *Bensen et al. (2007),* mencionan cuatro fases importantes para el procesamiento de datos de ruido sísmico cuando se estudian ondas superficiales: 1) Preparación de

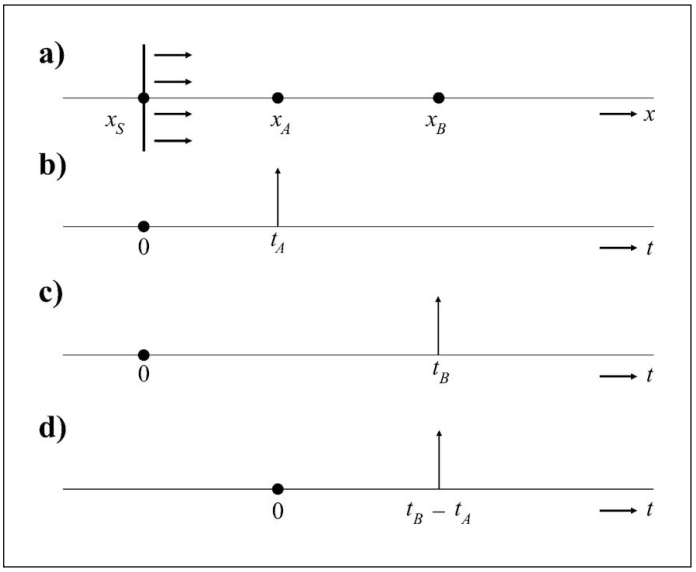

Figura 1. Interferometría de onda directa, Wapenaar *et al.*, (2010).

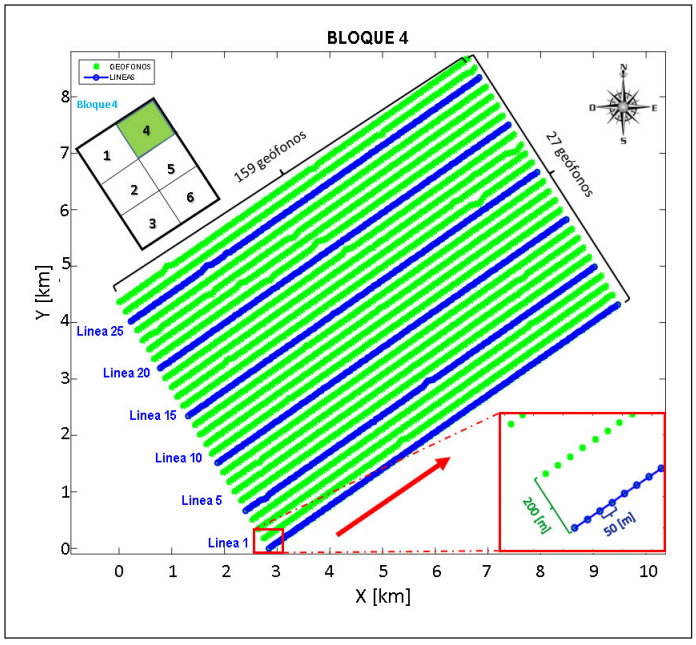

Figura 2. Bloque 4. Separación de receptores en dirección *inline* 50 m y 200 m en dirección crossline. En color azul se muestran las 6 líneas procesadas para este estudio: Línea 1 (L1), Línea 5 (L5), Línea 10 (L10), Línea 15 (L15), Línea 20 (L20) y Línea 25 (L25).

los datos por estación. 2) Correlación cruzada y apilamiento temporal. 3) Medición de curvas de dispersión (realizadas con análisis de frecuencia-tiempo para velocidades de grupo y fase). 4) Control de calidad, análisis de errores y selección de las mediciones aceptables.

Acondicionamiento de trazas

En la primera fase del procesamiento se removió la media y la línea de tendencia en cada una de las trazas de ruido sísmico. Posteriormente, se definió la secuencia de procesamiento idónea para incrementar la relación señal-ruido de cada una de ellas (diagrama de la Figura 3). Debido a que el principal objetivo de este trabajo está enfocado en generar buenas imágenes sísmicas producidas por reflexiones provenientes del ruido, estamos interesados en extraer las ondas de cuerpo a partir de las *CC(t)*. Para ello, se tomó sólo la componente vertical de las trazas de ruido, ya que de acuerdo con *Toksöz y Lacoss, (1968); Douze, (1967); Okada, (2003); Bonnefoy-Claudet et al., (2006),* las componentes horizontales son dominadas por las ondas superficiales.

A diferencia de *Bensen et al. (2007),* aplicamos primero el blanqueamiento espectral para ampliar la banda de la señal y suavizar el espectro de amplitud de Fourier, evitando que las señales con gran amplitud enmascaren la información de señales con menor amplitud. Posteriormente, aplicamos un filtro Butterworth de 1 a 30 Hz para delimitar el rango de las frecuencias de interés asociadas a reflexiones sísmicas. Por último, se aplicó la normalización temporal que tiene como objetivo evitar señales dominantes de gran amplitud (*p. ej.* terremotos, irregularidades instrumentales y ruido no estacionario de fuentes cercanas).

Siguiendo el diagrama de la Figura 3, el siguiente paso

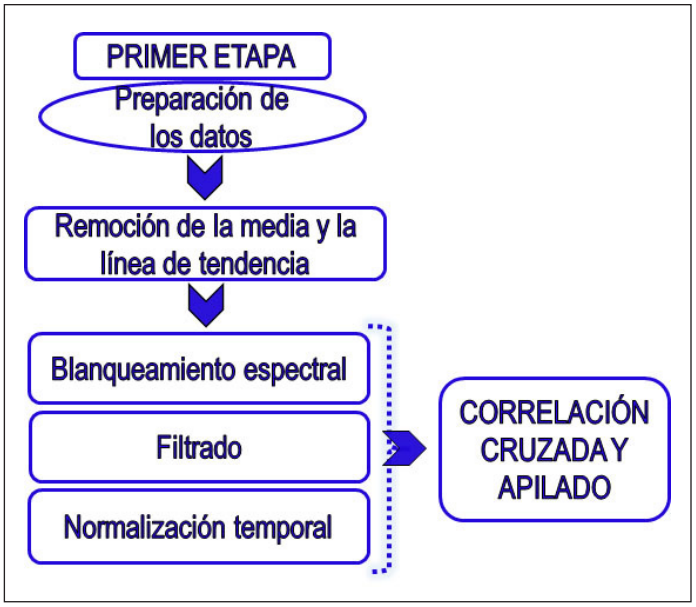

Figura 3. Secuencia de pre-procesamiento para las trazas de ruido sísmico.

fue realizar las *CC(t)*. Si la distribución de fuentes de ruido es homogénea, la parte causal y anticausal de las *CC(t)* serán simétricas en amplitud y tiempos de llegada *(Wapenaar et al., 2010)*. Sin embargo, cuando no se cumple esto, obtendremos correlaciones asimétricas.

Las *CC(t)* las realizamos con ventanas de tiempo de 30 s. Posteriormente, las apilamos dando como resultado la suma de 780 ventanas para cada par de geófonos (6.5 h de grabación). El apilado de un gran número de ventanas de tiempo nos ayuda a promediar las variaciones de las correlaciones, permitiendo aumentar la señal coherente y considerar una distribución de ruido más isótropa, dando como resultado una mejor estimación de la función de Green.

En la Figura 4, mostramos un ejemplo de las variaciones de las *CC(t)* en la línea 15 (L15, cuya distancia entre pares de receptores es de 50 m) cuando el número de ventanas apiladas aumenta. El número de ventanas de apilamiento entre el par de geófonos 106-96 fue de: a) 6 ventanas de 30 s; b) 60 ventanas de 30 s y c) 360 ventanas de 30 s. Las *CC(t)* fueron normalizadas por su máximo valor absoluto. Observamos que la correlación mejora cuando el número de ventanas apiladas aumenta.

Pseudo-secciones sísmicas de tiros virtuales

En el apartado anterior se comentó acerca de la asimetría de las correlaciones y del efecto que provocan las diferentes distribuciones de fuentes de ruido sísmico. Lo anterior, hace que no se cumplan estrictamente las características de un campo difuso, provocando que no se pueda obtener la función de Green completa del medio entre los dos receptores a partir de la correlación.

Sin embargo, algunos autores como *Lobkis y Weaver (2001)*, y *Roux et al. (2005)*, obtuvieron resultados teóricos bajo el supuesto de que se tiene una distribución de fuentes homogéneas. La relación entre la correlación cruzada de ruido sísmico *CC(t)* y la función de Green estimada G(t) entre los receptores A y B se puede expresar como:

$$\frac{dCC_{AB}(t)}{dt} = -G_{AB}(t) + G_{BA}(-t); -\infty \le t < \infty \tag{4}$$

Siguiendo lo que describe *Lin et al. (2008)*, la ecuación anterior es equivalente a:

$$G_{AB}(t) = -\frac{dCC_{AB}(t)}{dt}; 0 \le t < \infty \tag{5}$$

$$G_{BA}(t) = -\frac{dCC_{AB}(-t)}{dt}; 0 \le t < \infty \tag{6}$$

Considerando el teorema de reciprocidad de las funciones de Green ($G_{AB}(t) = G_{BA}(t)$), nosotros promediamos las señales

de la parte causal y anticausal para obtener una correlación simétrica. Posteriormente, usamos esta señal simétrica para obtener la función de Green final del medio mostrada en la ecuación:

$$G_{AB}(t) = -\frac{d}{dt}\left[\frac{CC_{AB}(t) + CC_{AB}(-t)}{2}\right] \quad (7)$$

Las *CC(t)* se obtuvieron para las líneas marcadas en color azul en la Figura 2, consideramos cada uno de los 159 geófonos en dirección *inline* como fuentes virtuales (*FV*) y a su vez como receptores. Las *CC(t)* fueron estimadas para cada par de geófonos con el resto de ellos, en cada una de las líneas. El resultado es una sección sísmica de tiros virtuales, a la que llamaremos: *"pseudo-sección sísmica de tiros virtuales"*.

Yilmaz (1987) menciona que la energía de reflexión sísmica utilizable se limita a un ancho de banda de aproximadamente 10 a 70 Hz. Debido a esto, y con la finalidad de eliminar las ondas superficiales, decidimos realizar un segundo filtrado posterior al apilado de las *CC(t)* en un rango de 10 a 30 Hz.

A continuación, en la parte superior de la Figura 5, se observan las ubicaciones de las *FV* a lo largo de las líneas 10 y 15 (L10 y L15) del bloque 4. Recordando que cada geófono fue considerado como fuente virtual y receptor, en la Figura 5 se observan algunos resultados de las *pseudo-secciones sísmicas de tiros virtuales*, para: Línea 10 con el geófono 66 (G66) y la Línea 15, siendo la *FV* el geófono 75 (G75), respectivamente.

En color amarillo se resaltan las posibles reflexiones cercanas a la fuente virtual. Para los ejemplos de la L10 y L15, las posibles reflexiones llegan a 0.8 s y 0.9 s, respectivamente (Figura 5b). En la parte inferior (Figura 5c), se observan resultados análogos pero una vez aplicado el segundo filtrado a las pseudo-secciones. Hay una mejora significativa, ya que las reflexiones cercanas a la fuente (color amarillo) se definen mejor, e incluso se ven algunos horizontes con mayor continuidad (recuadros azules). Aunque las *CC(t)* y el apilado se realizaron para todas las combinaciones entre pares de los 159 geófonos en cada línea, sólo mostramos algunos ejemplos para visualizar los resultados obtenidos.

Pre-procesamiento de las pseudo-secciones sísmicas de tiros virtuales

Las reflexiones en datos sísmicos de exploración se reconocen por tiempos de viaje hiperbólicos. El principal objetivo del procesamiento en la exploración sísmica es mejorar la reflexión genuina al suprimir la energía no deseada (*Yilmaz, 1987*). Después de haber utilizado el método de *IS* y bajo la

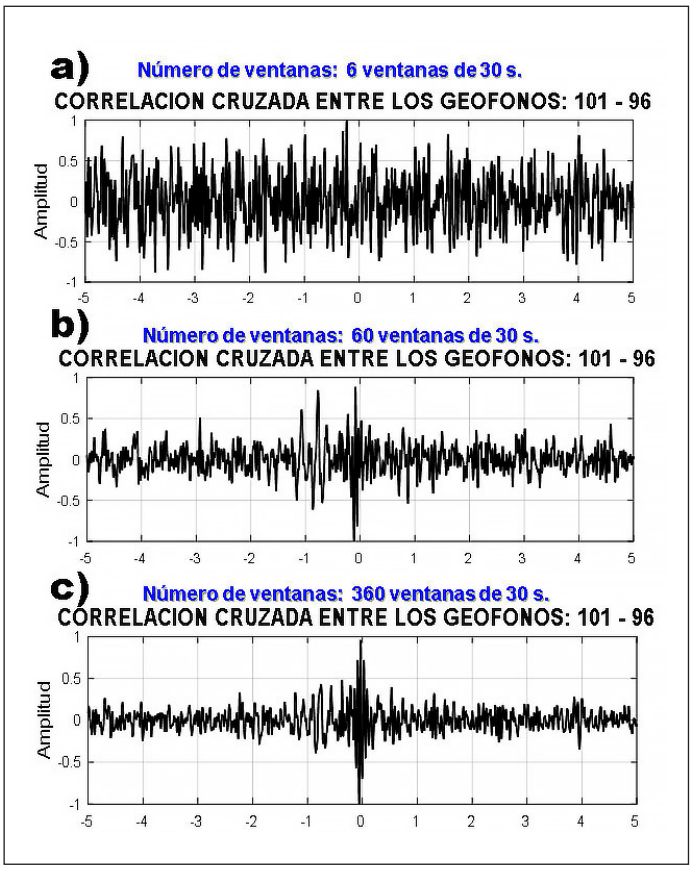

Figura 4. Correlación cruzada (*CC(t)*) entre los geófonos 101-96 de la línea 15 (L15). Ventanas apiladas de 30 s. Número de ventanas: a) 6; b) 60 y c) 360.

hipótesis de que el ruido sísmico contiene ondas de cuerpo, se aplicaron algoritmos de procesamiento que usualmente son utilizados en la industria de la sísmica de exploración.

En general, los objetivos principales del procesamiento en datos sísmicos de reflexión, son mejorar la resolución sísmica y aumentar la relación señal-ruido (SNR por sus siglas en ingles). Estos objetivos se logran a través de tres etapas principales: deconvolución, apilamiento y migración.

Con la finalidad de generar imágenes del subsuelo en términos de una sección sísmica de offset cero, las *pseudo-secciones sísmicas de tiros virtuales* fueron agrupadas en conjuntos de offset común, con lo cual, los diferentes reflectores representaran los cambios de impedancia acústica del medio.

Reflector común

En este apartado se propone una alternativa al procesamiento que se realiza en la sísmica de reflexión, reagrupamos los datos en conjuntos de offset común (*COG*) y los pasos realizados para aplicar esta metodología, fueron: 1) Considerar que todos nuestros geófonos son fuentes y receptores; 2) Aplicar el blanqueamiento espectral, filtrado de 1-30 Hz y su

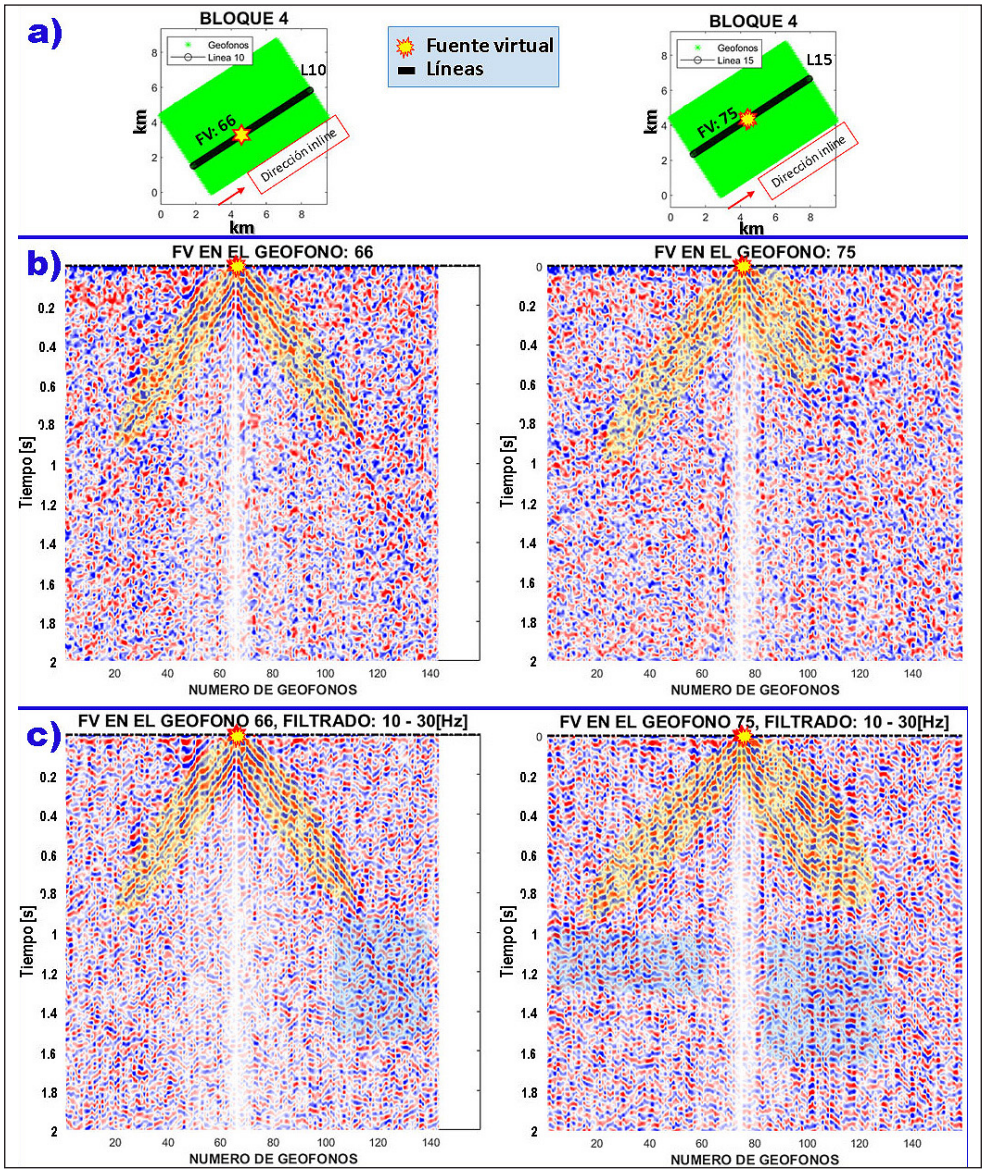

Figura 5. resultados de la *CC(t)*; a) ubicación de la *FV*:66 para la L10 y *FV*:75 para la L15; b) Pseudosección de tiros virtuales L10 y L15; c) Pseudosección de tiros virtuales L10 y L15, después del segundo filtrado (10-30 Hz).

normalización; 3) Realizar las *CC(t)*; 4) Descomposición de ondícula y reconstrucción a partir de un nivel; y 5) Apilado de las *CC(t)* reconstruidas.

Transformada de Ondícula

La transformada de ondícula es una herramienta matemática que permite obtener una representación, descomposición y reconstrucción de una señal que presenta cambios abruptos en sus componentes de tiempo-frecuencia en forma instantánea. *Daubechies (1992)*, sondeó la mayor parte de la teoría de ondícula y discutió los vínculos con otras áreas, especialmente el procesamiento de señales.

La transformada de ondícula hace un análisis de multi-resolución con ventanas de longitud variable, las cuales son adaptadas al cambio de frecuencia de la señal. Es decir, esta técnica permite el uso de ventanas grandes de tiempo en segmentos donde se requiere mayor precisión en bajas frecuencias, y ventanas angostas para el análisis en altas frecuencias *(Sheng, 1996)*.

Las ondículas, son funciones base de la transformada de ondícula, generadas a partir de una ondícula madre mediante traslaciones y dilataciones. Para llevar a cabo la transformada realizamos diversas pruebas con las ondículas: Haar, Morlet, Daubechies, Symlet, Coiflet y Meyer (Figura 6). Al final elegimos la ondícula de Meyer para descomponer y después reconstruir la señal de cada una de las *CC(t)*, ya que ésta aumentaba la relación señal-ruido más que las otras ondículas.

Análisis de velocidad y apilamiento

Mallat (1989) diseñó un algoritmo basado en un banco de filtros, que permite obtener una transformada de ondícula a partir de datos de interés. Una forma simple de ver la

aplicación de esta técnica, es pensar que la señal original (*S*) se subdivide al pasar por varios filtros en dos categorías: Aproximación (A) asociados a baja frecuencia y Detalle (D) para alta frecuencia (Figura 7). Este procedimiento se repite cada vez, hasta que se haya descompuesto la señal original en un determinado número de niveles para llegar a la precisión deseada. De este modo, se tiene un grupo de señales que representan a la señal original, pero todas ellas corresponden a diferentes bandas de frecuencia.

En la Figura 8, se muestra el cálculo de una ventana de 30 s de *CC(t)* y su descomposición en 6 niveles, usando la ondícula de Meyer. La señal *a6* de las componentes de aproximación es la de más baja frecuencia, dado que es la salida del último filtro pasa bajas del árbol de descomposición. Mientras que, las señales *di (i=1. . . 6)* son las componentes de alta frecuencia.

Después de hacer la descomposición con la ondícula de Meyer en cada una de las *CC(t)*, el siguiente paso fue reconstruir nuevamente la correlación considerando unas componentes y descartando otras. Descartamos las componentes de aproximación relacionadas a frecuencias por debajo de los 10 Hz ya que no son útiles. Dicho lo anterior, nos enfocamos en las componentes de detalle de altas frecuencias.

En la Figura 9 mostramos la técnica de reconstrucción de ondícula en 6 niveles de detalle para una pseudo-sección sísmica. Tomamos como ejemplo el geófono 44 (G44) de la L15 como fuente virtual y realizamos pruebas con 30 minutos de tiempo de correlación. Para los niveles d1, d2, d3 y d6 resulta complicado observar eventos reflectivos en la pseudo-sección sísmica.

Por otro lado, la reconstrucción con el nivel 4 (d=4) mejora sustancialmente las *CC(t)* en comparación con los

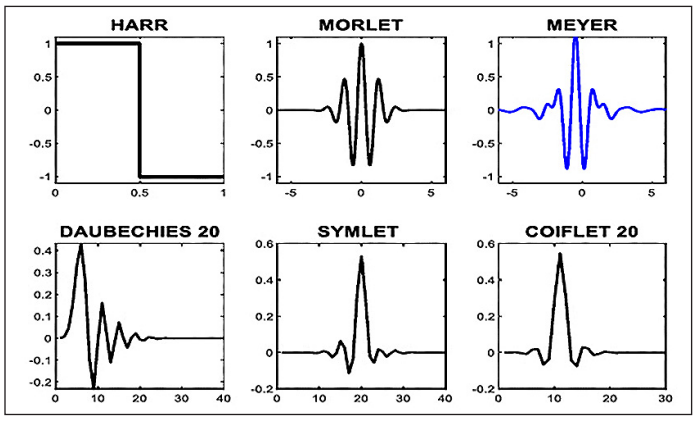

Figura 6. Familias de funciones ondícula. En color azul se resalta la ondícula de Meyer utilizada para este trabajo.

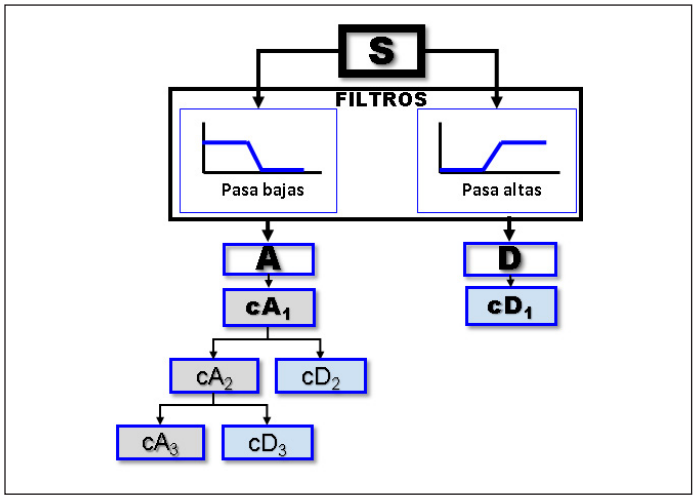

Figura 7. Diagrama de descomposición de señales. cA: coeficientes de aproximación; cD: coeficientes de detalle. Los subíndices representan el nivel de descomposición.

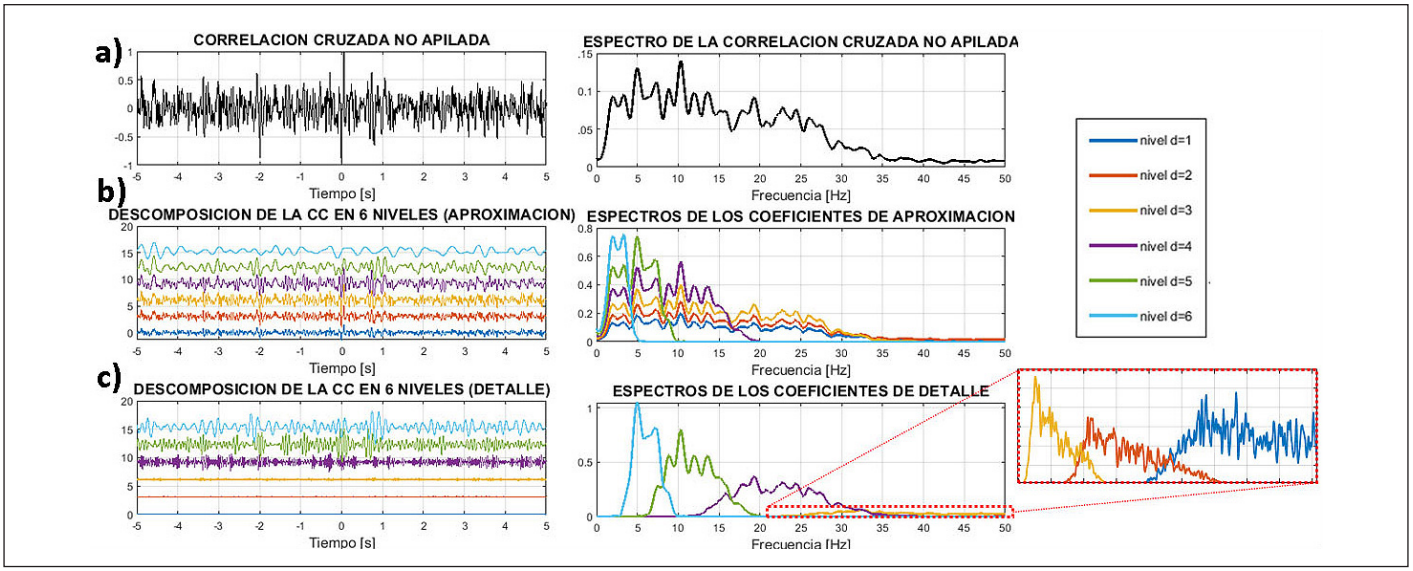

Figura 8. Descomposición con la ondícula de Meyer. a) *CC(t)* (ventana de 30 s) con su espectro de amplitudes. b) Descomposición en 6 niveles para los coeficientes de aproximación (dominio: tiempo y frecuencia). c) Descomposición en 6 niveles para los coeficientes de detalle (dominio: tiempo y frecuencia), en el recuadro en rojo se resaltan los niveles: 1, 2 y 3.

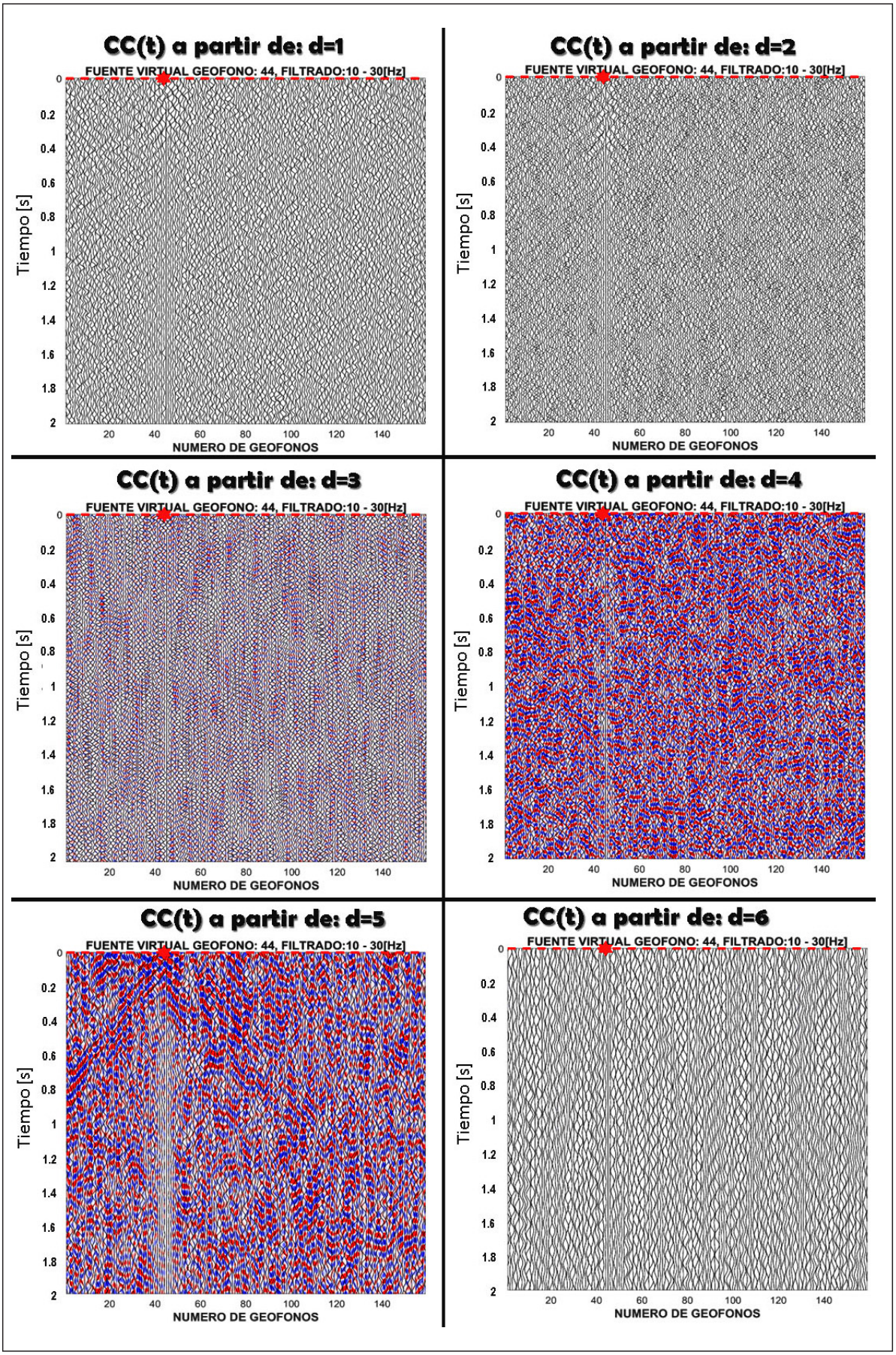

Figura 9. Fuente virtual G44, L15. Reconstrucción (a partir de cada nivel) de las *CC(t)* usando la ondícula de Meyer.

niveles mencionados anteriormente. Sin embargo, el mayor aporte de información en el rango de frecuencias que nos interesan es la reconstrucción con el nivel 5, ya que, se realzan y mejoran considerablemente los eventos reflectivos cercanos a la fuente virtual.

Una de las ventajas de usar algoritmos que utilizan ondículas se debe a que los datos se procesan a diferentes escalas o resoluciones. Es decir, cambia el contenido de frecuencia por longitud de onda. Esto nos ayudó a observar el grado de aporte que tiene cada banda de frecuencia en la *CC(t)* original y para descartar las que no se encuentran en los rangos de interés. En la siguiente sección hablaremos de la reconstrucción de las *CC(t)* a partir exclusivamente del nivel 5 y utilizando la ondícula de Meyer.

Reconstrucción de ondícula y apilado de las CC(t) a partir de un nivel

Una vez definidos el nivel y la ondícula con los que se reconstruirá la *CC(t)*, la siguiente metodología fue aplicada a todos nuestros datos. El orden de procesamiento quedó de la siguiente manera:

1. Blanqueamiento espectral,
2. Filtrado 1-30 Hz,
3. Normalización temporal,
4. Correlación Cruzada (*CC(t)*),
5. Descomposición de ondícula (en 6 niveles),
6. Reconstrucción de la *CC(t)*, usando la transformada inversa de la ondícula de Meyer (a partir del nivel 5),

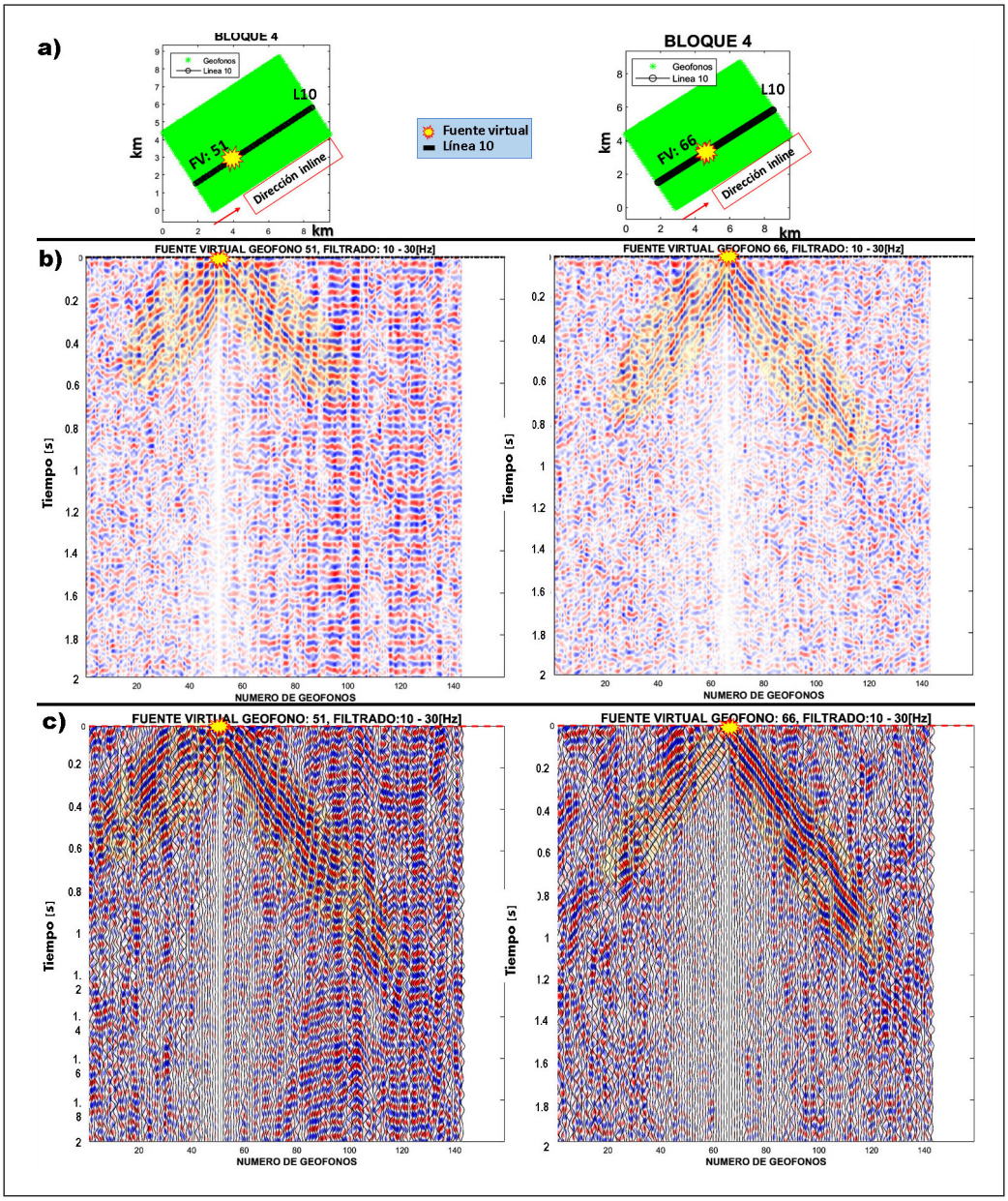

Figura 10. Comparación de las *CC(t)* para la L10. a) Bloque 4, ubicación de las *FV* (G51 y G) situadas a lo largo de la L10 en dirección *inline*. b) *CC(t)* sin la ondícula. c) *CC(t)* reconstruidas con la ondícula de Meyer a partir del n=5.

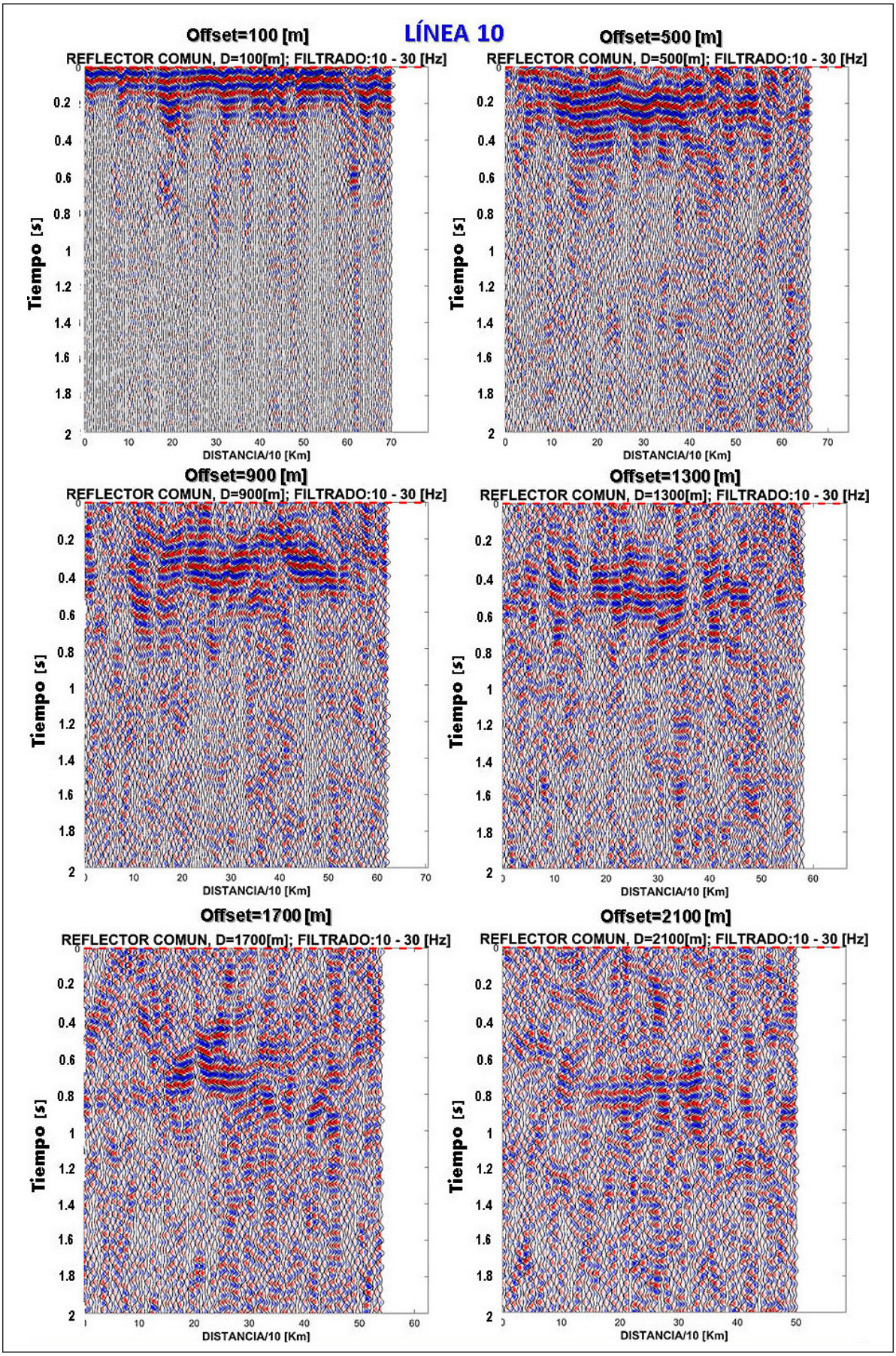

Figura 11. Pseudo-secciones de reflector común para la L10. Distancias entre fuente-receptor: 100, 500, 900, 1300, 1700 y 2100 m.

7. Apilado de las *CC(t)* (780 ventanas de 30 s, 6.5 h de grabación) y finalmente,
8. Segundo filtrado (10-30 Hz).

Cuando se usa el método de la ondícula se mejoran considerablemente los horizontes cercanos a la fuente y se aumenta la relación señal-ruido. En la Figura 10 mostramos ejemplos correspondientes a la L10 entre el apilado de las *CC(t)* con y sin la técnica de reconstrucción de ondícula. La parte a) corresponde a la ubicación de la *FV* a lo largo de cada una de las líneas. b) corresponde a las pseudo secciones de tiros virtuales sin el método de la ondícula. c) resultados de las pseudo secciones de tiros virtuales, cuando se descompone y posteriormente se reconstruyen las *CC(t)* con la ondícula de Meyer a partir del nivel 5.

Pseudo-secciones sísmicas con offset común

Después del pre-procesamiento descrito en la sección anterior, lo siguiente fue emplear la metodología que mencionamos previamente, con la finalidad de obtener una sección que nos defina las propiedades del subsuelo. En sísmica 2 y 3D, las trazas sísmicas pre-apiladas suelen ordenarse en planos de offset común (*COG*). Cabe recordar que el offset de una traza se define como la distancia entre la fuente y el receptor. La manera de organizar estos planos o conjuntos es agrupar las trazas por rango de inline-offset y crossline- offset.

Considerando a cada geófono como fuente y receptor, se reagruparon las *CC(t)* obtenidas con la ondícula de Meyer considerando un offset común. Esto quiere decir que, se fue desplazando la fuente a lo largo de la línea manteniendo constante la distancia entre fuente-receptor. El objetivo es generar una pseudo-sección con reflectores en común que permita visualizar horizontes delimitados por los cambios de impedancia en el subsuelo.

De manera ilustrativa, en la Figura 11 mostramos los resultados mencionados para la L10 del bloque 4. Las distancias D utilizadas entre fuente y receptor fueron de 100 m, 500 m, 900 m, 1300 m, 1700 m y 2100 m. Estos intervalos de distancias se desplazaron a lo largo de cada una de las líneas, obteniendo seis pseudo-secciones de reflector común por línea.

En general, en las imágenes podemos ver claramente que los offset cortos (100 y 500 m), favorecen los tiempos menores a 0.5 s, ya que delimitan y definen con una mayor continuidad los horizontes reflectivos superficiales, aunque con ligeras discontinuidades a lo largo de cada línea. A medida que el offset se incrementa, la información que existe en los extremos de nuestras pseudo-secciones se va perdiendo, ya que disminuye la resolución lateral debido a la falta de información en esos puntos. Por otro lado, en la parte central sucede lo contrario, ya que, al tener mayor apertura entre la fuente y el receptor, se aumenta la profundidad de investigación (periodos largos) y la delimitación en la parte central de estos nuevos horizontes reflectivos queda mejor definida.

Tomando como ejemplo la pseudo sección de la L10 (Figura 11), donde tenemos que la imagen es muy buena en especial para offsets de 100 m y 500 m, ya que se definen de manera excelente horizontes superficiales. Cuando se aumenta la distancia a 900 m, las partes laterales se comienzan a atenuar, lo que resulta que se pierda resolución lateral. En 1300 m de separación, los horizontes más superficiales se atenúan casi completamente y los que se encuentran mayores a 0.4 s se definen mejor en la parte central. Para un offset de 1700 m se profundiza llegando hasta 1 s, pero sólo la parte central se percibe con claridad. Caso similar a una distancia de 2100 m, en dónde se alcanza el tiempo más largo, pero con la menor resolución lateral en comparación con las otras distancias fuente-receptor.

Apilado a diferentes distancias

Con el objetivo de preservar la información que se encuentra en la parte más profunda sin perder la información de la parte somera (secciones de offsets cortos), realizamos un apilado de las trazas entre las pseudo-secciones con distintos offsets que obtuvimos anteriormente. En la Figura 12 se tiene un esquema que muestra cómo se realizó este apilado para dos offsets diferentes (100 y 500 m). El color rojo representa el desplazamiento a lo largo de toda la línea manteniendo constante un offset de 100 m, mientras que las líneas punteadas en color azul representan el desplazamiento para un offset de 500 m. También, apreciamos unas líneas continúas dadas en color verde y negro, las cuales representan los centros en común entre ambos offsets. Los centros en común fueron tomados como referencia para agrupar las trazas de ambas secciones y apilarlas posteriormente, obteniendo así una pseudo-sección total.

En la Figura 13 tenemos la pseudo-sección obtenida con el método de reflector común, usamos pseudo-secciones con offsets de: 100 m, 500 m, 900 m, 1300 m, 1700 m y 2100 m que posteriormente apilamos y obtuvimos la pseudo-sección

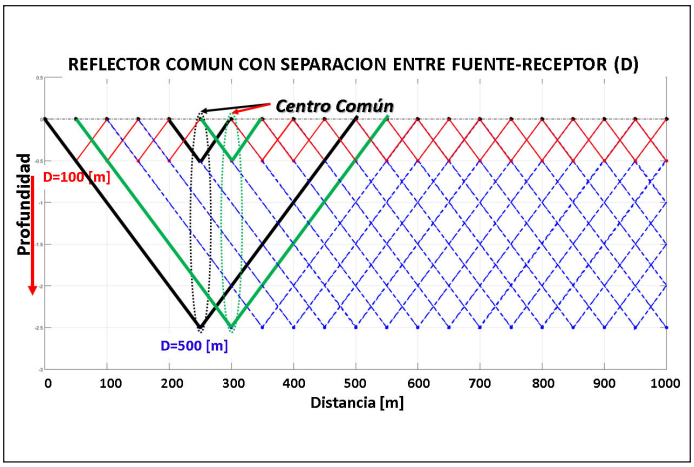

Figura 12. Representación esquemática del apilamiento entre 2 pseudo-secciones con offsets: 100 m y 500 m.

final. Las líneas amarillas delimitan algunos horizontes de lo que podrían considerarse como capas reflectoras a periodos de entre: 0.1-0.7 s, la parte superficial y central quedan muy bien caracterizadas, ya que se puede seguir lateralmente la tendencia de algunos horizontes reflectores hasta los 0.9 s.

Las Figuras 14 y 15, muestran los resultados finales de las pseudo-secciones para las líneas del bloque 4. Es claro que en todos los casos se definen los horizontes superficiales con una excelente continuidad. En color amarillo se delimitan paquetes de capas reflectoras llegando en la parte central a tiempos de 0.7 s y 1.2 s para las L5 y L10, respectivamente.

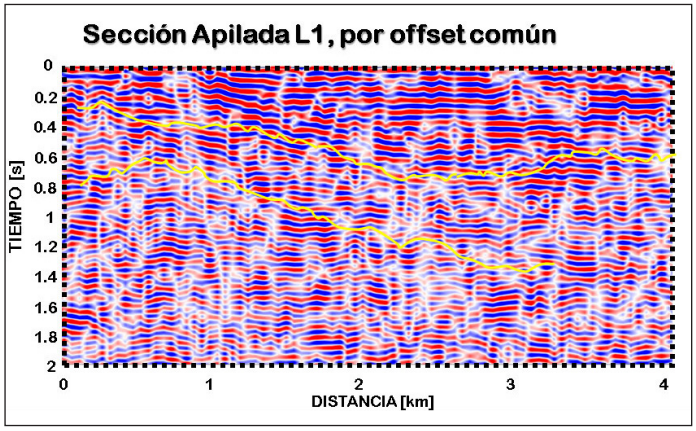

Figura 13. Pseudo-secciones de la L1 agrupadas por offset común y posteriormente apiladas con offsets: 100 m, 500 m, 900 m, 1300 m, 1700 m y 2100 m. Las líneas amarillas representan paquetes de capas reflectoras.

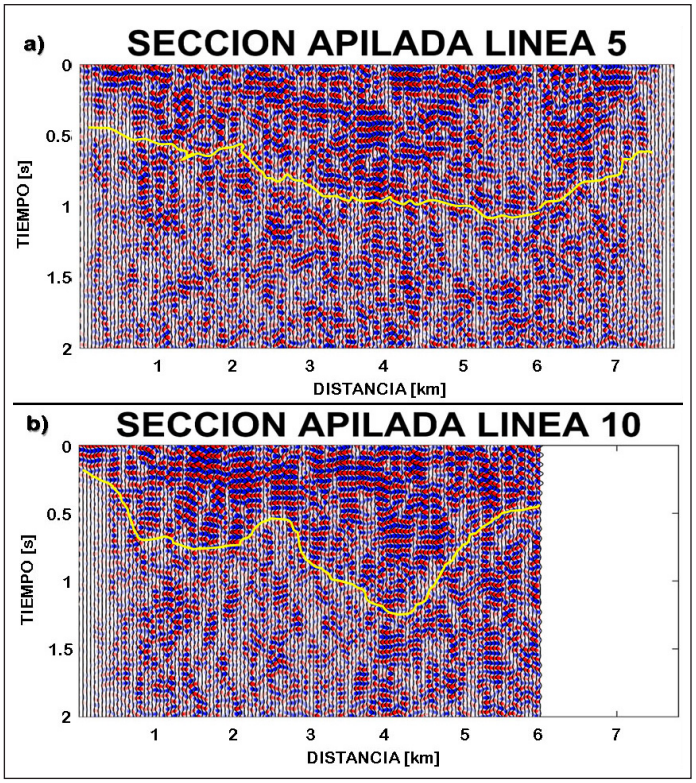

Figura 14. Pseudo-secciones de las L5 y L10 apiladas con offsets: 100 m, 500 m, 900 m, 1300 m, 1700 m y 2100 m.

La L10 presenta en la parte superficial capas muy planas y uniformes, similar al caso de la L15, donde se alcanzan tiempos de hasta 1 s.

Según nuestra apreciación en la L25 se observan posiblemente unos paquetes de estratos (líneas en color amarillo) más recargados hacia el lado izquierdo, uno para tiempos más largos (tiempos de 1.4 y 0.8 s) y otro para tiempos menores (tiempos de 0.7 y 0.2 s). Esto, hace que haya una variación con los resultados obtenidos en las otras líneas.

Alcances del Método

Como mencionamos anteriormente, lo que se busca con esta investigación es comparar el aporte que pueden tener los métodos relacionados con sísmica pasiva en el área de la exploración sísmica. Para evaluar los alcances desarrollados por el método usado, contamos con una sección sísmica de fuente explosiva migrada en profundidad muy cerca de las líneas: L10 y L15 (Figura 16b).

En la Figura 16c se muestra una sección sísmica convencional (con fuente sísmica de dinamita) migrada en profundidad y un registro de velocidades de ondas P y S, obtenido a partir de información de registros geofísicos de pozo (Figura 16d). La sección sísmica convencional muestra claramente capas reflectoras muy marcadas a profundidades de entre 2 y 4 km. Si hacemos un análisis de las capas de la sección sísmica y el modelo de velocidades, podemos dividir la sección sísmica en varios bloques según su profundidad:

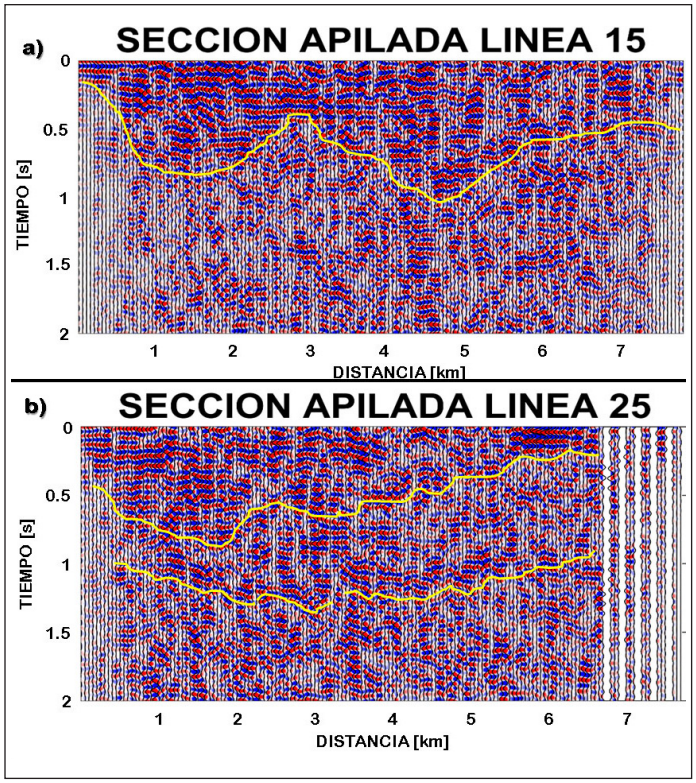

Figura 15. Pseudo-secciones de las L15 y L25 apiladas con offsets: 100 m, 500 m, 900 m, 1300 m, 1700 m y 2100 m.

1. Para el primer bloque (sección más superficial), las velocidades de ondas P (Vp) en promedio son de 3 km/s hasta los 800 m de profundidad, haciendo un tiempo de viaje doble de 0.53 s.
2. La segunda capa va de los 800 m a los 1100 m de profundidad, con una Vp de 2.85 km/s y un tiempo doble de viaje de 0.21 s.
3. La tercera capa corresponde a un intervalo de profundidad de1100 a 1500 m con Vp de 3.5 km/s y un tiempo doble de 0.23 s.
4. La capa siguiente tiene un espesor de 300 m con una Vp de 5 km/s y un tiempo doble de 0.12 s.
5. Posteriormente, en el rango de 1800 a 2200 m de profundidad la Vp llega a 4.5 km/s y el tiempo de viaje doble para ese intervalo seria de 0.18 s.
6. La sexta capa tiene un espesor de 300 m y Vp promedio de 4 km/s, con un tiempo de viaje doble de 0.15 s.
7. Finalmente, el ultimo bloque tiene un tiempo de viaje doble de 0.13 s, aproximadamente.

Para esta sección sísmica con fuente de dinamita migrada en profundidad, el tiempo de viaje total de las ondas sísmicas desde la parte superficial hasta los 3 km de profundidad es de aproximadamente 1.55 s, lo anterior lo resumimos en la Tabla 1. Para el caso de las secciones de sísmica pasiva, los periodos más largos de reflejo varían entre 0.8 s a 1.3 s, aproximadamente. Esto indica que los resultados que hemos obtenido con sísmica pasiva son alentadores al mostrar una relación con los que se observan en la sección sísmica de fuente convencional. Aunque no definen con claridad las partes más profundas de los posibles yacimientos, las formaciones y estructuras geológicas someras e intermedias pueden ser identificables. Lo anterior se observa mejor en la Figura 16, donde se tiene la comparación entre la sísmica convencional *versus* la sísmica pasiva, ambas migradas en profundidad.

La Figura 16 muestra: a) La ubicación de la sección sísmica con fuente de dinamita (color rojo) y las líneas más cercanas a ella de la sísmica pasiva (L10 y L15) mostradas en color azul. b) Las pseudo-secciones L10 y L15 de sísmica pasiva migradas en profundidad y c) la sección de sísmica convencional migrada en profundidad. Las líneas amarillas en las tres secciones corresponden a las primeras interpretaciones que delinean las principales estructuras geológicas y los mayores cuerpos reflectores. En las zonas de color amarillo de los datos de ruido se observan horizontes reflectores alrededor de los 2 km de profundidad, lo que coincide con los horizontes observados en la sísmica convencional (Figura 16c). Aunque no se definen con claridad los detalles de las capas reflectoras, si es posible observar cómo se empiezan a definir de manera tenue los límites a partir de las reflexiones virtuales indicando la presencia de posibles formaciones geológicas. Finalmente, en la Figura 16 d) se presentan los registros sónicos y el modelo de velocidades utilizados para la conversión de tiempo a profundidades en las secciones de sísmica pasiva.

Tabla 1. Resultados del tiempo doble de viaje a distintas profundidades.

Profundidad [m]	Vp Promedio [m/s]	Tiempo doble de viaje [s]	Tiempo Total de viaje [s]
0 - 800	3000	0.53	0.53
800 - 1100	2850	0.21	0.74
1100 -1500	3500	0.23	0.97
1500 -1800	5000	0.12	1.09
1800 - 2200	4500	0.18	1.27
2200 - 2500	4000	0.15	1.42
2500 - 3000	4500	0.13	1.55

Figura 16. a) Ubicación de las L10 y L15 (color azul) y de la sección sísmica con fuente de dinamita, migrada en profundidad (color rojo). b) *Pseudo-secciones sísmicas de tiros virtuales* (L10 y L15). c) Secciones sísmica con fuente de dinamita, migrada en profundidad. d) Modelo de velocidades.

Conclusiones

Se obtuvieron secciones sísmicas de ruido con el objetivo de delimitar estructuras geológicas asociadas a yacimientos de hidrocarburos. Utilizamos datos de sísmica pasiva de un arreglo rectangular localizado al noreste de la República Mexicana. Con el método de Interferometría Sísmica (*IS*), fueron procesadas 954 trazas de ruido sísmico de 6.5 h de grabación, lo cual nos permitió extraer la función de Green mediante el uso de correlaciones cruzadas (*CC(t)*).

Las *CC(t)* obtenidas (también llamadas *pseudo-secciones sísmicas de tiros virtuales*) fueron procesadas para la extracción de información estructural y de velocidad subsuperficial. Los resultados los reagrupamos en Gathers de Offset Común (*COG*), con el objeto de generar imágenes del campo de velocidades en el subsuelo en términos de secciones sísmicas de offset cero.

Además, realizamos un procesamiento que consistió en aplicar el método de la transformada de ondícula, para descomponer y reconstruir las *CC(t)* a partir de la ondícula de Meyer, mejorando la calidad de las *CC(t)*. En este caso los resultados mejoraron substancialmente, mostrando los reflectores esperados.

Al aplicar el método de Transformada de ondícula antes del apilado de las *CC(t)*, se mejoran considerablemente las pseudo-secciones sísmicas. Así mismo, al usar el enfoque de offset común se detectaron horizontes reflectores con una excelente resolución en la parte superficial. Sin embargo, a mayor distancia fuente-receptor la resolución de dichos reflectores disminuía. Para compensar esta pérdida, se aplicó

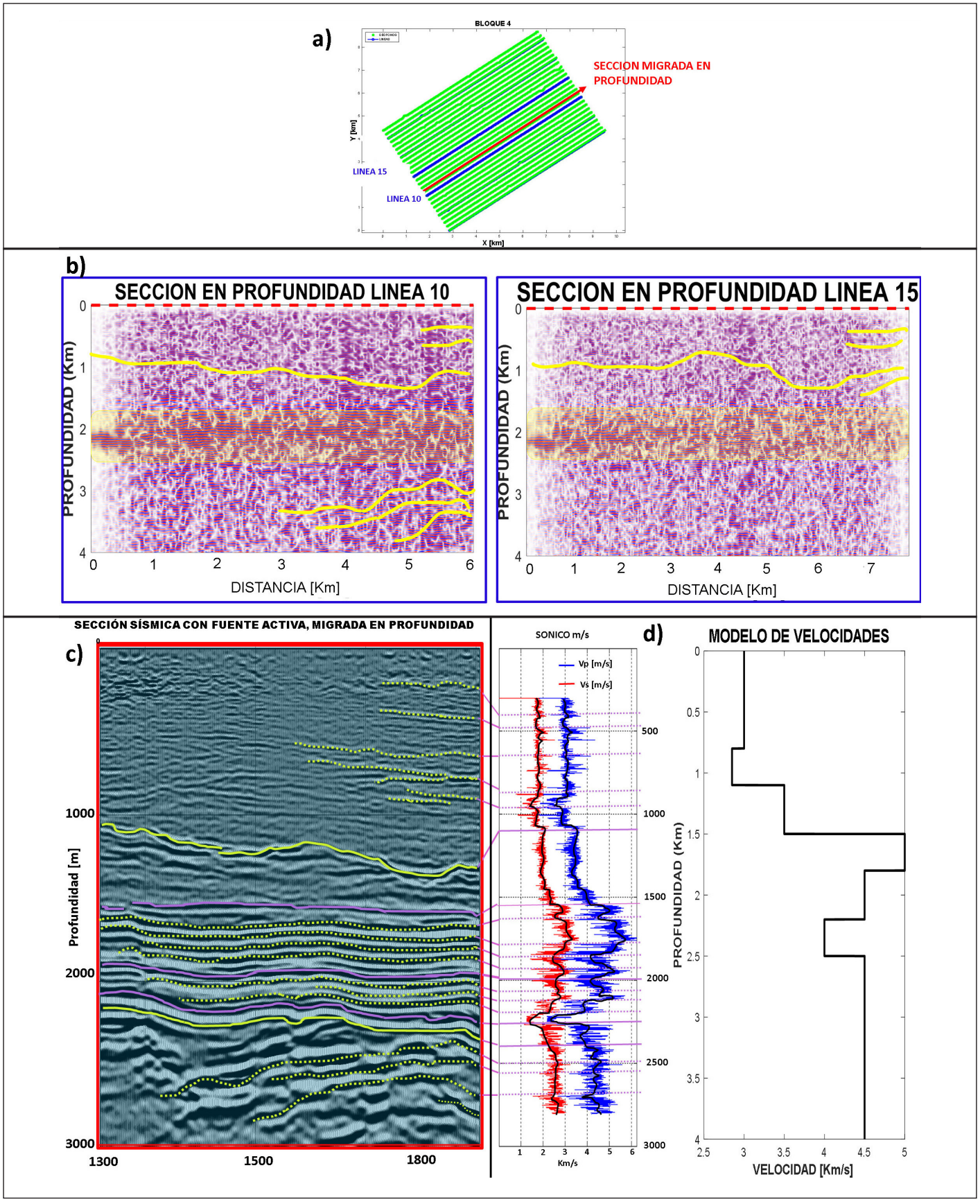

Figura 16. a) Ubicación de las L10 y L15 (color azul) y de la sección sísmica con fuente de dinamita, migrada en profundidad (color rojo). b) *Pseudo-secciones sísmicas de tiros virtuales* (L10 y L15). c) Secciones sísmica con fuente de dinamita, migrada en profundidad. d) Modelo de velocidades.

el apilamiento de varias secciones sísmicas con distintos offsets, aumentando así la profundidad de investigación y mejorando nuevamente la resolución de la pseudo-sección sísmica final.

El flujo de procesamiento para la generación de pseudo-secciones de tiros virtuales quedó de la siguiente manera:

1. Blanqueamiento espectral.
2. Filtrado 1-30 Hz.
3. Normalización temporal.
4. Correlación Cruzada (*CC(t)*).
5. Descomposición de ondícula (en 6 niveles).
6. Reconstrucción de la *CC(t)*, usando la transformada inversa de la ondícula de Meyer (a partir del nivel 5).
7. Apilado de las *CC(t)* (780 ventanas de 30 s, 6.5 h de grabación) y finalmente,
8. Segundo filtrado (10-30 Hz).

En consecuencia, sí se logró aumentar la relación señal-ruido y se mejoraron los ajustes de los pulsos reflejados en el mismo tiempo de las posibles capas que se consideraron como reflectoras. Aunque con ello, no se mejora sustancialmente la imagen sísmica a mayores profundidades.

Con el objeto de comprobar nuestros resultados, las secciones obtenidas de la sísmica pasiva convertidas a profundidad con el modelo de velocidades mostrado en la Figura 16d, fueron comparadas con una sección sísmica convencional (también llamadas secciones de sísmica "activa") migrada en profundidad. Obtuvimos buena similitud en los horizontes reflectores cercanos a los 2 km de profundidad, donde es posible observar como se empiezan a definir de manera tenue los limites de posibles formaciones geológicas. A pesar de que se exploraron yacimientos correspondientes a formaciones geológicas conocidas por su impacto económico, nuestros resultados indican que es posible alcanzar estas profundidades, por lo que podemos afirmar que sí se están definiendo los limites más someros asociados a dichas formaciones. No obstante, consideramos que hace falta incluir un mayor número de trazas y offsets en un procesamiento de los datos de ruido de manera tridimensional para definir una pseudo-sección sísmica confiable. Al agrupar las *CC(t)* por *COG´*s, se requieren adicionar a la iluminación de los reflectores comunes, todas las contribuciones de las señales con sus aportes azimutales para mejorar la falta de precisión en el establecimiento de la velocidad de reflexión. Con ello, esperaríamos alcanzar mayor definición en la continuidad de las estructuras profundas y mejorar la imagen sísmica. Por otro lado, delimitar los espesores totales de estas capas, es tarea de futuras investigaciones.

El aporte de nuestro trabajo contempló el reto de realizar una comparación de imágenes usando nuestros datos procesados de ruido contra una sección real en 3D de la sísmica convencional migrada en profundidad. Consideramos que nuestra técnica es, sin duda, una alternativa confiable, más económica, rápida y amigable con el ambiente, en comparación con los sendos estudios de sísmica de reflexión. Sin embargo, aunque los resultados de la sísmica pasiva nos dan una idea cualitativa de cómo es la distribución de las capas litológicas de una manera práctica y mucho más económica, nunca alcanzarán el detalle y definición de las imágenes sísmicas de alta resolución 3D-3C.

Referencias

Bensen, G.D., Ritzwoller, M. H., Barmin, M. P., Levshin, A. L., Lin F., Moschetti, M. P., Shapiro and Yang Y. (2007). Processing seismic ambient noise data to obtain reliable broadband Surface wave dispersion measurements. *Geophysics J. Int.* 169,1239- 1260.

Brenguier, F., D. Clarke, Y. Aoki, N. M. Shapiro, M. Campillo, and V. Ferrazzini (2011). Monitoring volcanoes using seismic noise correlations, Comptes Rendus Geosci., 343(8-9), 633–638, doi:10.1016/j.crte.2010.12.010.

Bonnefoy-Claudet, S., Cotton, F. y Bard, Pierre-Yves, (2006). The nature of noise wavefield and its application for site effect studies. A literatura review. Earth Science Reviews

Claerbout, J. (1968). Synthesis of layered medium from its acoustic transmission response. *Geophysics*, vol. 33, no. 2. **https://doi.org/10.1190/1.1439927**

Daubechies, I. (1992). Ten Lectures on Wavelets. *The Society for Industrial and Applied Mathematics, Philadelphia, Pennsylvania 1992*. **https://epubs.siam.org/doi/pdf/10.1137/1.9781611970104.fm**

Douze, E. J., (1967). Short-period seismic noise. Bulletin of the Seismological Society of America, 57, 1, 55-81.

Draganov, D., Wapenaar, K., Mulder, W., Singer, J. and Verdel, A. (2007). Retrieval of reflections from seismic background-noise measurements. *Geophysics. Res. Lett., 34*, L04305, L04305, doi:10.1029/2006GL028735, 2007.

Draganov, D., Campman, X., Thorbecke, J., Verdel, A. and Wapenaar, K. (2009). Reflection images from ambient seismic noise. *Geophysics*, 74(5), A63–A67. 39. **https://doi.org/10.1190/1.3193529**

Draganov, D., Campman, X., Thorbecke, J., Verdel, A., Wapenaar, K. (2013). Seismic exploration-scale velocities and structure from ambient seismic noise (>1 Hz). *Journal of Geophysical Research: Solid Earth*, Vol. 118, 4345-4360.

Duputel, Z., V. Ferrazzini, F. Brenguier, N. Shapiro, C. M.,. A. Nercessian, M. Campillo, and A. Nercessian (2009). Real time monitoring of relative velocity changes using ambient seismic noise at the Piton de la Fournaise volcano (La Réunion) from January 2006 to June 2007, J. Volcanol. Geotherm. Res., 184(1-2), 164–173, doi:10.1016/j.jvolgeores.2008.11.024.

Gouédard, P., Stehly, L., Brenguier, F., Campillo, M., Colin de Verdière, Y., Larose, E., Margerin, L., Roux, P., Sánchez-Sesma, F. J., Shapiro, N. M., Weaver, R. L. (2008). Cross-correlation of random fields: mathematical approach and applications. *Geophysical Prospecting*, 56,375-393.

Lin, F.C., Moschetti, M. P. and Ritzwoller, M. H. (2008). Surface wave tomography of the western United States from ambient seismic noise: Rayleigh and Love wave phase velocity maps. *Geophysics. J. Int.*, 173 (1),281-298. **https://doi.org/10.1111/j.1365** 246X.2008.03720.x

Lobkis, O. I. and Weaver, R. L. (2001). On the emergence of the Green's function in the correlations of a diffuse field. *J. Acoust. Soc. Am.*, 110, 3011-3017.

Mallat S. (1989). A theory for multiresolution signal decomposition: the wavelet representation. *IEEE Pattern Anal. And Machine Intell.*, vol. 11, no.7, pp. 674-693

Nakata, N., Snieder, R., Tsuji, T., Larner, K. and Matsuoka, T. (2011). Shear wave imaging from traffic noise using seismic interferometry by cross coherence. *Geophysics*, 76(6), SA97–SA106.**https://doi.org/10.1190/geo2010-0188.1**

Okada, Hiroshi, (2003). The microtremor survey method. Geophysical monographs series, 12. Society of Exploration Geophysics, E. U. A.

Roux, P., Sabra, K. G., Gerstoft, P., Kuperman, W. A. and Fehler, M. C. (2005). P-waves from cross-correlation of seismic noise. *Geophysics. Res. Lett.*, 32 (19), L19303, doi:10.1029/2005GL023803

Sabra, K. G., Gerstoft, P., Roux, P. and Kuperman, W. A. (2005). Surface wave tomography from microseisms in Southern California. *Geophys. Research Letters*, vol 32, L14311. 40.

Shapiro, N. M., y Campillo, M. (2004). Emergence of broadband Rayleigh waves from correlations of the ambient seismic noise. *Geophysical Research Letters*, vol 31, L07614. 7614, doi:10.1029/2004GL019491,

Shapiro, N. M., Campillo, M., Stehly, L. and Ritzwoller, M. H. (2005). High-resolution surface wave tomography from ambient seismic noise. Science, 307, 1615 – 1618.

Sheng, Y., (1996). *The Transforms and Applications Handbook*. CRC Press, 1996. **https://doi.org/10.1201/9781315218915**

Sthely, L., Campillo, M. and Weaver, R.L. (2008). Reconstructing Green's function by correlation of the coda of the correlation (C3) of ambient seismic noise. *Journal of Geophysical Research*, vol. 113, B11306, doi:10.1029/2008JB005693, 2008

Toksöz, M. N. y Lacoss, R. T., 1968. Microseisms: mode structure and sources. Science 159.

Xu, Z., Juhlin, C., Gudmundsson, O., Zhang, F., Yang, C., Kashubin,, A. and Luth, S. (2012). Reconstruction of subsurface structure from ambient seismic noise: An example from Ketzin, Germany. *Geophys. J. Int.*, 189, 1085–1102.

Wapenaar, K. (2004). Retrieving the elastodynamic Green's function of an arbitrary inhomogeneous medium by cross correlation. *Physical Review Letters*, 254301

Wapenaar, K. and Fokkeman, J. (2006). Green's function representations for seismic interferometry. *Geophysics*, Vol 71, No. 4. **https://doi.org/10.1190/1.2213955**

Wapenaar, K., Draganov, D., Snieder, R., Campman, X. and Verdel, A. (2010). Tutorial on seismic interferometry: Part 1 – Basic principles and applications. *Geophysics*, Vol. 75, No. 5. **https://doi.org/10.1190/1.3457445**

Yilmaz O. (1987). Seismic Data Analysis: Processing, inversion, and interpretation of seismic data. *Investigations in Geophysics, no. 10. Society of Exploration Geophysics* SEG, Tulsa Oklahoma, USA.

Yilmaz, O. (2001). Seismic Data Analysis: Processing, Inversion, and Interpretation of Seismic Data. *Society of Exploration Geophysicists*, 2nd edition, 2001.

Geofísica Internacional (2023) **62-1**: 419 - 428

Estructura del subsuelo de la Sabana de Bogotá. Análisis de dispersión de ondas superficiales a partir de sismos y ruido sísmicos

Francisco José Chávez-García[1], Hugo Monsalve-Jaramillo[2] y Joaquín Vila-Ortega[3]

Resumen

Se presentan resultados del análisis de componentes verticales de registros de sismos y ruido sísmico en la Sabana de Bogotá con el objetivo de explorar la estructura del subsuelo. En el caso de los registros de sismos, se analizaron directamente las ondas de Rayleigh presentes en los registros para estimar velocidades de grupo. Para los registros de ruido sísmico utilizamos el método de interferometría sísmica que permite estimar funciones de Green a partir de la correlación cruzada. El promedio de esas correlaciones cruzadas permitió recuperar pulsos de ondas Rayleigh entre pares de estaciones. En todos los casos estimamos curvas de dispersión de velocidad de grupo. Los resultados muestran el impacto de la geología en los valores de velocidad de grupo en la región de estudio. Observamos diferencias entre trayectorias contenidas en los sedimentos cuaternarios que cubren la Sabana de Bogotá y aquellas que incluyen parte de su trayecto por rocas del Cretácico. El contraste de impedancia estimado entre los sedimentos superficiales y los estratos subyacentes sugiere que la amplificación del movimiento sísmico excede un factor de 10. La deficiente cantidad y calidad de los datos limitaron los alcances del este trabajo. Los rangos de frecuencia de los resultados no coincidieron para las distintas fuentes de datos, lo que obstaculizó las comparaciones entre trayectorias. A pesar de esas limitaciones, estos resultados contribuyen a mostrar la relevancia de los efectos de sitio en la Sabana de Bogotá y la necesidad de tomarlos en cuenta para estimar el movimiento durante sismos futuros en esta zona.

Palabras clave: Correlación cruzada, Ondas de Rayleigh, Dispersión de velocidad de grupo, Efectos de sitio.

Abstract

We present the results of the analysis of vertical component from earthquake and seismic noise records obtained in the Sabana de Bogotá to determine subsoil structure in that region. Rayleigh waves present in the earthquake data were processed to estimate to estimate group velocities. In the case of seismic noise, we used seismic interferometry to estimate Green's functions between stations from average cross-correlation. Rayleigh wave pulses were recovered between stations from seismic noise. We processed the results to estimate group velocities in all cases. The results show the impact of geology on group velocities in the studied region. Different station pairs show varying group velocities depending on the age of the rocks along the paths. Our estimated impedance contrast between surficial deposits and underlying bedrock suggests possible amplification of ground motion larger than a factor of 10. The poor quality and the limited quantity of our data limited the comprehensiveness of our results. The frequency ranges of the results showed poor overlap, hindering comparisons among paths. In spite of their limitations, our results highlight the importance of site effects in the Sabana de Bogotá and the need to take them into account to estimate ground motion for future events in that region.

Keywords: Cross-correlation, Rayleigh waves, Group velocity dispersion, Site effects.

Received: May 17, 2022; October 18, 2022; published on-line: January 1, 2023.

Editorial responsibility: Arturo Iglesias Mendoza

* Corresponding author: Francisco J. Chávez-García
[1] Coordinación de Ingeniería Sismológica, Instituto de Ingeniería, Universidad Nacional Autónoma de México, Ciudad Universitaria, Coyoacán 04510 CDMX, México, email: paco@pumas.ii.unam.mx, orcid: 0000-0002-5490-9792
[2] Centro de Estudios e Investigaciones de la Facultad de Ingeniería, Universidad del Quindío, Cra. 15 # 12N Armenia, Quindío, Colombia, email: hugom@uniquindio.edu.co
[3] Centro de Estudios e Investigaciones de la Facultad de Ingeniería, Universidad del Quindío, Cra. 15 # 12N Armenia, Quindío, Colombia, email: jjvilaortega@uniquindio.edu.co, orcid: 0000-0001-9358-4903

Francisco J. Chávez-García, H. Monsalve-Jaramillo, J. Vila-Ortega

https://doi.org/10.22201/igeof.2954436xe.2023.62.1.1449

Introducción

La ciudad de Bogotá, capital de Colombia, está expuesta un riesgo sísmico importante. Si bien la sismicidad de la región es moderada, en los últimos 500 años han ocurrido al menos 8 sismos que han alcanzado intensidades de hasta IX en esa ciudad (Dimaté *et al.*, 2005). Bogotá concentra una parte significativa de la infraestructura económica de ese país. Por ello, aunque la peligrosidad sísmica sea moderada, el riesgo sísmico, la magnitud de las posibles pérdidas económicas por la ocurrencia de sismos, es elevado. Una estrategia para la mitigación de ese riesgo es buscar entender los mecanismos que gobiernan el movimiento del terreno que se ha observado durante los sismos pasados. Ello permitiría estar mejor preparados para predecir el movimiento esperado en el futuro y establecer los requisitos necesarios en las obras de infraestructura para protegerlas en caso de sismos (Chávez-García, 2007).

Uno de los factores que controlan el movimiento durante sismos es la estructura del subsuelo bajo la zona de interés, los efectos de sitio. El contraste en las propiedades mecánicas de los materiales que forman el subsuelo modifica el movimiento sísmico y puede ocasionar amplificaciones importantes del mismo en suelos blandos. Los parámetros relevantes para estimar efectos de sitio son observables con relativa facilidad, en comparación por ejemplo con los parámetros de la fuente para sismos futuros. Aun un simple mapa geológico nos permite distinguir entre un subsuelo formado por rocas cristalinas o suelos blandos. Los efectos de sitio pueden ocasionar diferencias en la intensidad del movimiento sísmico observado de dos unidades en sitios muy cercanos, para los cuales los factores de fuente y trayecto son los mismos (Chávez-García *et al.*, 1990).

En este trabajo presentamos resultados de un estudio de la estructura del subsuelo en la región de la Sabana de Bogotá a partir del análisis de registros de sismos pequeños y de registros de ruido sísmico. Utilizamos datos de dos redes: la que opera el Servicio Geológico Colombiano (SGC) y una red de estaciones de banda ancha operada por la Universidad Nacional (Red Sísmica de la Sabana de Bogotá, RSSB). Los registros de ruido sísmico fueron analizados mediante la interferometría sísmica de los componentes verticales. Ello permitió estimar pulsos de ondas Rayleigh y determinar curvas de dispersión entre estaciones. A esos resultados se agregó el análisis de ondas Rayleigh contenidos en los registros de 12 pequeños sismos. Sin embargo, la deficiente cantidad y calidad de los datos limitaron los alcances del proyecto. El número de trayectorias para las cuales se estimaron curvas de dispersión fue pequeño e hizo imposible considerar el cálculo de una tomografía. Adicionalmente, los rangos de frecuencia de los resultados no coincidieron para las distintas fuentes de datos, lo que obstaculizó las comparaciones entre trayectorias. A pesar de esas limitaciones, nuestros resultados muestran la relevancia de los efectos de sitio en la Sabana de Bogotá y la necesidad de tomarlos en cuenta para estimar el movimiento durante sismos futuros en esa zona.

Zona de estudio y datos

La Sabana de Bogotá es una estructura sedimentaria ubicada junto al borde occidental de la Cordillera Oriental, cerca de la parte central de su extensión longitudinal (Figura 1). Esta estructura comprende la parte alta de la cuenca del río Bogotá, tiene una extensión aproximada de 4,300 km^2 y una altitud promedio de 2,600 m.s.n.m.m. Es el centro agroindustrial más importante de Colombia y ahí se localizan la ciudad capital y alrededor de 20 centros urbanos más. Concentra cerca del 20% de la población del país.

La estratigrafía de la Sabana de Bogotá ha sido estudiada tanto desde el punto de vista geológico (Helmens y van der Hammen, 1994; Torres *et al.*, 2005), como con objetivos de microzonificación sísmica y predicción del movimiento esperado para sismos futuros (Ingeominas, 1997; FOPAE, 2010). Se trata de una cuenca compleja con sedimentos de edad cenozoica. La zona urbana de Bogotá se asienta sobre la formación Bogotá, la cual consiste en depósitos lacustres paludales del Cuaternario (edad menor a 2.6 ma) distribuidos en toda la planicie y en los valles que desembocan en ella. Las rocas circundantes datan del Cretácico (Figura 1). El contraste de edad entre esas formaciones se debe traducir en un contraste de impedancia significativo entre los sedimentos directamente bajo la ciudad capital y las rocas subyacentes (Park y Elrick, 1998). Ese contraste ha amplificado el movimiento sísmico observado durante sismos pasados y amplificará de modo similar el movimiento que afectará a Bogotá durante los sismos futuros.

Para este estudio recopilamos registros de ruido sísmico de dos redes sísmicas. La que opera el Servicio Geológico Colombiano (SGC) y la Red Sísmica de la Sabana de Bogotá (RSSB), instalada y operada por el Departamento de Geofísica de la Universidad Nacional. Elegimos arbitrariamente procesar ventanas de una hora de duración de vibración ambiental. Esa duración es adecuada para el rango de distancias entre estaciones y facilita la búsqueda de registros simultáneos. Los registros de ruido del SGC provienen de 6 instrumentos de la red que opera esa institución (Tabla 1). El periodo de registro utilizado comprende del 27 de octubre al 30 de diciembre de 2018 para las estaciones BOG, ROSC e ICBF y del 27 de octubre al 30 de noviembre de ese año para las estaciones CVER, ROSCH y TABC. Aunque se trata de 6 instrumentos, ROSC (sismógrafo de banda intermedia) y ROSCH (acelerógrafo) están colocados en el mismo sitio, por lo que solo contamos con datos de 5 sitios de registro. Por ello, hay un total de 10 parejas de estaciones para las cuales es posible calcular correlaciones cruzadas de ruido sísmico. Un problema inmediato es la heterogeneidad de sensores

de las estaciones utilizadas, problema que no se soluciona al corregir los registros por la respuesta instrumental. En efecto, al corregir el registro por respuesta instrumental nos acercamos al movimiento del punto en el que se instaló la estación sísmica pero ello no corrige las limitaciones de la respuesta del sensor en frecuencia. La Tabla 1 indica que los seis instrumentos de registro incluyen estaciones sismológicas de banda ancha, una estación de banda intermedia, una de periodo corto y dos acelerógrafos. La respuesta de la estación de banda intermedia no afecta los resultados pues los límites de esa estación se encuentran a periodos mayores a 20 s y registra correctamente el movimiento para frecuencias superiores a 0.05 Hz. En cambio, el sismómetro de periodo corto limita la banda de frecuencias para la que es posible obtener correlaciones cruzadas. En el caso de las estaciones con acelerógrafos, encontramos que la mejor solución era integrar esos registros antes de calcular correlaciones cruzadas con los obtenidos en estaciones sismológicas. Aunque la integración numérica afecta la calidad del registro, es preferible correlacionar las trazas de velocidad obtenidas por sismógrafos con trazas de velocidad integradas a partir de registros de aceleración. El número de ventanas analizadas para cada par de estaciones y la distancia entre ellas se muestra en la Tabla 2.

Adicionalmente a los datos del SGC, analizamos registros de ruido sísmico en tres estaciones de la RSSB. Se trata de una red de estaciones sismológicas de manufactura rusa y sensores de banda ancha (respuesta plana entre 0.016 y 50 Hz). Sólo utilizamos datos de tres estaciones (Figura 1) debido a dos razones: la localización de otras estaciones no era útil para los objetivos de este trabajo; la baja calidad de los registros que no permitió seleccionar un número de ventanas de registro continuo de una hora adecuado. Aunque para la pareja de estaciones USME-ZIPA (distancia entre estaciones de 66.5 km) analizamos 3,829 ventanas de una hora, para las parejas CHRL-USME (distancia entre estaciones de 98.3 km) y CHRL-ZIPA (distancia entre estaciones de 138.1 km) solo fue posible analizar 202 y 283 ventanas de ruido sísmico.

Inicialmente se había contemplado limitar el análisis al ruido sísmico. Sin embargo, las restricciones en el número de estaciones y consecuentemente en el número de pares de estaciones con resultados nos motivó a incluir el análisis de registros de pequeños sismos obtenidos en las estaciones del SGC. Del periodo 2012-2018 se seleccionaron 12 eventos registrados en las estaciones CHI, VIL y ROSC, 15 registros en total (Figura 1 y Tabla 3). Los criterios para la selección fueron que el trayecto sismo estación cruzara o se acercara a la Sabana de Bogotá y que la relación señal/ruido fuera mayor a 3.

Tabla 1. Estaciones del SGC cuyos registros de ruido sísmico fueron analizados

Estación	Latitud N [°]	Longitud W [°]	Altitud [m]	Tipo	Sensor
BOG	4.641	74.080	2584	Aceleración	Episensor
CVER	4.521	74.074	3604	Banda ancha	CMG40T
ICBF	4.672	74.091	2583	Banda ancha	CMG40T
ROSC	4.845	74.321	3015	Banda intermedia	CMG3ESP
ROSCH	4.845	74.321	3015	Aceleración	CMG5TD
TABC	5.011	74.204	3500	Periodo corto	L4C-3D

Tabla 2. Análisis de registros de ruido sísmico en las estaciones del Servicio Geológico Colombiano. Para cada par de estaciones se indica la distancia entre ellas y el número de ventanas analizadas.

Pareja de estaciones	Distancia entre estaciones [km]	Número de ventanas analizadas
BOG-ICBF	3.621	2851
BOG-CVER	13.304	1548
CVER-ICBF	16.810	1575
ROSCH-TABC	22.548	1462
ICBF-ROSCH	31.872	1461
BOG-ROSCH	35.071	1458
ICBF-TABC	39.685	1575
BOG-TABC	43.265	1486
CVER-ROSCH	45.201	1472
CVER-TABC	56.237	1576

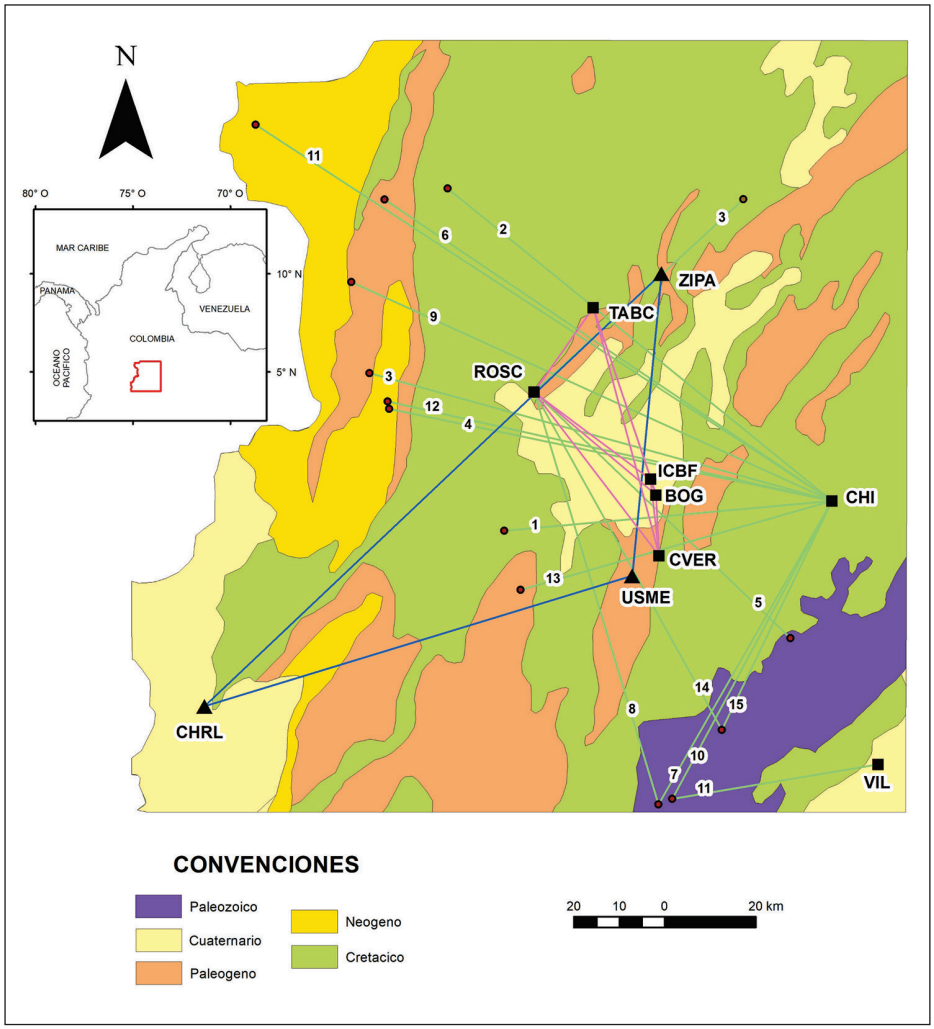

Figura 1. La figura insertada indica la localización del área representada en la figura principal, la cual muestra el mapa geológico simplificado de la zona de estudio. La Sabana de Bogotá corresponde al área de sedimentos cuaternarios en el centro del mapa. Las estaciones BOG e ICBF están localizadas en la ciudad de Bogotá. Los cuadros negros indican las estaciones del SGC, mientras que los triángulos muestran la ubicación de las estaciones de la RSSB. Los círculos rojos muestran los epicentros de los eventos utilizados y los números permiten identificar los datos de los eventos en la Tabla 1. [Modificado de Gómez *et al.* (2019).]

Tabla 3. Datos de los 15 registros analizados en este trabajo correspondientes a 12 eventos. La distancia corresponde a la distancia epicentral para la estación indicada.

Reg	Fecha	Hora UTC	Lat. N [°]	Lon. W [°]	H [km]	ML	Dist. [km]	Estación de registro	Azimuth
1	18/05/2013	13:18:40	4.57	74.38	0	3.0	72.2	CHI	73.4
2	14/07/2013	15:40:54	5.25	74.49	3.2	3.2	108.2	CHI	128.5
3	05/10/2013	8:56:12	4.88	74.65	14.3	2.7	105.3	CHI	105.3
4	27/12/2013	9:00:58	4.81	74.61	2	3.0	99.2	CHI	101.6
5	27/01/2014	10:37:57	4.36	73.81	0	2.9	77.9	ROSC	313.9
6	14/05/2014	3:33.56	5.23	74.62	9.2	2.8	118.2	CHI	123.8
7	17/08/2014	13:46:00	4.03	74.08	4.1	3.4	76.5	CHI	29.8
8	17/08/2014	13:46:00	4.03	74.08	4.1	3.4	94.3	ROSC	342.8
9	14/11/2015	1:59:17	5.06	74.68	12.5	3.6	115.8	CHI	114.3
10	01/03/2016	2:05:46	4.04	74.05	0	3.0	74.0	CHI	208.2
11	01/03/2016	2:05:46	4.04	74.05	0	3.0	40.1	VIL	78.5
12	25/08/2016	10:54.21	4.83	74.61	2.4	3.2	99.9	CHI	102.5
13	21/01/2017	6:34:06	4.45	74.35	25.4	3.8	71.1	CHI	74.0
14	17/02/2018	22:20:14	4.18	73.95	0.1	3.1	55.4	CHI	26.1
15	17/02/2018	22:20:14	4.18	73.95	0.1	3.1	84.6	ROSC	150.8

Método de análisis

El procesamiento de registros de sismos para estimar velocidades de grupo para cada trayectoria fuente-estación es sencillo. La velocidad de grupo de los trenes de ondas Rayleigh de los componentes verticales se obtiene simplemente al observar el tiempo de llegada de los máximos de la envolvente de la traza filtrada en distintas bandas de frecuencias (técnica de filtrado múltiple, Dziewonski *et al.*, 1969), tal como lo muestran, por ejemplo, Mokhtar *et al.* (2001). El caso del ruido sísmico requiere un análisis adicional. El ruido sísmico o vibración ambiental es la vibración permanente de cualquier punto de la superficie terrestre generada por causas naturales (oleaje en las costas, tormentas, sismos lejanos) o artificiales (maquinaria, vehículos, tránsito de personas). La enorme cantidad de fuentes que genera esa vibración y su continua variación tanto en tiempo como en espacio dan por resultado un campo de ondas estacionario e isotrópico que se aproxima a un campo difuso: no hay un modo de propagación dominante y la contribución de cada modo de propagación es independiente del tiempo y de la posición (Hennino *et al.*, 2001). Muchos artículos han mostrado argumentos, pruebas y demostraciones que muestran la estrecha relación entre la correlación cruzada en el dominio del tiempo de un campo difuso y la función de Green del medio entre los dos puntos de observación (e.g., Weaver y Lobkis 2001; Snieder 2004; Wapenaar 2004; Roux *et al.* 2005; Sabra *et al.* 2005a; Weaver y Lobkis, 2005). La función de Green contiene toda la información necesaria para calcular la propagación de todas las ondas posibles entre los dos puntos de observación (Aki y Richards, 1980).

Consideremos el cálculo de la correlación cruzada en el dominio del tiempo entre las trazas de ruido sísmico registrado en dos posiciones distintas, r_1 y r_2. Sabra *et al.* (2005b) escriben esa correlación cruzada como

$$C_{ij}(\tau) = \int_0^T v_i(r_1,t)v_j(r_2,t+\tau)\,dt$$

en donde t es el tiempo, $v_i(r_1, t)$ y $v_j(r_2, t)$ son dos ventanas de registro de ruido sísmico en las posiciones r_1 y r_2, T es el periodo de observación y C_{ij} es la correlación cruzada calculada entre las dos trazas en función de τ, el tiempo de retraso. Se puede demostrar que, con la hipótesis de que el ruido sísmico está generado por una distribución uniforme de fuentes (i.e., el campo de ruido sísmico es un campo difuso), el promedio de la correlación cruzada del ruido sísmico observado en dos puntos converge en el largo plazo a una función proporcional a la función de Green entre esos dos puntos

$$\frac{d<C_{ij}>}{dt} \approx -G_{ij}(r_1,r_2;t) + G_{ji}(r_2,r_1;-t)$$

en donde los términos en el miembro derecho de la ecuación son las funciones de Green entre las dos posiciones de registro. G_{ij} es la función de Green correspondiente a las señales que se propagan del receptor 1 al receptor 2 y que presentan un tiempo de retraso positivo, mientras que G_{ji} es la función de Green correspondiente a las señales que se propagan del receptor 2 al receptor 1 y que presentan un tiempo de retraso negativo. Los paréntesis triangulares indican promedio temporal. Aunque la función de Green incluye información de todos los modos posibles de propagación entre los dos sitios, resultados experimentales han mostrado que las ondas superficiales son el componente más estable y el que es reconstruido con mayor fidelidad en los promedios de las correlaciones cruzadas (Chávez-García y Rodríguez, 2007). Al pasar de propagación en 3D para ondas de cuerpo a propagación en 2D para ondas superficiales eliminamos un grado de libertad lo que hace a las ondas superficiales más estables en un medio heterogéneo. En este trabajo analizamos únicamente los componentes verticales, lo que permite asegurar que las ondas superficiales son ondas de Rayleigh. Se ha observado que se requiere promediar la correlación cruzada durante un tiempo suficientemente largo y que la distribución de las fuentes de ruido sísmico sea homogénea espacialmente para estimar la función de Green a partir de correlaciones de ruido sísmico (Lobkis y Weaver, 2001; Roux *et al.*, 2004). La superposición de resultados para muchas ventanas de tiempo permite que las señales coherentes se refuercen mientras el ruido incoherente se cancela (Sabra *et al.*, 2005c). La primera opción para realizar esa superposición es simplemente apilar la correlación cruzada obtenida para cada ventana en una suma global. Por supuesto, es necesario normalizar las amplitudes de esa correlación para que el peso de cada ventana promediada en el apilamiento sea homogéneo. Este procedimiento es lineal. Una segunda posibilidad para superponer los resultados de las ventanas individuales de correlación cruzada fue propuesta por Schimmel *et al.* (2011). La idea es promediar las distintas ventanas de correlación cruzada aplicando un peso que privilegie las señales que presentan mayor coherencia y atenúe las contribuciones que no son coherentes. Este algoritmo es no lineal. Los resultados se calcularon utilizando tanto el apilamiento lineal como el no lineal. Finalmente, estimamos curvas de dispersión de velocidad de grupo a partir de las correlaciones cruzadas promedio utilizando nuevamente la técnica de filtrado múltiple.

Resultados

El análisis de nuestros resultados se basa en los siguientes principios e hipótesis. Debido a que hemos procesado componentes verticales podemos estar seguros que las ondas superficiales que identifiquemos corresponden a ondas Rayleigh. Para estas ondas, cuando la velocidad de propa-

gación es invariante con la frecuencia la velocidad de fase (c) es igual a la velocidad de grupo (U), $c=U=V_R$. En estos casos, la velocidad de propagación de las ondas de Rayleigh, V_R, se puede escribir como $V_R=0.92V_S$ para sólidos de Poisson (el coeficiente de Poisson es igual a 0.25), en donde V_S es la velocidad de propagación de ondas de cortante, y la longitud de las ondas Rayleigh es $\lambda=V_R\,T$ en donde T es el periodo. Finalmente, dadas las limitaciones en la cantidad de resultados, discutimos nuestras observaciones en términos del modelo de un estrato sobre un semiespacio siguiendo el estudio paramétrico de la forma de las curvas de dispersión de velocidad de grupo presentado en Mooney y Bolt (1966).

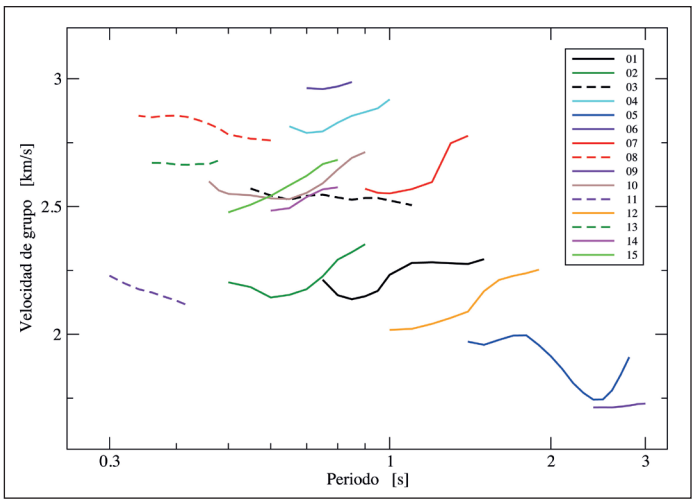

Figura 2. Curvas de dispersión de velocidad de grupo obtenidas del análisis de los 15 registros de sismos pequeños seleccionados (Tabla 1).

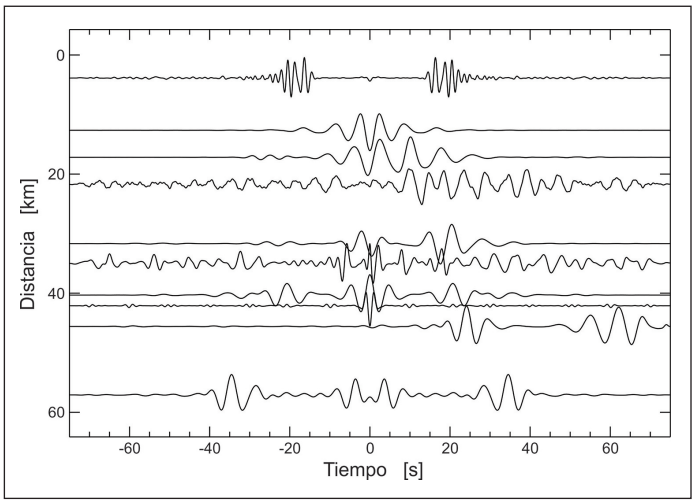

Figura 3. Correlaciones cruzadas promedio para los 10 pares de estaciones del SGC analizados. La amplitud de las trazas ha sido normalizada. Cada correlación cruzada se grafica a la correspondiente distancia entre estaciones y las trazas han sido filtradas con un filtro pasabandas de Butterworth de 4 polos con frecuencias de corte de 0.1 y 0.7 Hz. Se observa un pulso de ondas Rayleigh de baja frecuencia en casi todas las trazas.

Consideremos primero los resultados obtenidos para los registros de sismos pequeños obtenidos a distancias entre 40 y 118 km. La Figura 2 muestra las curvas de dispersión de velocidad de grupo estimadas a partir de esos registros. Todas las curvas muestran valores elevados de velocidad de grupo, mayores a 1.7 km/s (correspondiente al registro 9). El rango de frecuencias para el cual se estimaron velocidades varía de 0.3 a 3 s de periodo, pero cada registro permite estimar velocidades en un rango pequeño de periodos. Más aun, la banda de periodos de los resultados no se superpone para los 15 registros con excepción del pequeño intervalo entre 0.7 y 0.8 s de periodo, lo que dificulta analizar las curvas conjuntamente. Las longitudes de onda pueden estimarse burdamente en el rango entre 0.6 y 5.2 km. Los resultados no muestran una variación espacial acorde con la distribución de trayectorias. Algunas trayectorias cercanas muestran disparidad en las estimaciones de velocidad de grupo (e.g., 12 y 14), mientras que otras indican resultados cercanos (e.g., 7 y 10). Una única trayectoria (número 5) presenta una forma cercana a la esperada para un modelo sencillo de un estrato sobre un semiespacio. Si se interpreta este resultado en términos de este modelo, para una velocidad del estrato de 2 km/s, se puede estimar un espesor del estrato del orden de 2.1 km. Claramente todas las curvas de dispersión estimadas a partir de registros de sismos corresponden a ondas de Rayleigh que se propagan por una estructura profunda y no permiten estimar valores de velocidades de propagación para los estratos más superficiales, aquellos asociados a los efectos de sitio.

La Figura 3 muestra las trazas promedio obtenidas de la correlación cruzada de ruido sísmico en los 10 pares de estaciones del SGC analizados. Las trazas han sido filtradas con un filtro pasa bandas con frecuencias de corte de 0.1 y 0.7 Hz (1.4 y 10 s de periodo) y cada traza está graficada a la distancia entre el correspondiente par de estaciones. La amplitud ha sido normalizada con el máximo de cada traza y en cada caso se eligió la superposición causal/acausal que daba mejores resultados. Observamos en la mayoría de las trazas una señal que muestra una velocidad alrededor de 1.8 km/s, que interpretamos como el modo fundamental de ondas Rayleigh en ese medio. Es conspicuo que la primera traza (pareja BOG-ICBF, distancia de 3.6 km) muestra un pulso a un tiempo de retraso mayor, incompatible con las demás estaciones, con una velocidad menor a 200 m/s. A pesar de que el resultado para este par de estaciones se obtuvo de promediar 2,851 ventanas de una hora, la traza final sin filtrar (Figura 4a) no muestra un pulso claro de ondas Rayleigh. La Figura 4b muestra la misma traza filtrada en la banda de frecuencias usada en la Figura 3, 0.1 y 0.7 Hz, mientras que la Figura 4c presenta la traza de la Figura 4a filtrada en la banda de frecuencia entre 1.1 y 3.5 Hz. Las líneas rojas en las Figuras 4b y 4c corresponden a los envolventes de esas

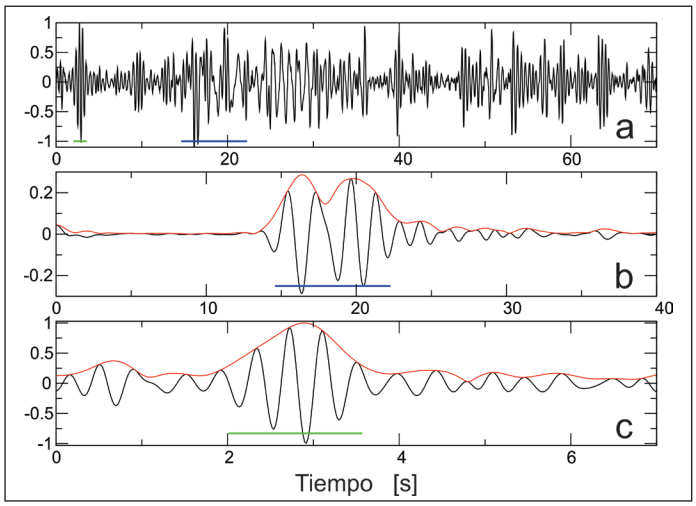

Figura 4. (a) Correlación cruzada final elegida para la pareja de estaciones BOG-ICBF, a una distancia de 3.621 km. Se muestran solo tiempos de retraso positivos para la traza sin filtrar. (b) Traza mostrada en (a) después de filtrarla con un filtro pasabandas de Butterworth de 4 polos con frecuencias de corte de 0.1 y 0.7 Hz. (c) Traza mostrada en (a) después de filtrarla con un filtro pasabandas de Butterworth de 4 polos con frecuencias de corte de 1.1 y 3.5 Hz. En las figuras (b) y (c), la línea roja muestra el envolvente de la traza y la línea azul (b) y verde (c) indican el intervalo de tiempo en el que se presentan los máximos del envolvente. Esos intervalos se muestran en (a) con los mismos colores, lo que permite identificar a que parte de la traza original corresponden.

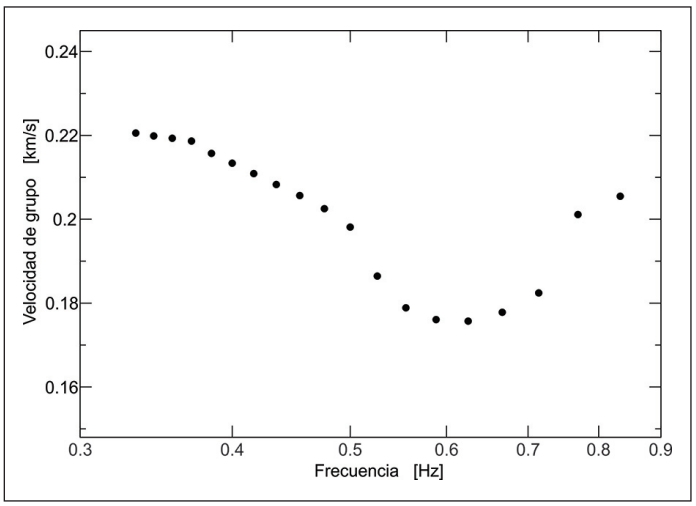

Figura 5. Curva de dispersión calculada para el pulso de ondas Rayleigh que se observa en la traza mostrada en la Figura 4b.

trazas. En la Figura 4b ese envolvente es máximo en 16.4 y 19.8 s, lo que corresponde a velocidades de grupo entre 221 y 183 m/s (Figura 5). En la Figura 4c el máximo del envolvente ocurre en 2.9 s, correspondiente a una velocidad de grupo de 1.2 km/s, congruente con la velocidad de grupo para la mayoría de las trazas de la Figura 3. Los resultados para la pareja BOG-ICBF son diferentes a las demás parejas analizadas debido a la pequeña distancia entre estaciones (3.6 km) que permite determinar dos pulsos de ondas Rayleigh. Uno de ellos, cuya curva de dispersión se muestra en la Figura 5 y que corresponde al pulso mostrado en la Figura 4b, no corresponde al medio muestreado por las otras parejas de estaciones: la dispersión de velocidad de grupo para esta señal sugiere un modelo de una capa de 163 m de espesor con velocidad de ondas de cortante de 220 m/s. El segundo pulso con una frecuencia más alta, mostrado en la Figura 4c, se propaga con velocidad de grupo que sí es compatible con la de las otras parejas de estaciones.

La Figura 6 presenta los valores de velocidad de grupo determinados para el ruido sísmico analizado en las 10 parejas de estaciones del SGC. Dos parejas de estaciones (BOG-CVER y BOG-ICBF) muestran resultados en una banda de frecuencia distinta a las demás, entre 0.2 y 0.6 s (1.6 y 5 Hz). La estimación de la pareja BOG-CVER indica un valor muy alto para la velocidad de grupo, mayor a 2.5 km/s, mientras que la pareja BOG-ICBF muestra los valores más pequeños (1.25 km/s, como se indicó arriba, este par de estaciones es

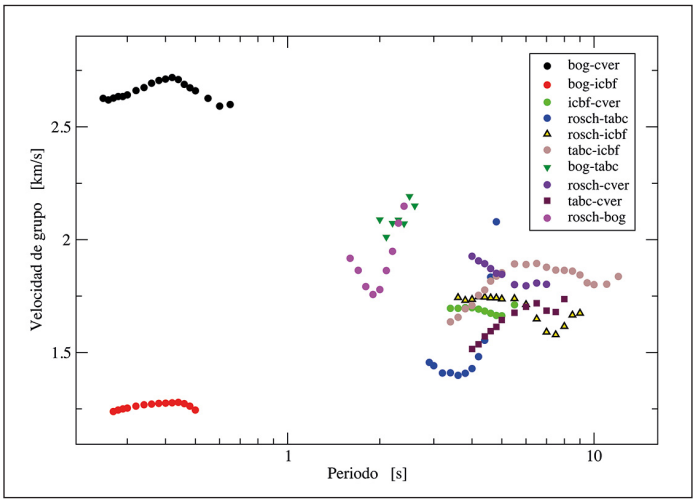

Figura 6. Curvas de dispersión de velocidad de grupo obtenidas del análisis de ruido sísmico registrado en las estaciones del SGC. Por razones de escala no se incluye la curva mostrada en la Figura 5.

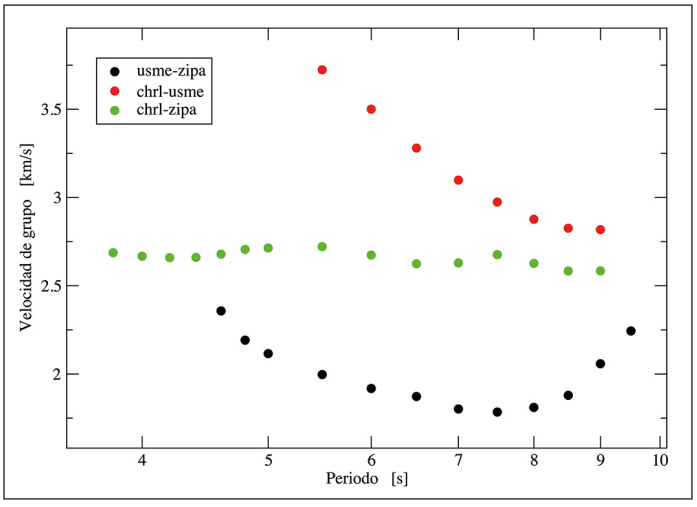

Figura 7. Curvas de dispersión de velocidad de grupo calculadas del análisis de filtrado múltiple para las trazas de correlación cruzada promedio obtenidas para tres pares de estaciones de la RSSB.

singular debido a la pequeña distancia entre estaciones). Las 8 parejas restantes permiten estimar velocidades de grupo entre 2 y 10 s de periodo (0.1 y 0.5 Hz) con estimaciones de velocidad de grupo en el rango de 1.5 a 2 km/s. Algunas de las parejas muestran formas de dispersión cercanas a lo esperado para un espacio estratificado (e.g., ROSCH-BOG, ROSCH-TABC) pero el rango de periodos es muy reducido y las curvas están incompletas, lo que no permite invertir esas curvas de dispersión.

Sólo fue posible calcular correlaciones cruzadas entre tres pares de estaciones de la RSSB. Las curvas de dispersión estimadas se muestran en la Figura 7. El rango de frecuencias es muy similar para los tres casos pero los valores de velocidad de grupo y la forma de las curvas difieren considerablemente. Las velocidades más altas se observan para la pareja CHRL-USME. La forma de esta curva coincide parcialmente con lo esperado para una capa sobre un semiespacio (Mooney y Bolt, 1966). Sin embargo, la velocidad de ondas de cortante que tendría el estrato sería mayor que la velocidad de grupo observada en el periodo mínimo (3.7 km/s), lo que corresponde forzosamente a un basamento rocoso. La longitud de onda a 9 s de periodo sería mayor a 20 km. Esta pareja probablemente muestrea el basamento rocoso profundo, que puede corresponder a las rocas del Cretácico que predominan a lo largo de esa trayectoria. El resultado para la pareja CHRL-ZIPA presenta una velocidad de grupo casi constante en el rango de periodos de 3.8 a 9 s. La velocidad de ondas Rayleigh corresponde con una velocidad de ondas de cortante de 2.9 km/s. Finalmente, la pareja USME-ZIPA muestra una velocidad de grupo con un mínimo en 7.5 s de periodo. La velocidad de grupo varía entre 1.8 y 2.4 km/s. Un posible estrato correspondiente a esa curva de dispersión tendría un espesor del orden de 8.5 km. La pequeña distancia entre las dos estaciones y el que la mayor parte de la trayectoria atraviese la Sabana de Bogotá sugiere que esta pareja de estaciones permite observar el basamento bajo los sedimentos superficiales de la Sabana.

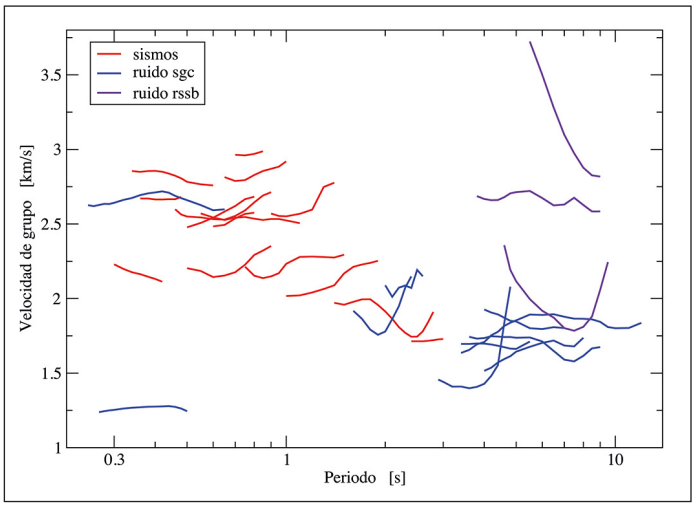

Figura 8. Compilación de todas las curvas de dispersión de velocidad de grupo obtenidas durante este proyecto, con excepción de la curva mostrada en la Figura 5, excluida por razones de escala.

Discusión y conclusiones

A pesar de las limitaciones en la cantidad y calidad de los datos analizados, nuestros resultados permiten algunas observaciones significativas. El par de estaciones situado a la menor distancia (BOG-ICBF) permitió observar valores de velocidad de ondas de cortante pequeños en los primeros cientos de m de profundidad (la longitud de onda asociada al pulso mostrado en la Figura 4b está comprendida entre 200 y 600 m). Si comparamos la forma de la curva mostrada en la Figura 5 con la esperada para el modo fundamental de ondas Rayleigh sobre un semiespacio (Mooney y Bolt, 1966) podemos estimar que corresponde a una capa de 163 m de espesor con velocidad de ondas de cortante de 220 m/s, valores que presentan un buen acuerdo con los resultados de Pulido *et al.* (2020). Los resultados obtenidos para la pareja BOG-ICBF contrastan con los valores observados para los demás pares de estaciones, implicando un contraste de impedancias significativo entre sedimentos profundos y superficiales. La amplificación del movimiento del terreno durante sismos está estrechamente ligada a la magnitud de ese contraste, por lo que nuestros resultados sugieren que los efectos de sitio son importantes en la Sabana de Bogotá.

La Figura 8 muestra todas las velocidades de grupo estimadas en este trabajo (con excepción de la curva de dispersión mostrada en la Figura 5). Salvo dos excepciones, los resultados del ruido sísmico registrado en estaciones del SGC proporcionan valores de velocidad de grupo a periodos mayores (frecuencias menores) que los resultados del análisis de sismos. Esto es esperado pues el espectro de Fourier de velocidad de la energía asociada a sismos pequeños como los analizados ocurre a frecuencias relativamente altas. Los sismos proporcionan valores de velocidad de grupo en el rango de frecuencias de 0.3 a 3 s de periodo. En todos los casos, cada trayectoria proporciona valores de velocidad de grupo en un rango pequeño de frecuencias y la variación de velocidad de grupo con la frecuencia es pequeña, con pocas excepciones. La menor velocidad de grupo en la Figura 8 corresponde al ruido sísmico analizado para la pareja BOG-ICBF, pero aun esta estimación indica velocidades de grupo mayores a 1.2 km/s. Dado que las distintas curvas se observan en rangos de periodos pequeños y dado que esos rangos no coinciden para las distintas estimaciones, no es posible calcular una inversión tomográfica a partir de estos resultados.

En términos generales se observa una disminución de la velocidad de grupo estimada desde valores alrededor de 2.5 km/s entre 0.3 y 1 s de periodo a valores alrededor de 1.7 km/s entre 4 y 10 s de periodo. Los resultados para la RSSB son dispares a pesar que el rango de periodos es simi-

lar en los tres casos. A pesar de ello, es claro que las ondas de Rayleigh muestreadas por esta red corresponden a capas profundas. No se observa semejanza entre resultados, aun cuando las trayectorias sean cercanas, lo que sugiere que la incertidumbre asociada a nuestras estimaciones de velocidad de grupo es elevada. Esto no es inesperado debido a que las ondas Rayleigh concentran su energía en los estratos situados sobre el basamento rocoso, y en éste presentan amplitudes que decaen exponencialmente al aumentar la profundidad, o sea al aumentar el periodo de la curva de dispersión. Esto hace que sea difícil estimar la velocidad de propagación del basamento rocoso en cualquier caso (Chávez-García, 2007).

Los resultados obtenidos muestran el impacto de la geología en los valores promedio de dispersión de velocidad de grupo en la región de la Sabana de Bogotá. Observamos diferencias significativas en velocidad de grupo entre trayectorias contenidas en los sedimentos cuaternarios que cubren la Sabana de Bogotá y aquellas que incluyen parte de su trayecto por rocas del Cretácico. Una única trayectoria permite muestrear la velocidad de ondas de cortante en los sedimentos superficiales de la sabana. El contraste de impedancia estimado entre esos sedimentos y los estratos subyacentes sugiere que la amplificación del movimiento sísmico excede un factor de 10.

La deficiente cantidad y calidad de los datos limitaron los alcances de este trabajo. El número de trayectorias para las cuales se estimaron curvas de dispersión fue muy pequeño y los rangos de frecuencia de los resultados no coincidieron para las distintas fuentes de datos, lo que obstaculizó las comparaciones entre trayectorias e hizo imposible el considerar el cálculo de una tomografía. A pesar de esas limitaciones, estos resultados contribuyen a mostrar la relevancia de los efectos de sitio en la Sabana de Bogotá y la necesidad de tomarlos en cuenta para estimar el movimiento durante sismos futuros en esta zona.

Agradecimientos

Este trabajo fue apoyado por la Vicerrectoría de Investigación de la Universidad del Quindío bajo la clave 934. Los autores agradecen al Servicio Geológico Colombiano (SGC) el acceso a los datos sismológicos y acelerográficos de las redes que opera, y al Dr. Carlos Vargas Jiménez del Departamento de Geofísica de la Universidad Nacional de Colombia, sede Bogotá, por el acceso a los datos registrados por la Red Sísmica de la Sabana de Bogotá. Los autores agradecen a Sheila Sánchez Ramírez, su apoyo en el análisis de los registros de ruido sísmico obtenidos en las estaciones del SGC. Finalmente, los autores agradecen el apoyo recibido de la Coordinación de la Investigación Científica de la Universidad Nacional Autónoma de México para las actividades de intercambio académico entre la UNAM y la Universidad del Quindío que permitieron realizar este trabajo.

Referencias

Aki, K., Richards, P.G., 1980, Quantitative seismology. Theory and methods. Freeman, 2 vols, San Francisco.

Bensen, G.D., Ritzwoller, M.H., Barmin, M.P., Levshin, A.L., Lin, F., Moschetti, M.P., Shapiro, N.M., Yang, Y., 2007, Processing seismic ambient noise data to obtain reliable broad-band surface wave dispersion measurements. *Geophys. J. Int.*, 169, 1239-1260. **https://doi.org/10.1111/j.1365-246X.2007.03374.x**

Chávez-García, F.J., Pedotti, G., Hatzfeld, D., Bard, P.Y., 1990, An experimental study of site effects near Thessaloniki (Northern Greece). *Bull. Seism. Soc. Am.*, 80, 784-806. **https://doi.org/10.1785/BSSA0800040784**

Chávez-García, F.J., 2007, Site effects: from observation and modelling to accounting for them in building codes, en K.D. Pitilakis (ed.) Earthquake Geotechnical Engineering, 4th International Conference of Earthquake Geotechnical Engineering–Invited lectures, vol. 6 de la serie Geotechnical, Geological and Earthquake Engineering, Springer, 53-72.

Chávez-García F.J., Rodríguez, M., 2007, The correlation of microtremors: empirical limits and relations between results in frequency and time domain. *Geophys. J. Int.*, 171, 657-664. **https://doi.org/10.1111/j.1365-246X.2007.03529.x**

Dimaté C, Rivera, L., Cisternas, A., 2005, Re-visiting large historical earthquakes in the Colombian Eastern Cordillera. *J. Seismol.*, 9, 1-22. **https://doi.org/10.1007/s10950-005-1413-2**

Dziewonski, A., Bloch, S., Landisman, M., 1969, A technique for the analysis of transient seismic signals. *Bull. Seism. Soc. Am.*, 59, 427-444. **https://doi.org/10.1785/BSSA0590010427**

FOPAE, 2010, Zonificación de la Respuesta Sísmica de Bogotá para el Diseño Sismo Resistente de Edificaciones, FOPAE, 152 pp.

Gómez J., Shobbenhaus, C., Montes, N.E., 2019, Geological map of South America 2019, scale 1:5,000,000, Commission for the Geological Map of the World (CGMW), Servicio Geológico Colombiano y Servicio Geológico de Brasil, Paris. **https://www2.sgc.gov.co/MGC/Paginas/gmsa5M2019.aspx**

Helmens, K.F., van der Hammen, T., 1994, The Pliocene and Quaternary of the high plain of Bogotá (Colombia): a history of tectonic uplift, basin development and climatic change. *Quat. Int.*, 21, 41-61. **https://doi.org/10.1016/1040-6182(94)90020-5**

Hennino, R., Trégourès, N., Shapiro, N.M., Margerin, L., Campillo, M., van Tiggelen, B.A., Weaver, R.L., 2001, Observation of equipartition of seismic waves. *Phys. Rev. Lett.*, 86, 3447-3450. **https://doi.org/10.1103/PhysRevLett.86.3447**

Herrmann, R.B., 1985, Computer programs in seismology, University of Saint Louis, St. Louis, MO.

INGEOMINAS, 1997, Proyecto Microzonificación sísmica Santafé de Bogotá, INGEOMINAS, 124 pp.

Lobkis, O.I., Weaver, R.L., 2001, On the emergence of the Green's function in the correlation of a diffuse field. *J. Acoust. Soc. Am.,* 110, 3011-3017. **https://doi.org/10.1121/1.1417528**

Mokhtar, T.A., Ammon, C.J., Herrmann, R.B., Ghalib, H.A.A., 2001, Surface Wave Velocities Across Arabia. *Pure appl. geophys*., 158, 1425-1444. **https://link.springer.com/article/10.1007/PL00001228**

Mooney, H.M., Bolt, B.A., 1966, Dispersive characteristics of the first three Rayleigh modes for a single surface layer. *Bull. Seism. Soc. Am.*, 56, 43-67. **https://doi.org/10.1785/BSSA0560010043**

Park, S., Elrick, S., 1998, Predictions of shear-wave velicities in Southern California using surface geology. *Bull. Seism. Soc. Am.*, 88, 677-685. **https://doi.org/10.1785/BSSA0880030677**

Pulido, N., García, H., Montejo, J., Senna, S., 2020, Long period ground motion simulations at the Bogota basin, Colombia, based on a 3D velocity model of the basin from dense microtremors arrays measurements, gravity and geological data, en 17th World Conf. on Earthq. Engrg., 1f-0031, Sendai, Japón, 13 a 18 septiembre.

Roux, P., Kuperman, W.A., el grupo NPAL, 2004, Extracting coherent wave fronts from acoustic ambient noise in the ocean. *J. Acoust. Soc. Am.,* 116, 1995-2003. **https://doi.org/10.1121/1.1797754**

Roux, P., Sabra, K.G., Kuperman, W.A., 2005, Ambient noise correlations in free space: theoretical approach. *J. Acoust. Soc. Am.,* 117, 79-84. **https://doi.org/10.1121/1.1830673**

Sabra, K.G., Roux, P., Kuperman, W.A., 2005a, Arrival-time structure of the time-averaged ambient noise cross-correlation function in an oceanic guide. *J. Acoust. Soc. Am.,* 117, 164-174. **https://doi.org/10.1121/1.1835507**

Sabra, K.G., Gerstoft, P., Roux, P., Kuperman, W.A., Fehler, M.C., 2005b, Extracting time-domain Green's function estimates from ambient seismic noise. Geophys. Res. Lett., 32, L03310. **https://doi.org/10.1029/2004GL021862**

Sabra, K.G., Roux, P., Kuperman, W.A., 2005c, Emergence rate of the time-domain Green's function from the ambient noise cross-correlation function. *J. Acoust. Soc. Am.,* 118, 3524–3531. **https://doi.org/10.1121/1.2109059**

Schimmel, M., Stutzmann, E., Gallart, J., 2011, Using instantaneous phase coherence for signal extraction from ambient noise data at a local to a global scale. *Geophys. J. Int.*, 184, 494-506. **https://doi.org/10.1111/j.1365-246X.2010.04856.x**

Snieder, R., 2004, Extracting the Green's function from the correlation of coda waves: a derivation based on stationary phase. *Phys. Rev. E*, 69, 046610. **https://doi.org/10.1103/PhysRevE.69.046610**

Stein, S., Wysession, M., 2003, An introduction to Seismology, earthquakes, and Earth structure. Blackwell, Reino Unido.

Torres V., Vandenberghe, J., Hooghiemstra, H., 2005, An environmental reconstruction of the sediment infill of the Bogota basin (Colombia) during the last 3 million years from abiotic and biotic proxies, *Palaeogeography, Palaeoclimatology, Palaeoecology*, 226, 127-148. **https://doi.org/10.1016/j.palaeo.2005.05.005**

Wapenaar, K., 2004, Retrieving the elastodynamic Gree's function of an arbitrary inhomoheneous medium by cross correlation. *Phys. Rev. Lett.*, 93, 254301. **https://doi.org/10.1103/PhysRevLett.93.254301**

Weaver, R.L. Lobkis, O.I., 2001, Ultrasonics without a source: thermal fluctuation correlations at MHz. *Phys. Rev. Lett.*, 87, 134301. **https://doi.org/10.1103/PhysRevLett.87.134301**

Weaver, R.L. Lobkis, O.I., 2005, The mean and variance of diffuse field correlations in finite bodies. *J. Acoust. Soc. Am.,* 118, 3447-3456. **https://doi.org/10.1121/1.2109307**

Geofísica Internacional (2023) **62-1**: 429 - 444

Developing and calibrating a new approach of geoelectrical acquisition for detecting active tectonic features, Northern Dead Sea Fault System, Syria

Jamal Asfahani*[1] and Walid Al-Fares[1]

Abstract

A new interpretative geoelectrical approach is adapted by using vertical electrical sounding (*VES*) technique with geoelectrical Schlumberger configuration and mainly Pichgin and Habibuleave technique. The proposed approach is aimed at getting interpretative reliable apparent resistivity measured data for the shallow penetration depths of approximately less than 10 meters. The adapted *VES* configuration with its specific *small AB/2* spacings not exceeding 50m is used to characterize the structures of Recent and Quaternary deposits in the Al-Ghab depression region. *The AB/2* spacings used in this Schlumberger array are 1, 1.3, 1.68, 2.18, 2.82, 3.66, 4.74, 6.15, 7.97, 10.33, 13.38, 17.35, 22.49, 29.15, 37.78 and 48.87 meter. The features of those structures are considered as good records for indicating active and neo-tectonic events. The interpretations of the eight acquired *VES* data carried out along a studied profile located above an excavation at Mehanbel area with an integrated enhanced Pichgin and Habibuleave approach provide quantitative calibrated results that are in exact concordance with the real positions of the Recent and Quaternary structures. The obtained results encourage consequently to apply this adapted configuration elsewhere to detect the outcropped or blind active faults and other structural features in the Recent and Quaternary deposits. The privileged locations of the trenching, used for studying the new active tectonic features will be decided at the light of the established subsurface geoelectrical imaging obtained by this integrated approach along different profiles in a given study area.

Key Words: Active tectonic, *VES* sounding, Trenching, Dead Sea Fault System, Al-Ghab, Syria.

Resumen

Se adopta un nuevo enfoque geoeléctrico interpretativo mediante el uso de la técnica de sondeo eléctrico vertical (*VES*) con una configuración geoeléctrica de Schlumberger y la técnica de Pichgin y Habibuleave principalmente. El enfoque propuesto busca obtener datos interpretativos de resistividad aparente confiables para profundidades someras, de menos de unos 10 metros. La configuración *VES* se adapta usando espaciamientos *AB/2* pequeños, que no superan 50 m y se utiliza para caracterizar estructuras de depósitos Recientes y Cuaternarios en la región de la depresión de Al-Ghab. Los espaciados *AB/2* usados en esa disposición de Schlumberger son 1, 1.3, 1.68, 2.18, 2.82, 3.66, 4.74, 6.15, 7.97, 10.33, 13.38, 17.35, 22.49, 29.15, 37.78 y 48.87 metros. Con esas estructuras se obtienen buenos registros para identificar eventos activos y neotectónicos. Las interpretaciones de los ocho grupos de datos *VES* adquiridos a lo largo de un perfil ubicado sobre una excavación en el área de Mehanbel, con un enfoque integrado mejorado de Pichgin y Habibuleave, brindan resultados cuantitativos calibrados que están en concordancia exacta con las posiciones reales de las estructuras Reciente y Cuaternaria. Por lo tanto, los resultados obtenidos alientan a aplicar esta configuración adaptada en otros lugares para detectar fallas activas afloradas o ciegas y otras características estructurales en depósitos Recientes y Cuaternarios. Las mejores ubicaciones para la excavación de zanjas utilizadas para estudiar las nuevas características tectónicas activas se decidirán a la luz de las imágenes geoeléctricas del subsuelo obtenidas por este enfoque integrado, a lo largo de diferentes perfiles en un área de estudio determinada.

Palabras clave: Tectónica activa, Sondeos eléctricos verticales (SEV), excavación, Sistema de fallas del Mar Muerto, Al-Ghab, Siria.

Received: June 2, 2022; October 25, 2022; published on-line: January 1, 2023.

Editorial responsibility: Anonymous

* Corresponding author: jasfahani@aec.org.sy
[1] Geology Department, Atomic Energy Commission of Syria, P.O.Box. 6091, Damascus- Syria. E-mail: cscientific3@aec.org.sy

https://doi.org/10.22201/igeof.2954436xe.2023.62.1.1450

Introduction

A valuable record of neo-tectonic events over the last ten thousands years can be provided by the Quaternary and recent sediments, composed mainly of soft sediments with a cover of top soil. They highly very susceptible to the weathering and could be removed away in a little time. This might completely or partially efface the traces of surface expressions, recording and containing the recent tectonic events. Those important records could be also erased by increasing the levels of the human activities since the dawn of civilization that range from the land cultivation to the construction of giant dams. The main challenge in the active tectonic studies is the need to improve our knowledge about the morphotectonic mapping of active surface tectonic features with subsurface data to receive convincible and well-preserved *3D* images of Quaternary structures.

Generally, the different geophysical techniques that we are using today have been designed to satisfy the increasing demand of society for new resources of mineral, water, and energy. Those different resources are usually localized at big depths. In the neo-tectonic research, in contrast, the scope is reversed. Several high-resolution seismic reflection surveys have been recently realized in the last few years to explain the geometry and timing of the Quaternary fault (Williams *et al.*, 1995; Palmer *et al.*, 1997; Van Arsdale *et al.*, 1998). Ground-penetrating radar (*GPR*) has been applied in the San Francisco Bay region by Cai *et al.*, (1996) for very shallow investigations. *GPR* technique bridges the gap between the high-resolution seismic investigations and the trenching. Although this *GPR* provides with a high-resolution image down to 4 m to 6 m, but the high number of *GPR* reflections and diffractions resulting from the sedimentological complexity and the tectonic features does not usually allow an unambiguous location of a fault (Demanet *et al.*, 2001). However, subsequent interpretation of *GPR* measurements can provide us with valuable information on the deformation patterns close to the fault if it is delineated by using other geophysical techniques such the one described in this paper.

Shields *et al.*, (1998) used different geophysical methods (magnetic, electromagnetic and seismic reflection methods) to delineate the fault zone extension of the Parhump Valley near the Nevada and California border. Demanet *et al.*, (2001) practiced also various geophysical techniques (electrical profiling, electromagnetic, *GPR*, seismic reflection) along the Bree fault scarp (western border of the Roer Graben) to image and locate the active fault zone over a depth ranging from a few decimeters to a few tens of meters. The interpretations of those geophysical data were already used as a useful reconnaissance tool to smartly guide the direct investigations by trenching.

Several other examples of the use of multiple geophysical methods for investigating the shallow neo-tectonic features are provided by (Parrales *et al.*, 2003, Caputo *et al.*, 2003; Chwatel *et al.*, 2005, Caputo *et al.*; 2007; Fazzito *et al.*, 2009; Piscitelli *et al.*, 2009). Massoud *et al.*, (2009) recently used the directional azimuthal resistivity sounding and joint inversion of vertical electrical sounding and time electromagnetic (*VES*-TEM) measurements to delineate the shallow subsurface structures near Lake Qaroun, El Fayoum, Egypt.

The water resources in Khanasser valley region in northern Syria have been successfully estimated by applying methodological researches, based mainly on the direct geoelectrical current (*DC*) methods, particularly *VES* soundings (Asfahani, 2007a and b, 2010). Those researches applied the enhanced Pichgin and Habibullaev technique (1985) to the acquired *VES* data to delineate the different subsurface structures and to outline fresh, brackish, and saline water accumulations. Asfahani and Radwan (2007) improved and update the efficiency of the Pichgin-Habibullaev technique to make it easily applicable in the pronounced topography areas. Accordingly, shallow and young subsurface structures were defined and characterized to be the essential basis for establishing the tectonic origin of Khanaser Valley as a graben, which developed during Pliocene-Quaternary and accompanied with cycled volcanisms.

Several geoelectrical techniques were recently applied by Asfahani *et al.*, (2010) in Al-Lijj area, northwestern Syria to determine the subsurface tectonic structure of Kastoon dam in Al-Ghab depression. Al-Fares and Asfahani, (2018) applied also electrical resistivity tomography (*ERT*) and *VES* sounding techniques with different interpretative approaches to determine the subsurface tectonic conditions of Abu Baara dam in Northern Syria. Asfahani (2018) has proposed and developed a combined geoelectrical array having a good resolution in comparing with the traditional Schlumberger configuration for characterizing the shallow and deep structures. Asfahani and Al-Fares, (2021) proposed a new fractal technique to interpret the *VES* data along a given profile, and to explain the evolution scenarios of different basalt structures along the studied profile.

The above encouraging geoelectrical results motivate us to apply the geoelectrical techniques and the enhanced Pichgin and Habibullaev interpretation approach in the active tectonic domain in Al-Ghab pull apart, that has been developed at the northern segments of the Dead Sea fault System in Syria.

A shallow and deep penetrating Schlumberger configuration is accordingly designed to characterize structurally the shallow Quaternary and recent sediments, as well as the deeper structures located at depths of <250m in Al-Ghab depression region, where five profiles (*Pr-1, Pr-2, Pr-3, Pr-4,* and *Pr-5*) were studied and analyzed (Asfahani, 2010-a).

A suitable shallow-depth penetrating configuration in the order of less than 10 m is designed herein aiming at

disclose the shallow-depth deformation and structures in Quaternary sediments, which are good indications of active and neo-tectonic events.

The reliability of this designed configuration and its efficacy in detecting deformations in Quaternary sediments is tested on a selected site in Mhambel area along the *N-S* Al-Ghab eastern faults.

The main objectives of this paper are therefore the followings:

- Testing the validity and the merit of the shallow-depth penetrating *VES* configuration purposely-developed for detecting active tectonic deformation in the Recent and Quaternary sediments at a test area located on active faults.
- Acquiring the geoelectric responses of different morphotectonic features in the Recent and Quaternary sediments mapped in the selected test area, through the employment of the adapted *VES* configuration with the proposed integrated geoelectrical approach.
- Applying the acquired geoelectrical response on other areas to predict their neo-tectonic activity.

Geology and tectonic setting

Figure. 1 indicates the Syrian map, in which the study area of Al-Ghab and the main tectonic features in Syria are shown.

Geology (Stratigraphy)

Rock types outcropped at the eastern side of Al- Ghab pull apat and Rouj depression (Figure 2) consist of 150 m thick 5-7° eastward dipping Cenomanian–Turonian sequence composed of massive, moderately and thin-bedded limestone and dolomites with marl and limestones intercalations.

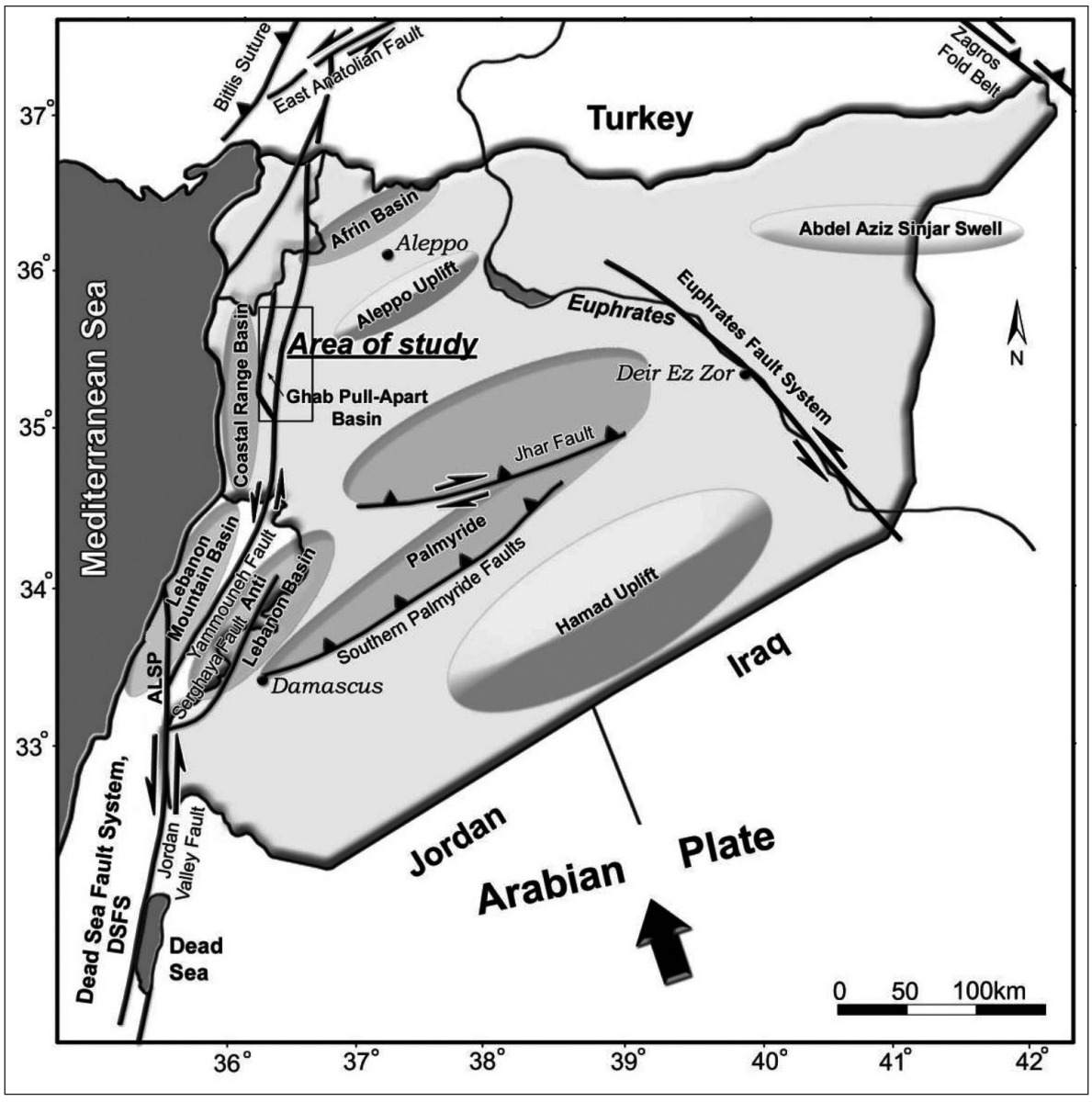

Figure 1. Study of Al-Ghab area and the main tectonic features in Syria.

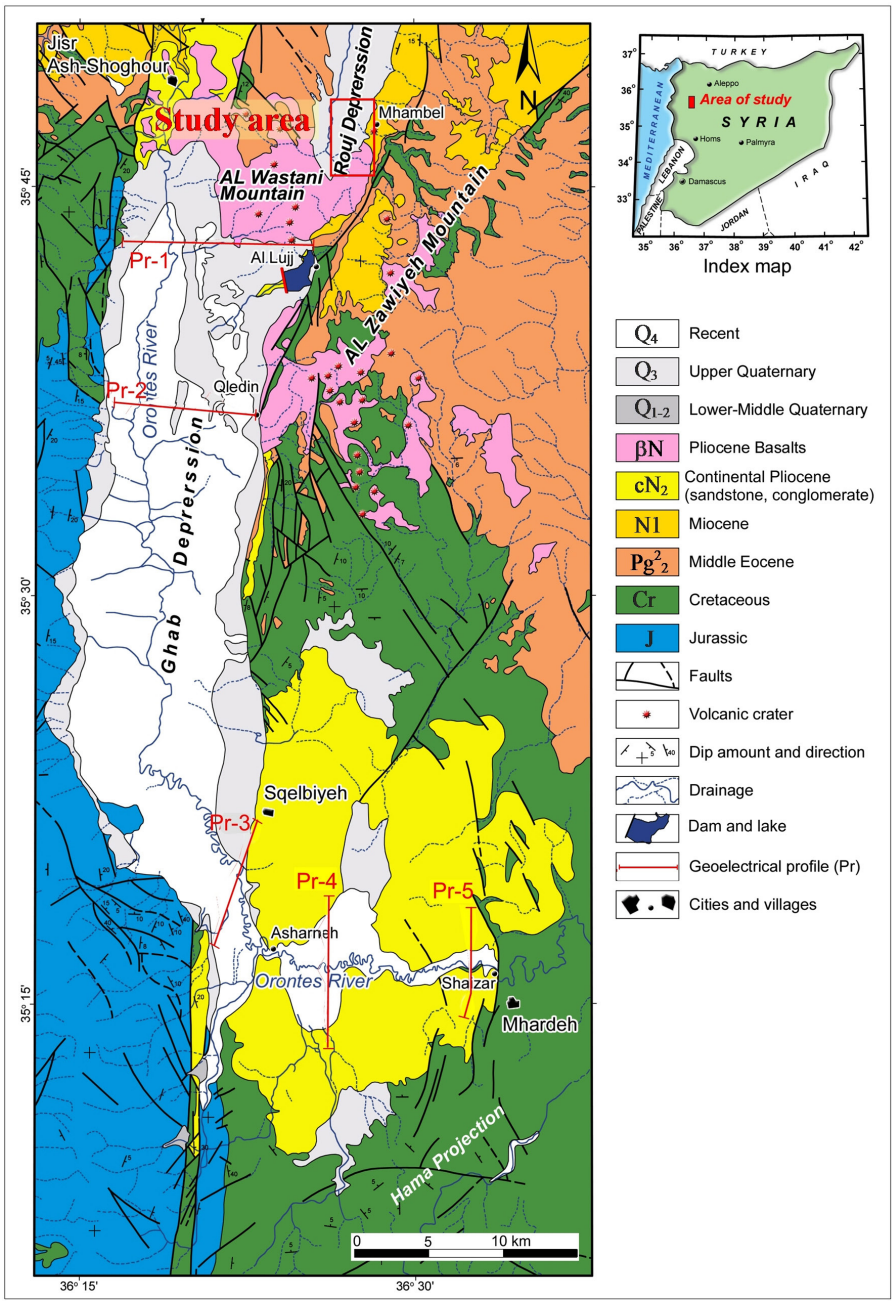

Figure 2. Geology of the Mhembel study area.

The sequence is overlain by 40-45 m thick Campanian marl and limestone and discordantly overlain by 180-225 m thick Middle Eocene (*Pg2*) limestone with white clayey chalk like limestone interbeds.

The overlying Tortonian (N_1: Lower Miocene) sediments composed of 410 m basal conglomerate changes with sandstone interfingering, followed by a 150 m thick series of grey calcareous sandstone interbedded with siltstone, marl and conglomerate, ending with arenaceous marl with sandstone lenses and bands outcropped near Mhambel. The series, decreasing in thickness southward, is replaced by coarse pebble and boulder conglomerate indicating its closeness to the Tortonian sea coastline.

Large Pliocene basaltic rocks (βN_2), extruded from eight highly eroded, oval shaped volcanic cones (1km×100m), cover the northern end of Al-Ghab pull apart and the sourthern parts of the Rouj depression with a maximum thickness of 60m. They are composed of dolerite, anamesite, hyalobasalt and teschenite, nepheline basanite, analcite anamesites, alternated lavas, tuffs and slags. Their surface is slightly inclined southward and buried under Upper Quaternary and Recent sediments. Lower-Middle Quaternary (Q_1) is represented in northeastern Al-Ghab by shell limestone and Proluvial poorly sorted conglomerates and pebble beds is encountered. Upper Quaternary (Q_3) alluvium is composed of flinty pebbles and brown loams, while the proluvium and

the deluvium is composed of clays, loams, sandstone with clay fragments and gravels mixtures. Lacustrine sediments form a low terrace-like platform, 0.5-3 m high composed of yellow silty sands and dark brown nearly black loam 1m.

The lacustrine, deluvial and proluvial sediments bear flint implements, ceramics and polished basaltic items considered as old as 6000-8000 years. The Recent (Q_4) sediments are alluvial pebbles beds, loam and Orontes River sandy loam. Recent lacustrine sandy clay passing upwards into black peaty loams (3-4 m thick) fill the centre of Al-Ghab depression, (Ponikarov, 1966).

Tectonic

From the tectonic point of view, the research test areas are located at the western rims of Al Zawiyeh Mountain, bounded by Al- Ghab eastern faults, which are segments of the *N-S* Dead Sea Fault System (*DSFS*) extension in Syria. Two structures were developed along Al-Ghab Eastern faults; the Al-Ghab pull apart and the Rouj depression. Brew *et al.*, (2001a, 2001b) consider the 15×25 km *N-S* elongated Al-Ghab pull apart, as a deep structure opened in response to a left-step in the *DSFS* during Pliocene to Holocene. The northern tips of Al-Ghab eastern faults deviates at Qlaidin village from their *N-S* regional strike marking the initiation of the wedge-shaped Rouj depression elongated in the *NNE* (Figure 2). Many workers such as Quennell, 1984; Beydoun, 1999 believe that the Dead Sea fault system is an active major sinistral transform plate boundary between the sinistraly northward moving Arabian plate relative to the African Plate (Levantine subplate) developing complex deformational structures oriented according to the stress field prevailed along it, e.g. Dead Sea, Tiberias lake, Bekaa Valley and Al-Ghab Depression. A double-episode lateral movement was suggested by Quennell (1959) along the *DSFS*, expressed by a Miocene 60 to 65 km slip on the system's southern segment (Freund *et al.*, 1970; Quennell, 1984), and Post-Miocene 20 to 25 km sinistral motion on the system's both southern and northern segments. The second phase was accompanied by additional 20 km suggested to be accommodated by shortening of the adjacent Palmyride fold and thrust belt (Chaimov *et al.*, 1990), making the total post-Miocene slip amounts 40-45, and 105 km on the northern system and southern segments respectively.

The geomorphological evidences for Pliocene-Recent tectonic activity (Hricko, 1988; Darkal *et al.*, 1990; Radwan *et al.*, 1994a, 1994b; Devyatkin *et al.*, 1997), the seismic evidences of Ambraseys and Jackson (1998), paleoseismic evidences of Serghaya fault and Al-Ghab pull apart, (Meghraoui *et al.*, 2003; Gomez *et al.*, 2001, 2003); and *GPS* measurements (McClusky and Balassanian, 2000; Gomez *et al.*, 2006), collectively gave additional support to the system current activity, denying Butler *et al.*, (1997), argument that the northern segments of the *DSFS* have been inactive since Miocene.

Geomorphotectonic features at Mhambel calibration site

The calibration test site lies 1.3 km at the south of the village of Mhembel at the N-NE faulting zone, which deviates from the *N-S* regional trend of the northern segments of the *DSFS*, and bounds the eastern edges of the Rouj valley (Figure 2).

The rocks, at the area of Mhambel village, are mainly Middle Eocene (*Pg2*) limestone interbeded by thin beds of clayey and chalky limestone and overlain by Tortonian sandstone, calcareous sandstone, siltstone, marl and arenaceous marl lenses. These rocks outcrop at both sides of the valley of Sakhreen transient stream, which crosses through Mhambel village. The mapped Pliocene basaltic rocks (βN_2) in Sakhreen valley and south of Mhambel were extruded from a heavily eroded volcanic cone located in the mentioned valley. Most of Mhambel village is built from materials composed of loam, clay, sandstone and gravels mixtures that are incised by the current running water of Sakhreen stream. Deluvial and proluvial sediments of varied thickness cover sporadically the slopes south of the village.

An excavation at 1.3 km south of Mhambel, disclosed a N-NE normal fault cuts through the fan sediment and the underlying Tortonian rose sandstone (Figure 3).

This site was selected as an ideal fault exposure for calibrating the adapted shallow *VES* geolectrical configuration developed with its *small AB/2* spacings not exceeding 50 m to detect and trace the active faulting due to the followings:

1. The presence of a clear cut vertical displacement of an active normal fault,
2. The limitation of the fault exposure area,

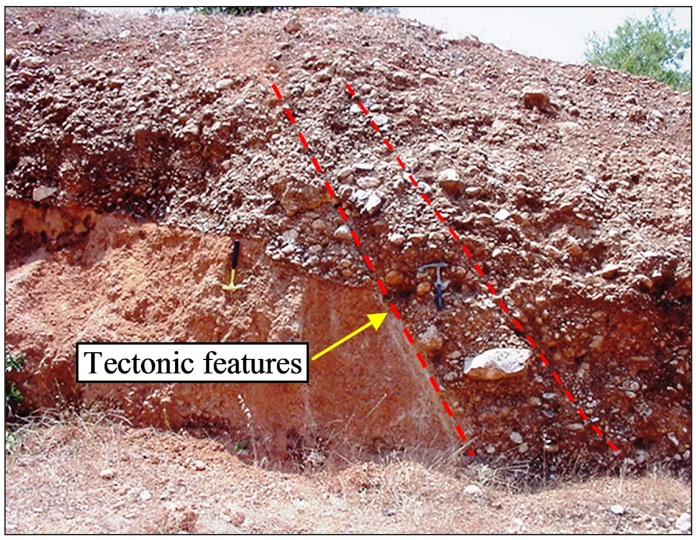

Figure 3. The calibrated site of Mhambel study area.

3. The striking lithological difference between the soft Tortonian marly sandstone and the rough Recent fan gravel sediments,
4. The negligible effects of weathering processes on the active faulting zone. Accordingly, the break in the moderate slope upon it, the developed colluvial wedge and fault scarp were well preserved,
5. The youngness of this representative active faulting, makes the use of this developed *VES* configuration applicable and promising in detecting blind active faults elsewhere.

Material

Vertical electrical sounding (VES) Technique

The apparent resistivity measurements were carried out using the Indian resistivity meter model ACR-1. Eight vertical electrical sounding were carried in the location study area. The traditional Schlumberger configuration is adapted and used to acquire the apparent resistivity data by means of vertical electrical sounding (*VES*), with a half maximum current electrode spacing (*AB/2*) of 48.87 m and potential electrode spacing (*MN/2*) of 3 m.

The *specific AB/2* spacings used in this designed adapted *VES* array are 1, 1.3, 1.68, 2.18, 2.82, 3.66, 4.74, 6.15, 7.97, 10.33, 13.38, 17.35, 22.49, 29.15, 37.78 and 48.87 meter. The Resistance (R_a) was first recorded in the field, and converted later to apparent resistivity (ρ_a) for the Schlumberger array by the use of the following equation:

$$\rho_a = \frac{(AB/2)^2 - (MN/2)^2}{MN} * Ra \quad (1)$$

This equation was reduced to: $\rho_{a=} GRa$

$$G = \frac{(AB/2)^2 - (MN/2)^2}{MN} \quad (2)$$

where *G* is the geometric factor.

The field apparent resistivity curves were obtained by increasing the electrode spacing *AB/2* about a fixed point. Those vertical electrical sounding curves were thereafter plotted in the next stage for each of the survey locations, and smoothened to remove noisy signatures (Chakravarthi *et al.*, 2007; Ebong *et al.*, 2006). We use the curve matching technique with master curves for interpreting the field resistivity curves to determine an initial model including resistivities and thicknesses of the corresponding layers (initial approximate model) (Orellana and Mooney, 1966). The inversion WINRESIST software program is thereafter used to interpret the parameters of the approximate model to get the final optimum model, in which a goodness of fit between the field resistivity curve and the final theoretical regenerated curve was arrived (Zohdy, 1989; Zohdy and Bisdorf, 1989). This inversion procedure allows estimating the values of the true resistivity, depth and thickness of the subsurface after several iterations for each *VES* point.

Pichgin and Habibulaeve Technique

Pichgin and Habibulaeve (1985) have already developed a geoelectrical technique aimed at interpreting vertical electrical sounding (*VES*) points, measured and distributed along a given profile. This technique is considered as one of the best technical methods established for distinguishing tectonic fractured zones and dipping contacts. This *2D* interpretative technique allows also the determination of the direction and inclination of faults under a given geoelectrical profile, hence a *2D* subsurface tectonic image can be derived.

The basic of this technique can be described as follows:

When an electrical current passes through a contact of two outcropping formations of different resistivities $\rho 1$ and $\rho 2$, the injected electrical current boundary conditions at this contact will be explained according to Pichgin-Habibullaev technique as follows:

1. If the direction of the symmetrical electrode Schlumberger configuration of the four electrodes is perpendicular to this contact, and if the center point of the *VES* sounding is located just over a vertical contact between two formations of different resistivities $\rho 1$ and $\rho 2$, the apparent measured resistivity ρK is expressed in this case by the following equation:

$$\rho k = (\rho 1 + \rho 2)/2 \quad (3)$$

The measured *VES* resistivity is independent from *AB* and *MN* lengths.

If there are two vertical electrical soundings *VES*1, *VES*2, measured on both sides of a vertical contact (Figure 4), in such a case, all the geoelectrical profiling curves presented as a function of distance between the different *VES* points, for all the used *AB/2* will be intersected in only one point, located directly over this vertical contact (Figure 4). Every geoelectrical profiling clearly shows the apparent resistivity variations for a given *AB/2* (Figure 4).The vertical electrical soundings data for all the *VES* points distributed along a given profile are therefore transferred to be represented as horizontal multi-depths profiling curves for every given *AB/2*. The locations of vertical electrical soundings, realized on such a given profile are plotted on abscissa using a linear scale, while the corresponding apparent resistivities (ρk or $\rho' k$) for each given *AB/2* are plotted on the ordinate using a logarithmic scale. This resistivity is also independent from *AB* and *MN* lengths.

2. If the direction of the symmetrical electrode Schlumberger configuration of the four electrodes is parallel to such a contact, the apparent measured resistivity $\rho`K$ is expressed by the following equation:

$$\rho'k=2(\rho1*\rho2)/(\rho1+\rho2) \quad (4)$$

The intersection points of the horizontal geoelectrical curves represented for the different *AB/2* are called the non-homogeneity points (*PNH*) symbolized as (+). Those *PNH* are plotted on a *2D* (*x*, *y*) geological section. The depth (z) of each *PNH* is determined from to the following equation:

$$Z=[(AB/2)_i+(AB/2)_j]/2 \quad (5)$$

Where $(AB/2)_i$ and (*AB/2*)j are the half-spacings between the electrodes *A* and *B*, at which two horizontal curves are intersected.

A computer program developed by Asfahani and Radwan (2007) is used to determine the positions and locations of the *PNH*. Geological interpretations of the *PNH* could be achieved according to the Pichgin-Habibullaev technique, based on the following assumptions:

1. The presence of an inhomogeneous lithologic contact is decided when the *PNH* are distributed along oblique lines located at shallow depths.
2. A fractured zone is decided if *PNH* are arranged along oblique lines dipping at an angle exceeding 30° at depth.
3. An homogeneous lithology is decided if *PNH* are scattered randomly near the surface.
4. Certain geological structures, such as synclines, anticlines, or horizontally layered strata could be decided if *PNH* are arranged in regular forms.

The above four assumptions have been calibrated and verified through different field tests, particularly in Syria, including different lithologies and structural architecture (Asfahani and Mohamad, 2002; Asfahani, 2007a,b; Asfahani and Radwan, 2007; Asfahani *et al.*, 2010).

However, it is to mention that the basic original Pichgin and Habibullaev method, being developed only for smooth topography gives inaccurate and sometimes misleading tectonic interpretations in areas of rough topography (Pichgin and Habibuleav, 1985). Asfahani and Radwan, 2007 therefore modified and enhanced slightly this technique to attain a reliable subsurface tectonic interpretation, by taking into consideration the real absolute elevation of each measured *VES* point. Numerical values of the topography elevations of the *VES* points were incorporated in the processing software through purposely-developed mathematical formulas as

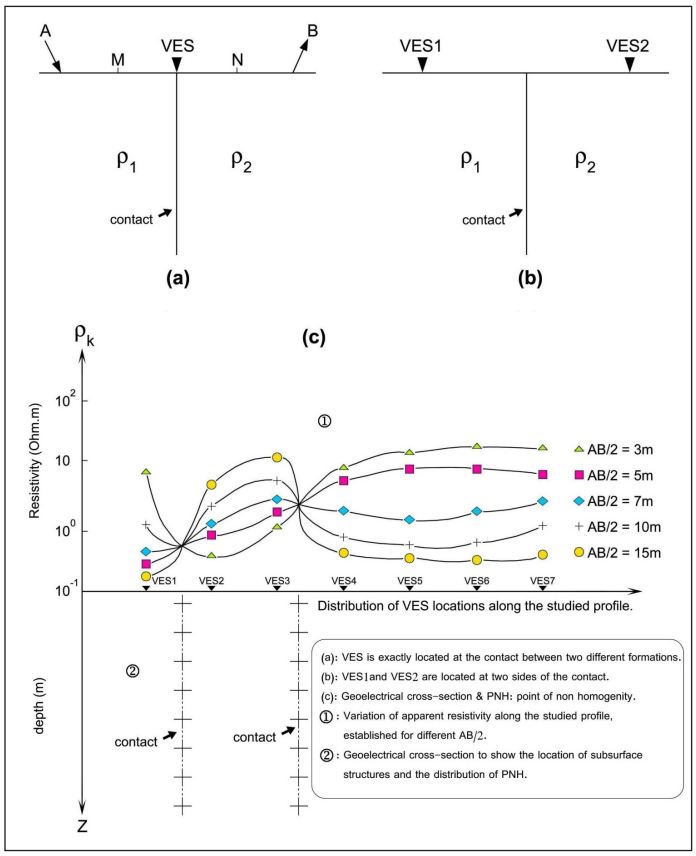

Figure 4. Principal of Pichgin and Habibulaeve technique (1985).

additional crucial factors to achieve enhanced Pichgin and Habibuleav profiles.

The mentioned development and enhancement was performed according to the four following successive steps (Asfahani and Radwan,2007):

1. Constructing a real topographic profile passing through *VES* station positions of a given *VES* profile, hence real absolute elevation of the *VES* station is considered.
2. For every pair of successive resistivity *VES*s, of *AB/2* spacing along a given profile, all intersections points are localized and projected on a real topographic profile constructed in step-1. In the original Pichgin and Habibullaev technique, all the intersection points are projected onto a zero reference level, assuming that all *VES* stations have the same elevation.
3. The intersection points, together with the topographic profile constructed in step-2, are projected onto the *X-Z* plane, to obtain (*PNH*), whose depths *Z* are similarly determined by using equation (5).

The location of (*PNH*) depths by using the enhanced method is more sophisticated and reliable in extrapolating the subsurface structures, where real and true elevation of the intersection *PNH* points is determined with reasonable accuracy.

Procedures of step-2 are repeated for all *AB/2* spacings, to localize all possible (*PNH*) in the *X-Z* plane.

A computer program was already developed to enable the performance of the aforesaid 4-steps enhancement through processing the *VES* resistivity input data, hence acquiring enhanced Pichgin and Habibuleav *VES* profiles, that could be interpreted according to the rules and conception previously discussed (Asfahani and Radwan, 2007). Thus the enhanced method became easily applicable in areas of hard topography and prominent relief, attaining real computer-aided topographic cross sections along *VES* profiles.

Asfahani and Mohammed, 2002 applied efficacy this technique for sulfur prospecting in North East of Syria. Asfahani and Radwan (2007), used this geoelectrical interpretative technique for solving different hydrogeological problems at Khanasser valley region, Northern Syria. Asfahani *et al.*, 2010 interpreted the geoelectrical *VES* data by using this technique for determining the subsurface tectonics and their impacts on the Qastoon Dam, Northwestern Syria. Asfahani, 2010-a used it for solving subsurface structural and mining phosphate problems in Al-Ghab area and Al-Sharquieh mine in Syria respectively. This enhanced Pichgin and Habibuleav technique has been widely applied in different research published works, and proven its efficacy and importance in several geological applications (Asfahani, 2011).

Al-Fares (2016) conducted a geoelectrical *VES* survey, in which he used Pichgin and Habibuleav pseudo-*2D* method to maximize the reliability of the *VES* data interpretation. The results indicated the presence of a local faulted anticline structure at the top of the Paleogene formation, underneath the basaltic outcrops where Deir El-Adas village is situated, Southern Syria. Al- Fares explained in his paper that appearance of this subsurface anticline structure has considerably complicated the local hydrogeological situation, and most likely led to the limitation of the groundwater recharge in the Deir El-Adas area. Al- Fares and Asfahani, 2018 used also this technique through an integrated geophysical approach in the dam domain to identify the potential leakage zones within the substructure bedrock close to the Abu Baara earth fill dam, located at the southern margins of Al- Ghab plain northwest of Syria.

Sirwa and Asfahani, 2019 applied enhanced Pichgen and Habibullaev (1985) method, and proven its clear important role in providing subsurface structures, and in detecting the exact position, dip and direction of faults and groundwater level at Erbil Dumpsite, West of Erbil City – Iraqi Kurdistan Region.

Previous research works

Geoelectrical methods were already applied in the Al-Ghab depression region to characterize the Recent and Quaternary structures. A slight modification on the Schlumberger configuration concerning the design of its spacings of *AB/2* was adapted to get reliable image on the shallow penetration depths (<50 m), (Asfahani, 2011). The application of the adapted configuration with the proposed interpretative geoelectrical approach on studying and analyzing five profiles shown in Figure 2 (*Pr-1, Pr-2, Pr-3, Pr-4,* and *Pr-5*) allowed to get the real resistivities and thicknesses of the mentioned shallow structures as shown in Table 1.

Profile #	Recent		Quaternary	
	Average ρ (Ω.m)	Average thickness (m)	Average ρ (Ω.m)	Average thickness (m)
Pr-1	44	1.6	12	29
Pr-2	34	1.2	25	10
Pr-3	25	6	20	17
Pr-4	40	3.5	18	27
Pr-5	22	2	34	9

The application of the enhanced Pichgin and Habibulaeve technique on the geoelectrical *VES* data distributed along those five profiles provided us with the shallow structures of the Recent and Quaternary deposits as shown in Figure 5.

The results obtained on those mentioned profiles provoke us to update again the Schlumberger configuration to get geoelectrical information about only the shallower depths of less than 10 m.

Results and Discussion

The adapted shallow *VES* configuration with the interpretative geoelectrical approach is applied in this research to calibrate and test its applicability and efficacy to be used for detecting the Recent and Quaternary structures, considered as good records for the active tectonic features. It is applied in this paper on the surface perpendicular to the fault plane exposure shown in Figure 3.

Figure (6) shows the eight field *VES* curves with the variations of the apparent resistivity as a function of the half current electrode spacing (*AB/2*), that were carried out along a profile of 45m long over the faulted slope shown in Figure 3. The log-log scale is used, where the *X* coordinate represent the half spacing *AB/2*, while the *Y* coordinate represent the field apparent resistivity.

Those eight field curves have similar shape and reflect a special lithological structure near to surface that will be more identified with the following qualitative and quantitative interpretations.

The *1D* quantitative interpretations of those *VES* soundings by the use of WINRESIST software of Velpen (2004) allows after several iterations to obtain the real model values of the true resistivity, depth and thickness of the subsurface

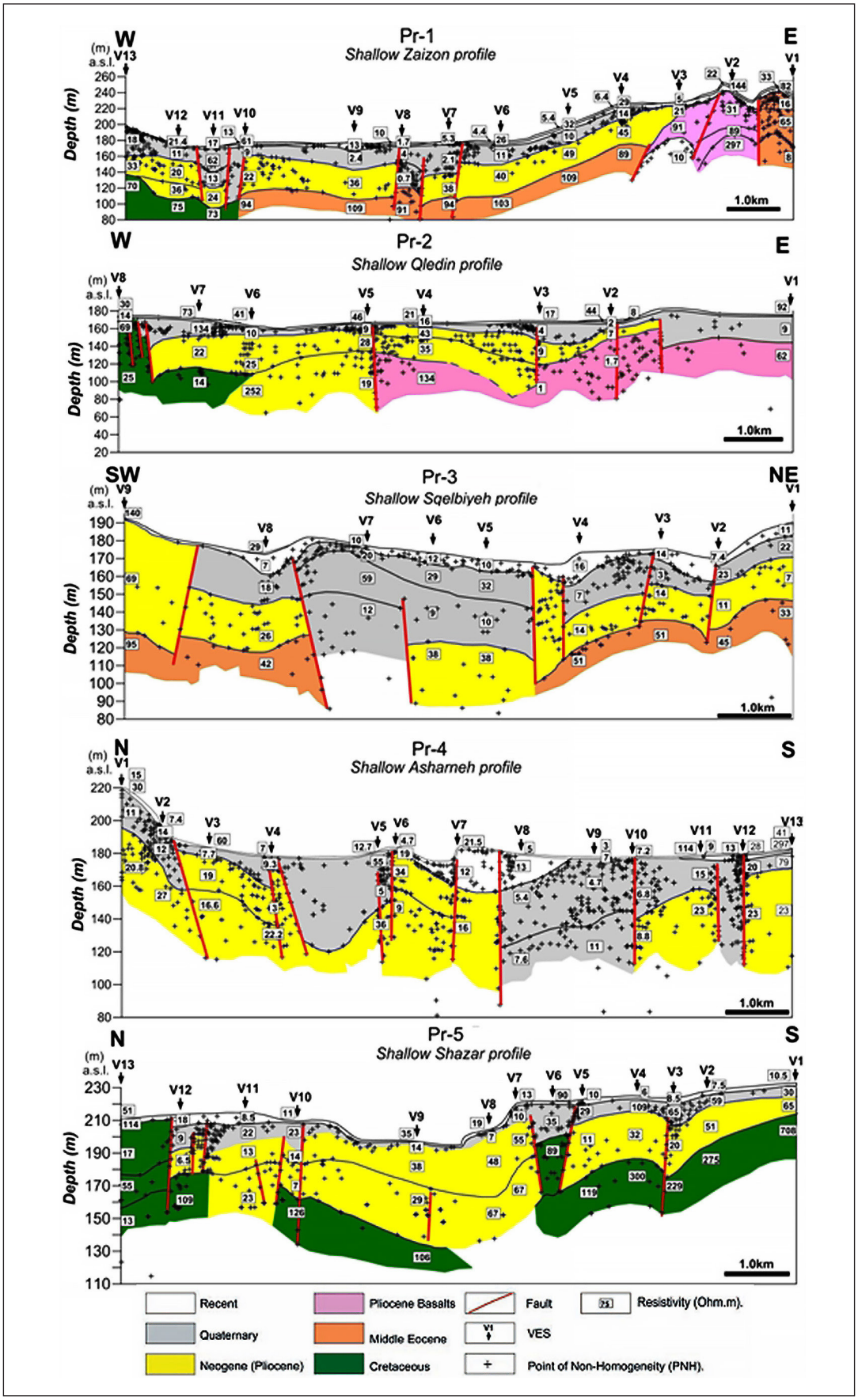

Figure 5. Recent and Quaternary structures obtained along *Pr-1, Pr-2, Pr-3, Pr-4,* and *Pr-5* profiles (Asfahani, J., 2010a).

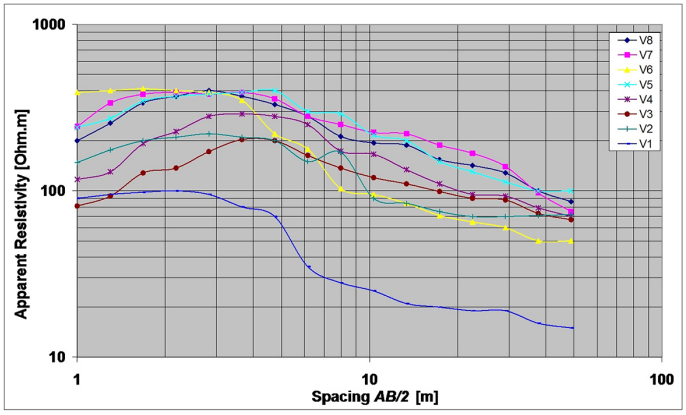

Figure 6. The field *VES* curves ($\rho a = f(AB/2)$) measured at eight locations in the study Mhembel area.

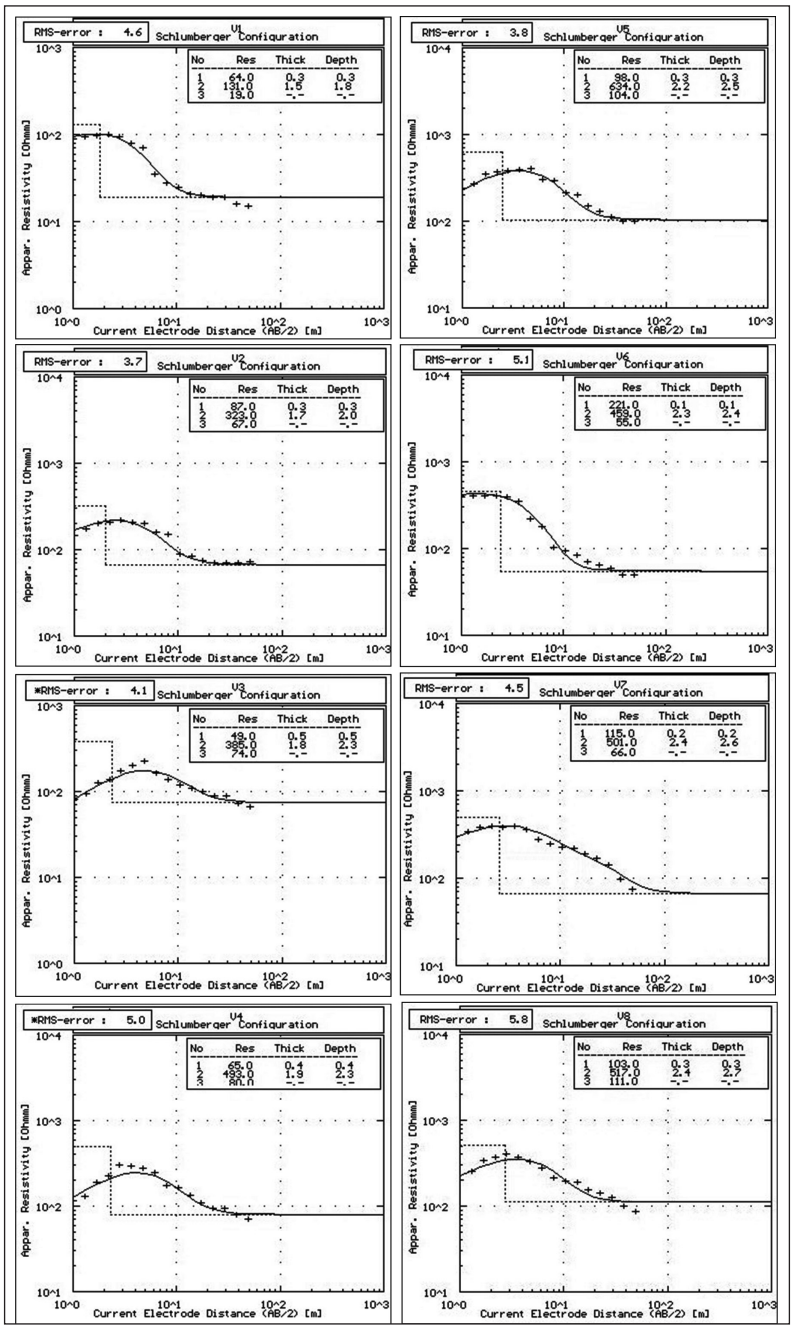

Figure 7. The inversion earth models of the eight *VES* in the study Mhembel area.

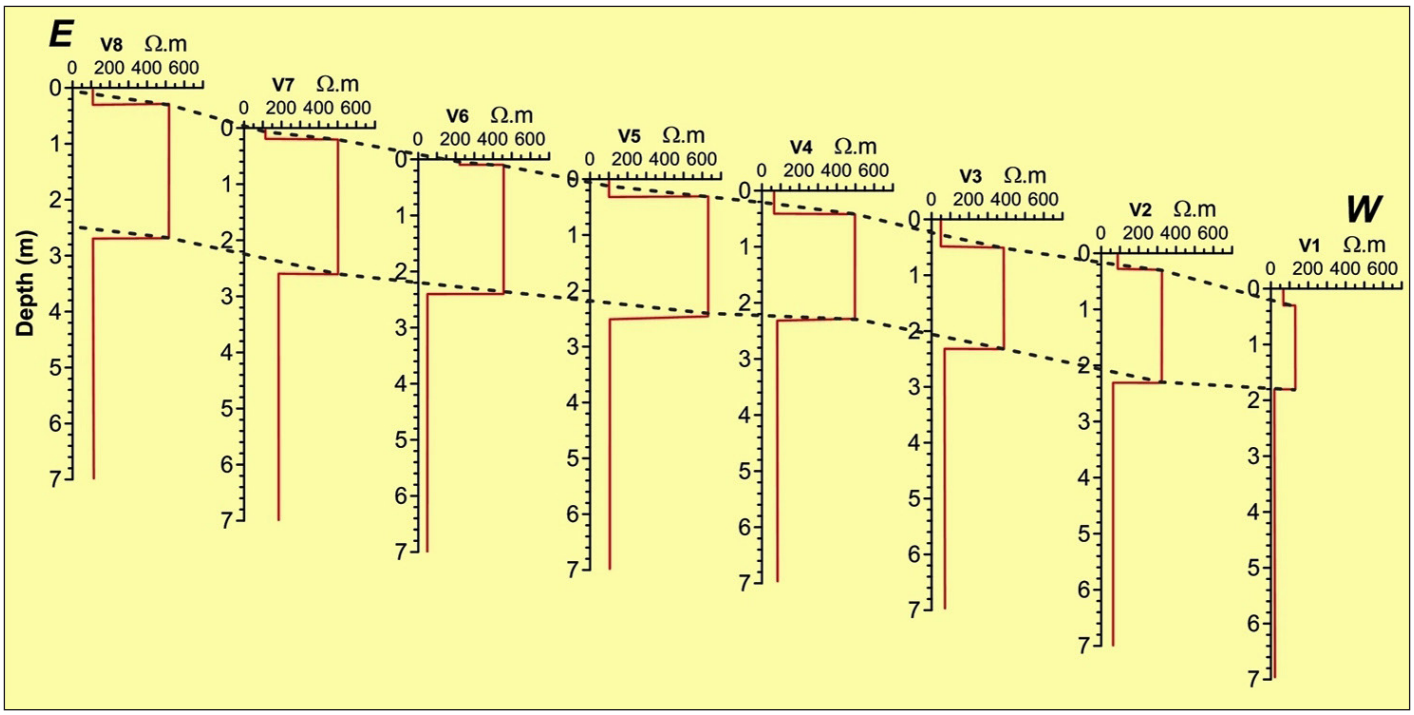

Figure 8. Two dimensional (*2D*) inversion resistivity-depth (R-D) model obtained by eight *VES* in the study Mhembel area.

Table 1. indicates that all the eight measured *VES* are interpreted by a model of three layers with a type curve.

VES points	Resistivity (Ω.m)			Thickness (m)			RMS (%)	Curve type
	ρ1	*ρ2*	*ρ3*	h_1	h_2	h_3		
V1	64	131	19	0.3	1.5	--	4.6	*K*
V2	87	323	67	0.3	1.7	--	3.7	*K*
V3	49	385	74	0.5	1.8	--	4.1	*K*
V4	65	493	80	0.4	1.9	--	5.0	*K*
V5	98	634	104	0.3	2.2	--	3.8	*K*
V6	221	459	55	0.1	2.3	--	5.1	*K*
V7	115	501	66	0.2	2.6	--	4.5	*K*
V8	103	517	111	0.3	2.4	--	5.8	*K*

layers for each *VES* point as shown in Figure 7 and 8, and Table 2. A model of three layers of *K* type of $\rho 1<\rho 2>\rho 3$ is adapted for those interpreted eight *VES*.

The thicknesses of the first top soil layer varies between a minimum of 0.1 m at *V6* location and 0.5 m at *V3* location. The resistivity of this layer varies between a minimum of 49 Ω.m at *V3* and 221 Ω.m at *V6*.

The thickness of the second layer varies between a minimum of 1.5 m at *V1* location and 2.6 m at *V7* location. The resistivity of this layer varies between a minimum of 131 Ω.m at *V1* and 634 Ω.m at *V5*. The resistivity of the third layer varies between a minimum of 19 Ω.m at *V1* and 111 Ω.m at *V8*.

Figure 9 shows the *2D* pseudo-section variations of the measured apparent resistivity as a function of *AB/2* along the studied *E-W* profile.

This *2D* qualitative interpretation proves that the adapted *VES* configuration with the proposed geoelectrical approach is highly sensitive to the surfacial layers structure located above 10 m, where its resolution diminishes considerably under 10 m depth.

The enhanced Pichgin and Habibuleav technique described above is used to interpret the eight measured *VES* soundings. The non homogeneity points (+) are obtained under the studied profile as shown in Figure 10.

The combination of the one dimensional (*1D*) results obtained by the quantitative interpretation of the eight *VES* soundings with the distribution of the non homegenity points allows to get the litho-structural two dimensional model (*2D*) along the studied *E-W* profile as shown in Figure 11.

The *2D* constructed model shows essentially well the resistivity variations of the distinguished top soil layer and

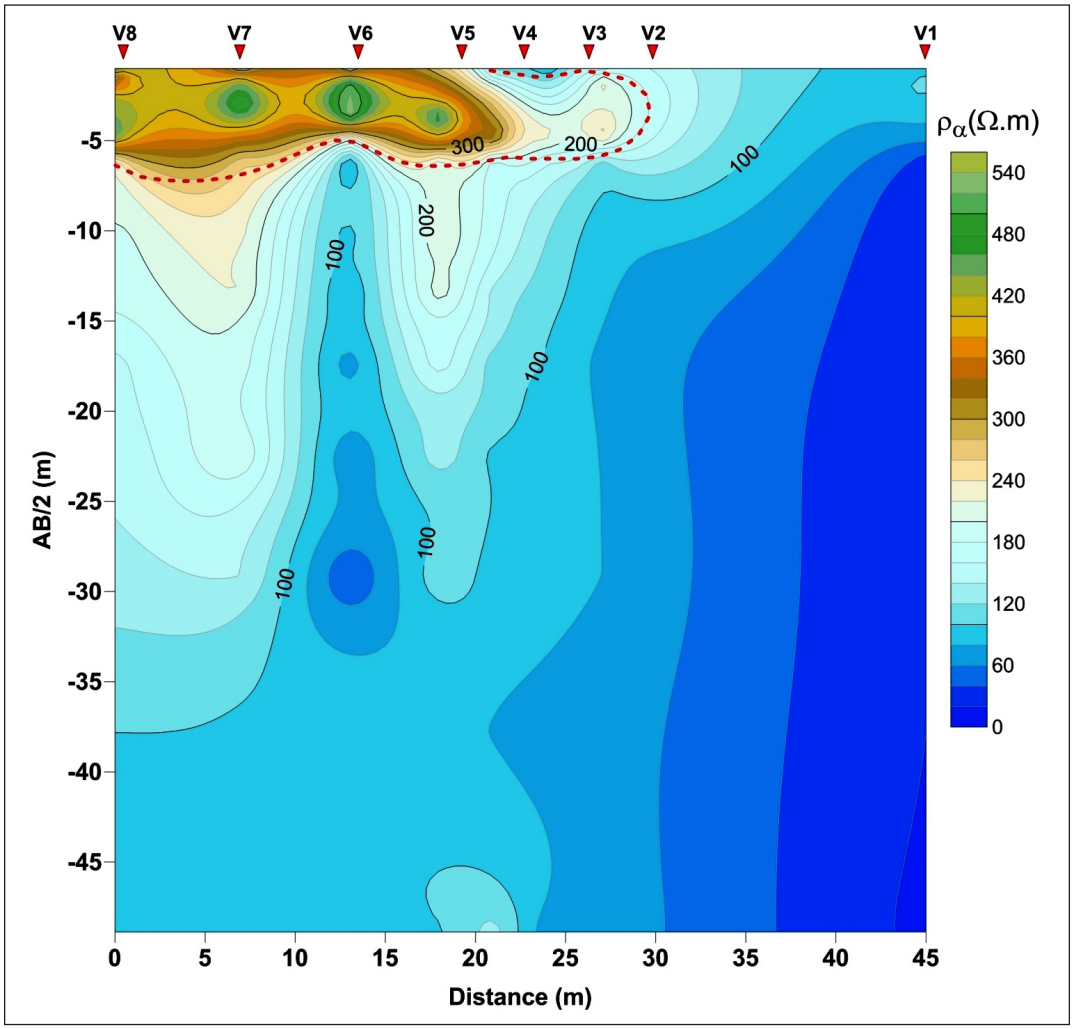

Figure 9. The pseudo section of apparent resistivity as a function of *AB/2* (ρa= f (*AB/2*) along the study Mhembel profile. The Recent and Quaternary structure is well identified near to the surface.

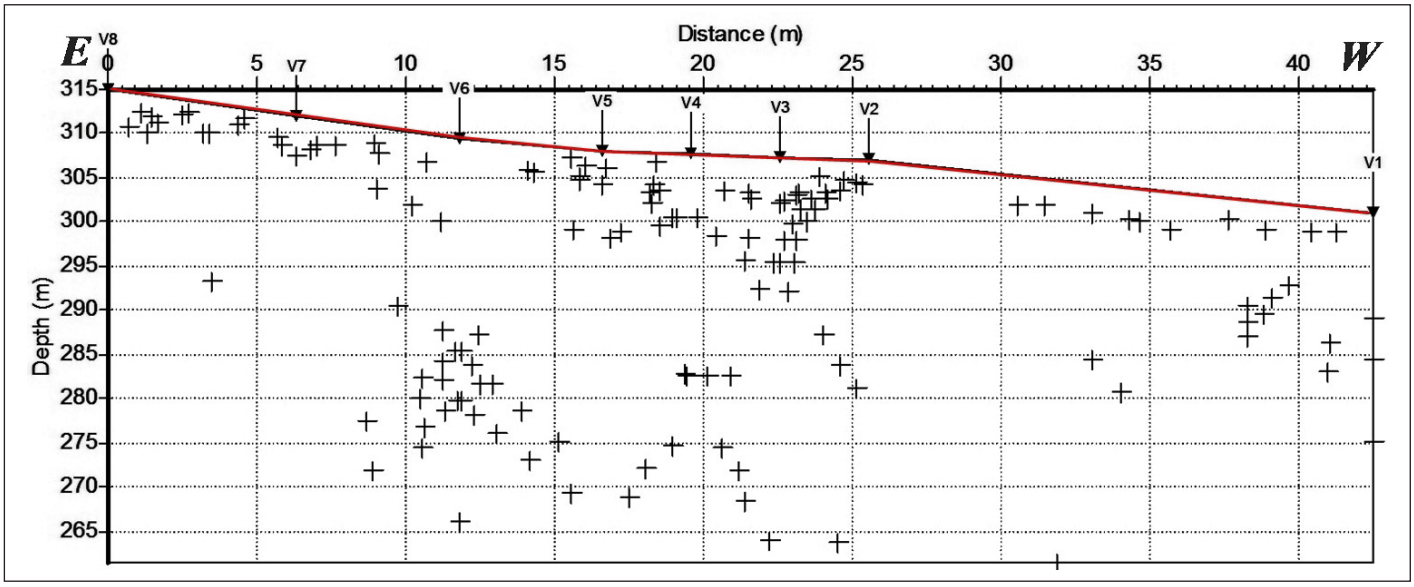

Figure 10. Non homogeneity points (+) obtained along the studied profile. The combination of the one dimensional (*1D*) results obtained by the quantitative interpretation of the eight *VES* soundings with the distribution of the non homegenity points allows to get the litho-structural two dimensional model (*2D*) along the studied *E-W* profile as shown in Figure 11.

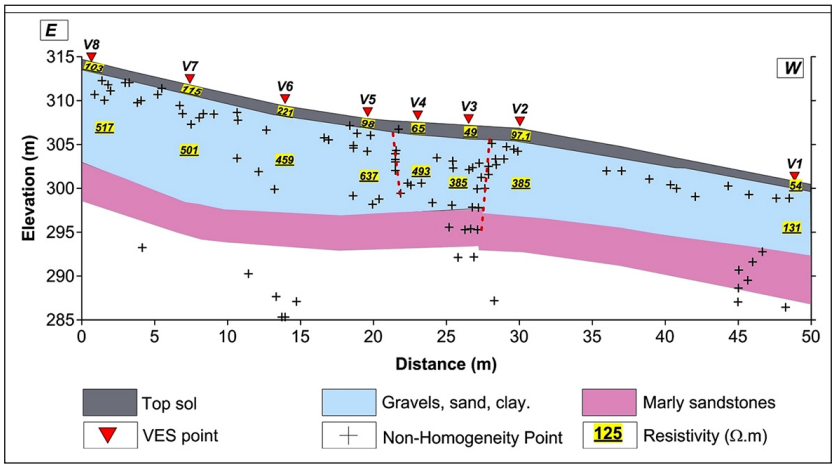

Figure 11. Two dimensional (*2D*) litho-structural model obtained along the *E-W* studied profile at Mhambel site.

the second one. A faulted zone is detected and located between *V2* and *V5*, where the non homogeneity points and their distribution with depth are located within this zone.

The projection of the same results shown in Figure 11 on a same scale field photo is done as presented on Figure 12 (a,b, and c), to test and calibrate the proposed geoelectrical configuration and to decide at which degree this configuration is apt for detecting shallow subsurface tectonic. This projection shows the details of the fault exposure under the slope and shows also a sharp resistivity layering correspondent to lithological differentiations between the Recent alluvial deposits and Pliocene light red marl and clayey marl extends from *V1* to *V2* Soundings. The non homogeneity points obtained by the enhanced Pichgin and Habibuleav profile are well located in the contacted and faulted zone, and reflect clearly the faulting and the resistivity changes related to the lithology of Tortonian and Quaternary.

The AB/2 spacing values ranging from 1 to 3.66 m could detect the shallow faulting, whose depth and width are less than 3 and 5 m respectively.

The AB/2 spacing values that range from 4.74 to 22.49 cannot detect those shallow faulting, nevertheless trace of deeper faulting which has no surface expression since it is covered by the Quaternary sediments. The observation indicates that the surface faulting is younger than the Quaternary sediments, while the deep faulting is older than it.

Conclusions

The application of the adapted *VES* configuration with the new geoelectrical approach proved that the electrical method is applicable and productive in detecting shallow depth tectonic deformation in Recent and Quaternary sediments, hence in active tectonic researches.

An electric signature of a normal faulting in a media of different lithologies is attained. The advantage of integrating this electric Schlumberger configuration within a geoelectrical interpretative approach is evident through its

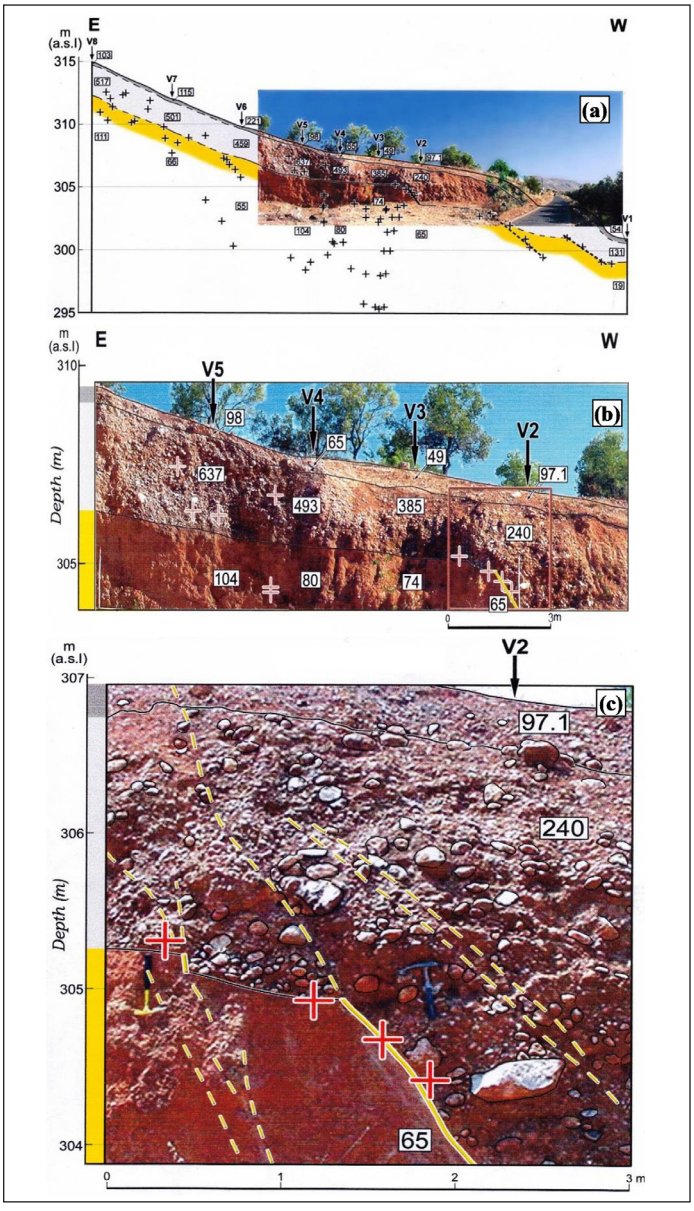

Figure 12. a): Real dimensional (*2D*) litho-structural model obtained along the *E-W* studied profile at Mhambel site; b): Detailed *2D* model between *V5* and *V2*; c): Detailed *2D* model under *V2*.

simplicity and rapidity. The integrated use of the measured *VES* data with the advanced and enhanced Pichigin and Habibulaieve interpretation approach makes the application of such an adapted array possible in a reliefed terrain, where a reliable image of the shallow subsurface structures can be reflected. The electrical signature obtained from the calibration of this adapted Schlumberger configuration at the selected site of Mhembel will guide electrical surveys performed in the frame of future active tectonic research to detect the subsurface buried normal faulting. The established subsurface geoelectrical imaging obtained by this geoelectrical integrated approach along different profiles in a given study area will in addition allow to determine later the privileged locations for trenching, used for studying the new active tectonic features.

Acknowledgment

The authors would like to thank Prof. I. Othman the Director General of the Atomic Energy Commission of Syria (AECS) for his approval to publish this paper. The two anonymous reviewers are thanked for their skin professional remarks, critics, and propositions that considerably improved the final version of this paper. Thanks are due to Prof. Servando De la Cruz-Reyna, the Editor in Chief of the Geofisica Internacional for his assistance during the different process of this paper.

Declaration of competing interest

The authors declare that they have no known competing financial interests or personal relationships that could have appeared to influence the work reported in this paper.

References

Al-Fares, W., 2019. Using Vertical Electrical Soundings for Characterizing Hydrogeological and Tectonic Settings in Deir El-Adas Area, Yarmouk Basin, Syria. *Acta Geophysica, 64*, 3, 610-632.

Al-Fares, W. and Asfahani, J. 2018. Evaluation of the leakage origin in Abu Baara earthen dam using electrical resistivity tomography, northwestern Syria. *GEOFÍSICA INTERNACIONAL 57*,4, 223-237.

Ambraseys, N. N. and Jackson, J. A., 1998. Faulting associated with with historical and recent earthquakes in the Eastern Mediterranean region, *Geophysical Journal International, 133*, 390-406.

Asfahani, J., Mohamad, R., 2002. Geoelectrical Investigation for sulfur prospecting in Techreen structure in northern Syria, Exploration and Mining Geology,11, 49-59.

Asfahani, J., 2007a. Geoelectrical Investigation for Characterizing the Hydrogeological Conditions in Semi Arid Region in Khanasser Valley, Syria: Journal of Arid Environnments, 68, 31-52.

Asfahani, J., 2007b. Electrical Earth Resistivity surveying for delineating the characteristics of ground water in semiarid region in Khanaser Valley, Northern Syria. *Hydrological Processes, 21*, 1085-1097.

Asfahani, J., 2010. Electrical Resistivity Investigations for Guiding and Controlling Fresh Water Wells Drilling in Semi Arid Region in Khanasser Valley, Northern Syria. *Acta Geophysica*, DOI: 10.2478/S11600-0010-0031-8.

Asfahani, J., and Radwan, Y., 2007. Tectonic Evolution and Hydrogeological Characteristics of Khanaser Valley, Northern Syria, Derived from the Interpretation of Vertical Electrical Soundings. *Pure Appl. Geophys, 164*, 2291-2311.`

Asfahani, J., Radwan, Y., and Layyous, I., 2010. Integrated Geophysical and Morphotectonic Survey of Impact of Ghab Extensional Tectonics on the Qastoon Dam, Northwestern Syria. *Pure Appl. Geophys, 167*, 323-338.

Asfahani, J., 2018. Geoelectrical Combined Sounding-Profiling Configuration for Characterizing the Sedimentary Phosphatic Environment in Al-Sharquieh Deposits Mine in Syria. *Geofísica Internacional, 57*, 3,189-203.

Asfahani. J, Al- Fares, W., 2021. Geological and structural characterizations of a basaltic environment by vertical electrical soundings and multifractal modeling techniques in Deir El-Adas Area,Yarmouk Basin, Syria. *Acta Geodaetica et Geophysica, 56*, 211–228.

Asfahani, J., 2010a. Geophysical Case Study of Shallow and Deep Structures Based on Traditional and Modified Interpretation Methods: Application to Tectonic Studies and Mineral Exploration. *Exploration and Mining Geology,19*, 3–4, 135–152. Canadian Institute of Mining, Metallurgy and Petroleum.

Asfahani, J., 2011. The Role of Geoelectrical *DC* Methods in Determining the Subsurface Tectonics Features. Case Studies from Syria. From the Edited Volume Tectonics. Edited by Damien Closson, DOI: 10.5772/13580.

Beydoun, Z. R., 1999. Evolution and development of the Levant (Dead Sea Rift) Transform System: a historical-chronological review of a structural controversy, in C. MacNiocaill, P.D. Ryan (Eds.), Continental Tectonics, Vol. 164, Geological Society of London, London, 239-255

Brew, G., Barazangi, M., Al-Maleh, K., and Sawaf, T., 2001a. Tectonic and Geologic Evolution of Syria. *GeoArabia, 6*, 573-616.

Brew, G., Lupa, J., Barazangi, M., Sawaf, T., Al-Imam, A., and Zaza, T., 2001b. Structure and Tectonic Development of Al-Ghab Basin and the Dead Sea Fault System, Syria. *Journal of the Geological Society, 158*, 665-674.

Butler, R.W.H., Spencer, S. and Griffiths, H.M., 1997. Transcurrent fault activity on the Dead Sea transform in Lebanon and its implications for plate tectonics and seismic hazard. *Journal of the Geological Society, London, 154*, 757-760.

Cai, J., McMechan, A., and Fisher, M.A., 1996. Application of ground penetrating radar for investigation of near surface fault properties in the San Francisco Bay rgion. *Bull. Seis Soc.Am, 86*, 1459-1470.

Caputo, R., Piscitelli, S., Oliveto, A., Rizzo, E., and Lapenna, V., 2003. *The use of electrical resistivity tomographies in active tectonic: Examples from the Tyrnavos basin, Greece, 36*, 1.-2, 19-35.

Caputo, R., Salviulo, L., Piscitelli, S., and Loperte, A., 2007. Late Quaternary activity along the Scorciabuoi fault (Southern Italy) as inferred

from electrical resistivity tomographies. *Annals of Geophysics, 50*, 2, 213-224.

Chaimov, T., Barazangi, M., Al-Saad, D., Sawaf, T., and A. Gebran, 1990. Crustal Shortening in the Palmyride fold belt, Syria, and implications of movement along the Dead Sea fault system. *Tectonics, 9*,1369-1386.

Chakravarthi, V., Shankar GBK., Muralidharan, D., Harinarayana, T., Sundararajan, N. 2007. An integrated geophysical approach for imaging sub basalt sedimentary basins: case study of Jam river basin, India. *Geophysics 72*, 6,141–147.

Chwatel, W., Decker, K., and Roch, K., 2005. Mapping of active capable faults by high-resolution geophysical methods: Examples from the central Vienna basin. *Austrian Journal of Earth Sciences, 97*, 52-59.

Darkal, B.N., M. Krauss and R. Ruske., 1990. The Levant fault zone: an outline of its structure evolution and regional relationship, Z. *Geol Wiss., 18*, 549-562.

Demanet, D., Renardy, F., Vanneste, K., Jongmans, D., Camelbeeck, T., and Meghraoui, M., 2001. The use of geophysical prospecting for imaging active faults in the Roer Graben, Belgium. *Geophysics, 66*, 1, 78-89.

Devyatkin, E.V., Dodonov, A.E., Sharkov, E.V., Zykin, V.S., Simakova, A.N., Khatib, K. and Nseir, H., 1997. The El-Ghab Rift Depression in Syria: Its Structure, Stratigraphy, and History of Development. *Stratigraphy and Geological Correlation, 5*, 4, 362–374.

Dobrin, M., 1976. Introduction to Geophysical Prospecting. Mc Graw-Hill, New York.

Ebong, DE., Akpan, AE., Onwuegbuche, AA. 2014. Estimation of geohydraulic parameters from fractured shales and sandstone aquifers of Abi (Nigeria) using electrical resistivity and hydrogeologic measurements. *J. Afr. Earth. Sci., 96*, 99–109.

Fazzito, S.Y., Rapalini, A.E., Cortes, J.M., and Terrizzano, C.M., 2009. Characterization of Quaternary faults by electric resistivity tomography in the Andean Precordillera of Western Argentina: Journal of South American. *Earth Sciences, 2*8, 217–228.

Freund, R., Garfunkel, Z., Zak, I., Goldberg, M., Weissbrod, T., Derin, B., Bender, F., Wellings, F., Girdler, R. 1970. The Shear along the Dead Sea Rift [and Discussion]. *Philos Trans R Soc Lond Ser A Math Phys Sci 267*(1181):107.

Gomez, F., Meghraoui, M., Darkal, A. N., Hijazi, F., Mouty, M., Suleiman, Y., Sbeinati, R., Darawcheh, R., Al-Ghazzi, R., Barazangi, M., 2003. Holocene faulting and earthquake recurrence along the Serghaya branch of the Dead Sea fault system in Syria and Lebanon. *Geophys. J. Int. 153*, 3, 658-674.

Gomez, F., Khawlie, M., Tabet, C., Darkal, A. N., Khair, K. & Barazangi, M., 2006.

Neotectonics of the northern Dead Sea fault system in Lebanon and Syria based on SAR imagery and high resolution DEM data. *Earth Planet. Sci. Lett., 241*, 913-931.

Hricko, J., 1988. Geophysical Exploration in Selected Areas of Syrian Arab Republic, Stage Report on Survey in Jisr al Shoghour Area. Unpublished internal report. Strojexport Praha-Geofysika Brno, Czechoslovakia, Damascus/Brno.

Massoud, U., El Qady, G., Metwaly, M., and Santos, F., 2009. Delineation of shallow subsurface structure by azimuthal resistivity sounding and joint inversion of *VES*-TEM data: case study near Lake Qaroun, El Fayoum, Egypt. *Pure Appl. Geophys,166*, 701-719.

McClusky, S. and Balassanian, S., 2000. *GPS* constraints on plate kinematics and dynamics in the Eastern Mediterranean and Caucasus. *Journal of Geophysical Research, 105*, 5695-5719.

Meghraoui, M., Gomez, F., Sbeinati, R., Van der Woerd, J., Mouty, M., Darkal, A. N., Radwan, Y., Layous, I., Al Najjar, H., Darawcheh, R., Hijazi, F., Al Ghazzi, R., Barazangi, M., 2003. Evidence for 830 years of seismic quiescence from palaeoseismology, archaeoseismology and historical seismicity along the Dead Sea Fault in Syria. *Earth Planetary Sci. Lett. 210*, 35-52

Orellana, E., and Mooney, H.M., 1966. Master Tables and Curves for Vertical Electrical Sounding Over Layered Structures:Interciencia, Madrid.

Palmer, J.R., Shoemaker, M., Hoffman, D., Anderson, N. L., Vaughn, J. D., and Harrison, R.W., 1997. Seismic evidence of quaternary faulting in the Benton hills area, southeast Missouri. *Seis. Res. Lett, 68*, 650-661.

Parrales, R., Dahlin,T., and Rubi, C., 2003. Site investigation with combined methods in a faulted area in Managua, Nicaragua- A pre-study: Procs. 9th Meeting of Environmental and Engineering Geophysics, Prague, Czech Republic, P-076.

Pichgin, N.I., and Habibullaev, I.K.H., 1985. methodological recomendations in studying geo-tectonic conditions of vertical electrical soundings data with application of computer for solving hydrogeological and geo-engineering problems, Tashkend, (in Russian).

Piscitelli, S., Caputo, R., Lapenna, V., Oliveto, A., and Rizzo, E., 2009. Electrical imaging survey across activity faults: Examples from the Tyrnavos basin, Greec: GNGTS- Atti del 21o Convegno Nazional/01.01

Ponikarov, V.P., (ed.) 1966. The Geological Map of Syria, scale 1:200000, sheets I-37-XIX and I-36-XXIV, Ministry of Industry, Damascus.

Quennell, A., 1959. Tectonics of the Dead Sea rift. Int. Geol. Congr., 20th Sess., Mexico, 385–405.

Quennell, A. M., The Western Arabia rift system In: Dixon, J. E. and Robertson, A. H. F. (eds.), 1984. The Geological Evolution of the Eastern Mediterranean, Geological Society, London, Special publications,17, 775-788.

Radwan, Y. Najjar, H. and I. Layyous, 1994a. Indications of neotectonics along the Syrian Lebanese fault (AL-Ghab Depression). In Proceedings of the Regional Workshop on Archaeoseismicity in the Mediterranean Region, AECS, Damascus, 122-133.

Radwan, Y. Najjar, H. and I. Layyous, 1994b. Investigations of Active Tectonic Along the Major Faults in Syria Using Geomorphic Techniques, The proceedings of the Second International Conference on Geology of the Arab World, vol. II, 59-71.

Sabrina Y.F., Augusto E.R., Jose M, Cortes., and Carla M., 2009. Characterization of Quaternary faults by electric resistivity tomography in the Andean Precordillera of Western Argentina. Journal of South American Earth Sciences, 28, 3, 217-228.

Shields, G., Allander, K., Brigham, R., Crosbie, R., Trimble, L., Sleeman, M., Tucker, R., Zhan, H., and Louie, J.N., 1998. Shallow geophysical survey across the Pahrump Valley fault zone. California- Nevada border. *Bull. Seis Soc. Am, 88*, 270-275.

Sirwa, G., Asfahani,. J., 2019. Subsurface tectonic characterizations by the use of geo-electrical resistivity technique and their implications on environmental soil and groundwater at Erbil dumpsite, west of Erbil city–Iraqi Kurdistan region. *Contributions to Geophysics and Geodesy, 49*, 3, 325–354.

Van Ardsal, R., Purser, J., Stephenson, W., and Odum, J., 1998. Faulting along the southern margin of Reeflot Lake, Tennesse. *Bull. Seis Soc. Am, 88*, 131-139.

Velpen, B.A., 2004.Win RESIST Version 1.0. M.Sc Research Project. ITC, Deft, Netherlands.

Williams, R., Luzietti, E, A., and Carver, D, L., 1995. High- resolution imaging of Quaternary faulting on the Crittenden County fault zone, New Madrid seismic zone, northeastern Arkansa. *Seis. Res. Lett, 66*, 42-57.

Zohdy, A.A.R., 1989. A New Method for the Automatic Interpretation of Schlumberger and Wenner Sounding Curves. *Geophysics, 54*, 245-253.

Zohdy, A.A.R. and Bisdorf, R.J., 1989. Schlumberger Sounding Data Processing and Interpretation Program: U. S. Geological Survey, Denver.